# Tuning Structural, Electronic, Magnetic and Optical Properties of 2D-$WX_2$ under Biaxial Strain and Substitutional Doping in First Principles Method

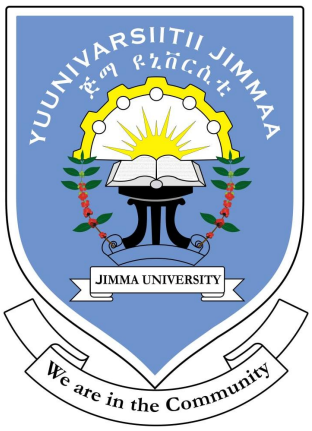


Mulugeta Shiferaw Woldesenbet

A Dissertation Submitted to Department of Physics

in Fulfillment of the Requirement of Degree of Doctor of

Philosophy in Physics (Condensed matter Physics)

at

Jimma University

Supervisors:

Professor Menberu Mengesha (PhD)

Nebiyu Gemechu (Associate professor, PhD)

**Jimma, Ethiopia**

June, 2024

JIMMA UNIVERSITY
DEPARTMENT OF PHYSICS

This is to certify that the thesis prepared by **Mulugeta Shiferaw Woldesenbet** Graduate Studies entitled "**Tuning the Structural, Electronic, Magnetic and Optical Properties of 2D-$WX_2$ under Biaxial Strain and Substitutional Doping in First Principles Method**" in fulfillment of the requirements for the degree of DOCTOR OF PHILOSOPHY IN PHYSICS (Condensed Matter Physics) complies with the regulations of the University and meets the accepted standards with respect to originality and quality.

| | | |
|---|---|---|
| Professor Menberu Mengesha (PhD) | 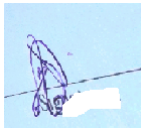 | June 25, 2024 |
| Advisor | Signature | Date |
| Nebiyu Gemechu (Associate Professor, PhD) | 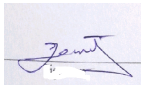 | June 25, 2024 |
| Advisor (co) | Signature | Date |
| Sintayehu Mekonnen (Associate Professor, PhD) |  | June 25, 2024 |
| External Examiner | Signature | Date |
| Mulualem Abebe (Associate Professor, PhD) |  | June 25, 2024 |
| Internal Exanminer | Signature | Date |
| Tolu Biressa (PhD, Department head) |  | June 25, 2024 |
| Chair person | Signature | Date |

# JIMMA UNIVERSITY

Date: June 25, 2024

Author: **Mulugeta Shiferaw Woldesenbet**

Title: Tuning the Structural, Electronic, Magnetic and Optical Properties of 2D-$WX_2$ under Biaxial Strain and Substitutional Doping in First Principles Method

**Department**: Physics

**Degree**: PhD

**Convocation**: June 2024

Permission is herewith granted to Jimma University to circulate and to have copied for non-commercial purposes, at its discretion, the above title upon the request of individuals or institutions.

Signature of Author

Date: June 25, 2024

# DEDICATION

This thesis is dedicated to my families.

# Acknowledgments

I want to begin by thanking Almighty God for enabling me to finish this endeavor in spite of many challenges. The completion of this study would not have been possible without the invaluable cooperation of my advisor, Professor Menberu Mengesha, who has been constant source of support ever since he connected me with resources and organizations for help to get the training and materials needed for my research. I would like to express my gratitude to Dr. Nebiyu Gemechu, associate professor, for all of his support and wise advice throughout this study. Furthermore, the College of Natural Sciences and Department of Physics have my deepest gratitude for their diligent attention to detail and unceasing support throughout the program, helping me and others to the best of their abilities.

Afterwards, I want to express my gratitude to my spouse Selam Wolde and my kids, Efrata and Eyoab, for their love and patience with me while I studied. In addition, I want to express my gratitude to parents, my mother and siblings, for their love, support, and encouragement. I would also like to express my gratitude to friends, specially to Fitsum Emiru, colleagues, and relatives for their support, encouragement, well wishes and guidance during my study time.

Last but not the least, I would like to acknowledge the institutions and organizations that had contributed great role to accomplish my research works. Bonga University for all contributions in terms of offering financial and material support and Jimma University for providing the research fund and other facilities required for the course and research works. Finally, I want to express my gratitude to the International Center for Theoretical Physics (ICTP) and the Computational Science and Engineering Society of Ethiopia (CSESE) for providing training in "High Performance Computing (HPC)" and the use of remote servers for solving high level research problems.

# List of abbreviations

† **AFM** - Antiferromagnetic

† **CDW** - Charge density wave

† **CVD** - Chemical vapor deposition

† **DFPT** - Density functional perturbation theory

† **DFT** - Density functional theory

† **DMS** - Dilute magnetic semiconductor

† **DOS** - Density of states

† **EELS** - electron energy loss function spectrum

† **FET** - Field effect transistor

† **FM** - Ferromagnetic

† **GGA** - Generalized Gradient Approximation

† **GNU** - Gnu's Not Unix

† **GPL** - General Public License

† **HK** - Hohenberg-Kohn

† **KS** - Kohn–Sham

† **LDA** - Local Density Approximation

† **LR-cDFT** - linear response constrained density functional theory

† **ML** - Mono-layer

† **NCPP** - Norm-conserving pseudopotential

† **PAW** - Projector-augmented wave

† **PBE** - Perdew, Burke and Ernzerhof

† **PL** - Photo-luminescence

† **PP** - Pseudo-potential

† **PW** - Plane wave

† **QE** - Quantum-Espresso

† **SSSP** - Standard solid state pseudopotential

† **SOC** - Spin-orbit coupling

† **TMD** - Transition metal dichalcogenide

† **TD-DFT** - Time-dependent density functional theory

† **TFT** - Thin film transistor

† **USPP** - Ultra-soft Pseudopotential

† **vdW** - Van der Waals

† **1L** - One layer

† **2D** - Two dimensional

# Abstract

Two dimensional (2D) $WX_2$ for X= S, Se and Te in various supercell sizes are considered in monolayer and heterobilayer. The structural, electronic, magnetic, and optical properties of 2D- $WX_2$ are investigated using density functional theory (DFT) with respect to a plane wave ultra-soft Pseudopotentials (PW-USPPs) and normconserving pseudopotentials (NCPPs) in a generalized gradient approximation (GGA) and the Hubbard correction (GGA + U) with the implementation of quantum espresso package. The optimized lattice parameters have been investigated interactively in each type of material. The band gaps for monolayer $WTe_2$ are investigated for unstrained, 2% biaxial compressive and tensile strain to the slab of the monolayer using GGA and GGA+U approximations. In GGA+U approximation, the energy band gap becomes slightly wider than with that of the GGA approximation. Monolayer $WTe_2$ under biaxial compression exhibits an expanded energy band resulting in blue shift and in biaxial tension red shift by narrowing of the energy band gap in comparison to the equilibrium.

Pristine $WSe_2$ monolayer is identified as a nonmagnetic direct band gap semiconductor with a band gap of 1.55 eV. Upon substituting Mn for W in the $WSe_2$ monolayer, the resulting structure exhibits enhanced stability, indicated by a negative formation energy. The Mn doped monolayer of $WSe_2$ has slightly shorter bond length with 2.4294$\mathring{A}$ than the pure with 2.5405$\mathring{A}$ for the Mn-Se and W-Se respectively. The doped system becomes FM and total magnetic moment within the nearest neighboring interactions of the impurity atoms increases notably and it is attributed to the electron-correlation effect in the high spin state under the GGA+U approximation. However, this correlation effect proves insignificant on the total magnetic moment for the second nearest neighboring interactions, yielding consistent outcomes in both GGA and GGA+U approximations. The transition of FM to AFM state occurs above room temperature for low impurity concentration, 443 k and 450 k for 8% and 12.5% substitution with Mn respectively. This indicates long-range FM ordering and crucial for high-temperature 2D-diluted magnetic semiconductors. However, at high concentrations of impurity atoms, the temperature drops below room temperature (220 K in 22.2%) in the doped monolayer $WSe_2$, showing weak magnetic interaction. Lastly, the optical property of a doped system is studied by applying polarization in perpendicular and parallel directions to the plane of the monolayer.

For two-dimensional $WS_2$/$WSe_2$ hetero structure lattice constant and the vertical interlayer distance between slabs are $a = 3.28\mathring{A}$ and $c = 13.14\mathring{A}$ respectively. The band gaps for $WS_2$/$WSe_2$ hetero structure are investigated for unstrained, (0-4)% biaxial compression and tension using GGA approximations. Direct band gap of 0.51eV is obtained for unstrained heterostructure. The band gap value of the heterobilayer is affected by the application of strain. When the heterobilayer is imposed to biaxial compression the band gap value increases. However, the tensile stress results in reducing the band gap value of the heterobilayer and the system attains its metallic or semimetalic state at 4% biaxial tensile strain. Tunability of the band gap is very

crucial in developing photovoltaic and optoelectronic devices. The strained heterostructure shows different optical property when it is under biaxial tension and compression due to the change in the values of the band gap. The heterobilayer has also high absorption coefficient in the visible light spectrum which makes it a promising material for photovoltaic applications.

# Contents

# List of Figures

# List of Tables

# Chapter 1

# Introduction

## 1.1 Background of the Study

After successful isolation of graphene, single layer graphite 2004 , two dimensional (2D) materials become an interesting area of investigation [1]. Graphene is an extraordinary 2D material with high Young's modulus, high electron mobility and good thermal conductivity [2, 3]. Because of these exciting properties, graphene is expected to be used in nano-devices as transparent conducting electrodes, energy storage, field effect transistors, sensors, photo-detectors, solar cells and others [3, 4]. Despite these interesting profile, graphene is zero bandgap material and this limits its applications for logical operations and searching for 2D-semiconductors with finite band-gap becomes important to overcome the limitations. 2D materials found in nature with different characteristics including insulators hexagonal boron-nitride (hBN), direct band gap semiconductors ($MoS_2$, $WS_2$), semi-metals ($WTe_2$) and metals ( $NbSe_2$) [5, 6, 7].

Recently, two dimensional materials including transition metal dichalcogenides (TMDs) are highly initiating the scientific community because of their unique properties [4, 6]. According to the statistical data recorded on publications of 2D and 2D composite materials, shown in (Figure-1.1), are growing fast from year to year [8]. TMDs are characterized by $MX_2$, where M stands for a transition metal elements consisting (Mo, W, Nb, Cr etc.) and X stands for chalcogen elements (S, Se, and Te). $MX_2$ are strongly bonded in a 2D layer, while neighboring layers are stacked by weak van der Waals (vdW) forces [2, 9]. Even though bulk TMDs were well

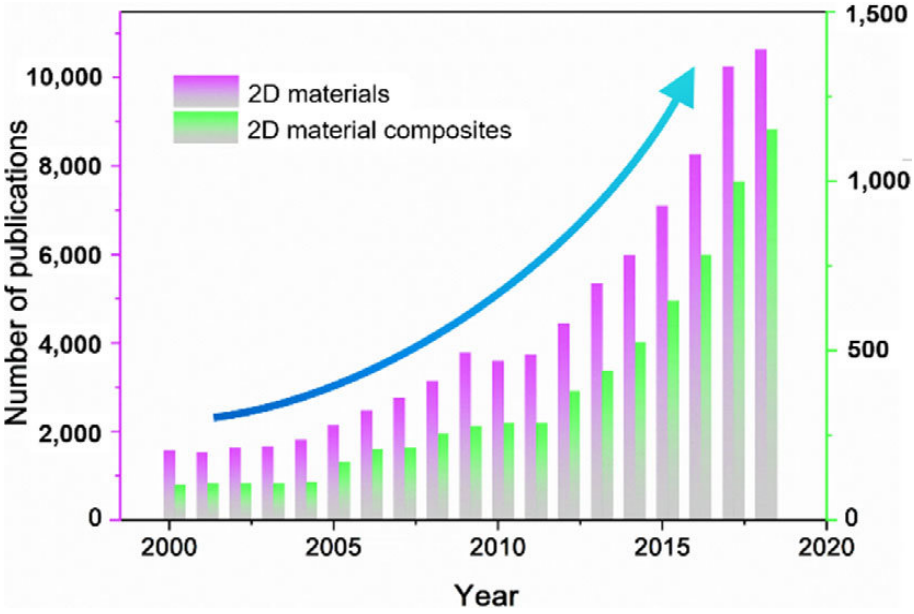


Figure 1.1: Evolution of studies on 2D and 2D-composite materials

known for a long, their application was limited [7, 10, 11]. After the discovery of graphene, 2D TMDs become exciting for further investigations. For example, 2D $MoS_2$, $WS_2$, $MoSe_2$, and $WSe_2$ semiconductors with direct bandgap are taken to be potential complement to graphene [12, 13]. 2D $CrX_2$, $MoX_2$, and $WX_2$, show direct bandgaps according to Rasmussen et al. [14] and Graedel et al. stated the environmental impacts [15] of these materials. These foundations enforce to identify and develop high-performing, cost-effective, energy-saving and environmentally friendly materials. Reduced dimension and novel compositions of these structures lead for further improvement and develop additional strategies for best performance including doping and heterostructure formations [16, 17].

Bulk TMD materials can be thinned to a few or single layer structures because of the weak interactions between the layers and these layers are different from their bulk counterparts [18]. Among TMDs, 2D $MoS_2$ is well studied with high on/off ratio, high cut-off frequency, and photo-detectors with high sensitivity have been successfully demonstrated. On the other hand, $WS_2$ is another typical 2D semiconducting TMD, with a direct band gap depending on the number of layers [19, 20]. The room-temperature electron mobility in monolayer $WS_2$ is over $1000 cm^2/Vs$, which is the highest among semiconducting TMD materials [21]. Although there are other interesting properties, 2D-tungsten dichalcogenide materials are less explored than

that of 2D-molybdenum dichalcogenides. The investigate electronic structure, lattice vibration and optical properties of $WTe_2$ with the application of strain important since it has low and direct band gap against small strain and this leads the material promising for electronic and photovoltaic applications with external stress. The magnetic property of 2D tungsten dichalcogenides is also another interesting area since pure 2D $WX_2$ are nonmagnetic semiconducting materials. Incorporating magnetic properties by doping with magnetic elements to $WX_2$ made the family of materials more applicable in wide range of applications like spintronics. Heterostructure with $WS_2$/$WSe_2$ is also targeted to be explored. Since the hetrobilayers have narrower band gap than individual monolayers and direct band gaps in contrast to homobilayers investigation of is electronic and optical properties with and without application of strain is also important to explore a wide range of applications in $WX_2$. Therefore, designing efficient model of the material computationally in first principles method using Quantum - Espresso open source software is the target.

## 1.2 Statement of the problem

2D Tungsten dichalcogenides ($WX_2$) are among 2D TMDs which are promising novel materials. Molybdenum dichalcogenide have been extensively explored in advance in comparison to tungsten families. $MoX_2$ materials have low carrier mobility at room temperature than $WX_2$ and this leads to examine $WX_2$ more better outcomes theoretically as well as experimentally. In addition, $WX_2$ have direct band gaps in monolayers comparatively less than that of 2D $MoX_2$ families. In general, $WX_2$ family of 2D materials require profound investigations for the mechanical, electronic, optical and magnetic proprieties. Employing first principle calculations on the family of $WX_2$, the following target points are used to be addressed throughout the study:

- The kind of crystal structural that 2D $WS_2$, $WSe_2$ and $WTe_2$ mono-layers and heterobilayers have with and without biaxial strain and in substitutional doping to one or more atoms of the pristine $WX_2$.

- The response in band structure and the density of states of 2D $WSe_2$ to an external stress (compressive/tensile) and doping by manganese in substitution to one or more tungsten

atoms in a monolayer.

- The effect of on site coulomb repulsion and the importance of utilizing the Hubbard correction on computation.

- The nature of optical parameters such as complex dielectric function, index of refraction and absorption coefficients in 2D $WS_2$, $WSe_2$ and $WTe_2$ with substitutional doping and biaxial strain

- Tuning of magnetic property under substitutional doping to 2D $WX_2$ with magnetic element in response to impurity concentration.

- Determination of optimum concentration of dopant to the pure $WX_2$ that keep stable ferromagnetism and the resulting curie temperature.

## 1.3 Objectives of the Study

### 1.3.1 General Objective

The general objective of this study is to investigate the structural, electronic, magnetic and optical properties of 2D $WX_2$, for X=S, Se and Te using density functional theory (GGA and GGA+U approximations).

### 1.3.2 Specific Objectives

The specific objectives of this study are:

1. To calculate the structural parameters of 2D mono and hetero bilayes of $WX_2$ in first principles method.

2. To analyze the electronic structure (band gap and the density of states) of 2D $WX_2$ under the effect of strain using first principles method.

3. To compute the optical parameters such as dielectric function, refractive index and absorption coefficients of 2D $WX_2$ using TD-DFT.

4. To determine the ferromagnetic property and its stability in Mn-doped 2D $WSe_2$ in DFT and DFT+U methods.

5. To analyze the effect of biaxial strain on electronic and optical properties of 2D $WX_2$ with mono and heterobilayers using the first principles method.

## 1.4 Significance of the study

2D materials are the future materials and among these the 2D-TMDs are expected to solve some of drawbacks on the field because of their wide range of band gaps in contrast to graphene. Therefore, the importance of this study is to determine necessary properties of $WS_2$, $WSe_2$, $WTe_2$ theoretically in first principle calculations. Using DFT and DFT+U, the structural, electronic, optical and magnetic properties of 2D $WX_2$ were intensively analyzed with Quantum-Espresso open source package. The findings of this research showed tungsten dichalcogenide have promising electronic, magnetic and optical properties. Thus, this work is significantly important for further experimental investigations and add some important values on the science.

## 1.5 Outline of structure of the Dissertation

The dissertation is organized in different chapters and sections by beginning with background of the basic principles of condensed matter physics behind the two dimensional transition metal dichalcogenides basically of tungsten families and the first principles approach in the study of such materials. The first chapter discusses the background and general introduction about the focus of the study. In addition the general and specific objectives of the study have been listed in this chapter and finally, structure of the Dissertation works is described.

Chapter two deals with reviewing literature related to two dimensional tungsten dichalcogenides. The basic parameters of the family of 2D-TMDs are examined to investigate foundation of structural, electronic, lattice vibration, magnetic and optical properties of the material and its advancement up to date. Chapter three deals with the methodology mainly the density

functional theory (DFT) and gives the detail insight of the basic principles of the density functional theory (DFT), the spin polarized DFT and the Hubbard correction (DFT+U) used in this study. Under the chapter, the software packages, pseudopotential selection and computation strategies used in of the study are described.

Chapter four discuses on the results of the study in different sections for each section dealing with independent results and analysis. This chapter is the main part of this study and contains all the results in different form as tables, graphs and discussions in detail. Finally, chapter five gives conclusions and summaries of the works by condensing the whole picture of the study in short and clear expressions.

# Chapter 2

# Review of Related Literature

## 2.1 Structure of Two Dimensional $WX_2$

Two dimensional TMDs have mostly two polymorphs, trigonal prismatic (2H) and octahedral (1T) phase structures [22, 23]. In the 2H phase, a single layer of atoms are vertically aligned. Thus, the stacking state of this phase shows X-W-X, where X is for chalcogen layers and W is for transition-metal layers. In 1T phase, one of the single layers is shifted relative to the other. For $WX_2$ structure at room temperature, the 2H phase is stable whereas the 1T phase is metastable.

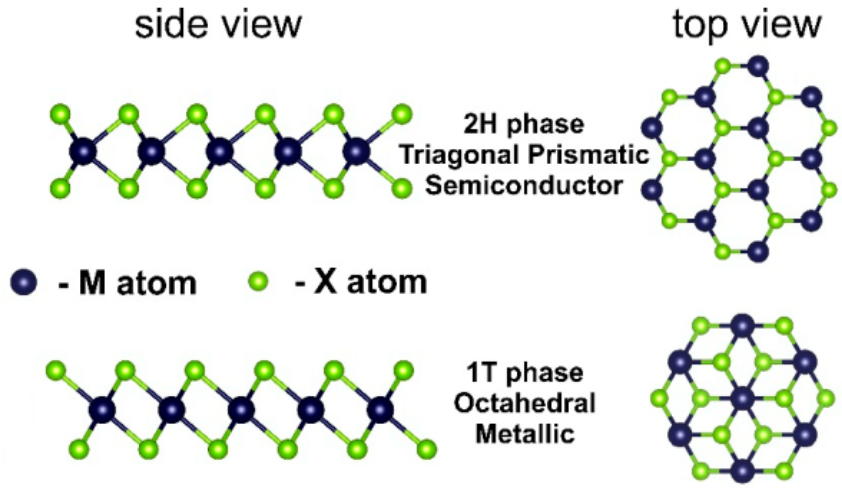


Figure 2.1: Different structural models of the 2H and 1T polymorphs in 2D-TMDs

The 2H phase could be converted to 1T phase under certain conditions, such as Li-ion intercalation, electron beam, laser beam irradiation, as well as plasma bombardment [24]. The chemically exfoliated 1T $MoS_2$ phase is known to be $10^7$ times more conductive than the semiconducting 2H phase [25]. On the other hand, the 1T phase could also be converted to 2H phase [26, 27]. The most prominent feature of the group VIB TMDs is the layer-dependent band structure tunability that they own an indirect bandgap in bulk, which becomes direct one when being thinned down to monolayer limit [6].

## 2.2 Mechanical properties of Two dimensional-$WX_2$

There are numerous benefits to 2D TMDs containing chalcogens and heavier transition metals. It has been expected that among 2D TMDs, monolayer (1L) tungsten disulfide ($WS_2$) will perform best in field-effect transistors (FETs) and have the maximum mobility because to its reduced effective mass[28]. In tungsten dichalcogenide, for example the Young's modulus of CVD-grown 1L $WS_2$ was measured by indentation and found to be $(272 \pm 18 GPa)$ [29] and different layers of $_2$ prepared by mechanical exfoliation were also measured with different values for each layer [30]. The experimental elasticity and strength values of atomically thin $WS_2$, $_2$, and $WTe_2$ are still not verified despite theoretical predictions [31]. Ab initio vdW-corrected density functional theory (DFT) calculations is used to reveal the distinct sliding tendencies in $WS_2$, $WSe_2$, and $WTe_2$ under strain[32].

Two-dimensional (2D) materials are particularly suited for strain engineering because they combine a high in-plane mechanical strength and an extremely small bending rigidity with substantial strain tunability of electronic band structure [33, 34]. The unique mechanical strength, flexibility, and tunability of 2D materials have therefore enabled their applications for wearable and flexible technologies[35, 36] as well as fundamental studies of material properties under carefully engineered strain conditions. The semiconducting layered transition-metal dichalcogenides (TMDs) have emerged as particularly interesting candidates for strain engineering, [37, 27] since they have exhibited exciton funneling strain-mediated phase transitions.

Strain engineering has been explored in TMDC monolayers, multilayers, and heterostructures. Multilayer TMDCs are particularly interesting because they are known to exhibit interlayer exciton transitions, that is, optical transitions where the electron-hole pairs are located in different constituent layers bounded by strong Coulomb interaction[38]. These interlayer excitons have been observed to be strain tunable in homobilayers of molybdenum disulfide ($MoS_2$)[39] and heterobilayers of molybdenum diselenide and tungsten diselenide ($MoSe_2/WSe_2$)[40] with deformation potentials.

## 2.3 Lattice vibration of Two Dimensional-$WX_2$

2D TMDs are expected to be used in field effect transistors with high on/off ratio. In addition, biaxial strain can shift the band gap which makes them efficient in solar spectrum. In these and other areas of applications, the efficiency of 2D TMD materials is highly affected by thermal properties of the materials. According to different theoretical and experimental findings, thermal conductivity of 2D TMDs is much lower than graphene. Because of their ultra-small thickness, handling thermal properties of these materials become much complicated. It is important to take the lattice vibrational mode (phonon) into account to understand the thermal properties of these materials. For 2D $MoS_2$ the unit cell contains three atoms (S-Mo-S) which creates three acoustic and six optical phonon modes with the three acoustic phonon modes are longitudinal acoustic (LA) mode, transverse acoustic (TA) and flexural acoustic (ZA) mode [41]. The frequency of the LA and TA modes have linear dispersion with vector q for small near the center of the Brillouin zone. The group velocities of monolayer $MoS_2$ are $V_{LA}$=1108.8m/s and $V_{TA}$= 693.5m/s are much lower than those in graphene . However, ZA modes have approximately quadratic dispersion. According to the first principle calculation at low temperature, most TMDs like $WS_2$, $WSe_2$, $MoS_2$, and $MoSe_2$ have positive thermal expansion but it is negative in the case of graphene [42]. One of the corrective schemes widely used to alleviate the challenges of residual self-interaction is the GGA + U approach [43, 44]. Moreover, the density functional perturbation theory with Hubbard correction (DFPT + U functional) [45] gives more precise results for phonon dispersion as compared to the density functional perturbation theory

(DFPT) [46].

## 2.4 Heterostructure in Two-Dimensional - $WX_2$

Semiconductor heterostructure are of two and a greater number of layers grown vertically and have received high attention because of their adjustable electronic structures and optical properties [2]. The emergence of such ultra-thin TMDs materials as a new class of two-dimensional semiconductors, which are almost as thin, transparent, and flexible as graphene and rich in new physical phenomena [6, 47, 48], creates exciting new opportunities to push semiconductor heterostructures toward a new frontier [49, 50]. Vertically stacked van der Waals TMDs heterostructures are recognized as a powerful platform to create atomically thin heterostructures [51, 52, 53]. - Among the various stacking configurations, the two AA and AB stackings are the most frequently used in TMDs. While one layer in AB stacking is significantly moved with respect to the other by the hexagon lattice's edge length, the two levels in AA stacking have the same lateral coordinates.

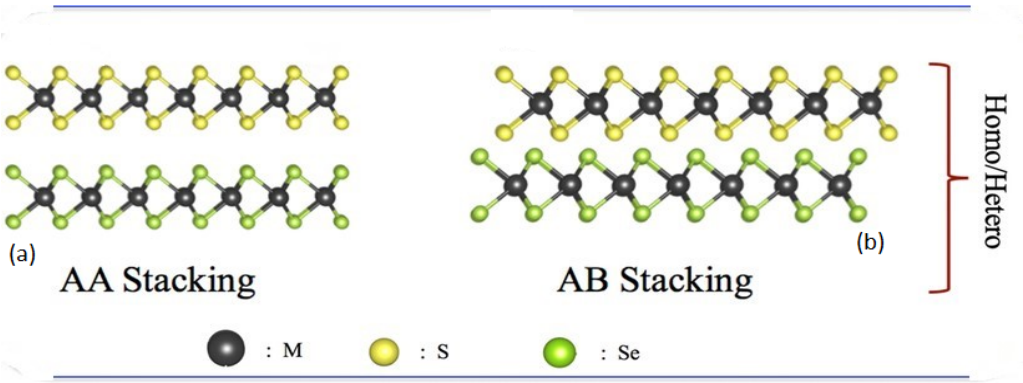


Figure 2.2: Heterostructure features of 2D-stacked $MX_2$ bilayers (a) AA stacking, (b) AB stacking

The AB-stacking heterostructure has a stronger interlayer coupling with a narrower band gap, larger band offset, and shorter interlayer distance than AA-stacking [54]. Consequently, compared to AA-stacking, the AB-stacking heterostructure produces a stronger piezoelectric response to strain with a bigger output voltage [55]. Such heterostructures have optically active band gap with bound electrons and holes limited in individual monolayers [56, 57]. Based

on the density functional theory (DFT) calculations, an interesting phenomenon is found that $MoS_2/WS_2$, $MoS_2/WSe_2$, and $WS_2/WSe_2$ heterostructures turn into direct-gap semiconductors from indirect-gap semiconductors with increasing the interlayer space. However, in those bilayer heterostructures, the change of the bandgap properties with interlayer spacing differs from each other. The results have been observed in the variable-temperature experiment and the results lead to new directions for various applications [58]. Strain engineering in TMDs monolayers, multilayers, and heterostructures is one of the methods to adjust the electronic structure or the band gap and optical properties of materials by the application of strain on it. Multilayer TMDs are predominantly interesting because they are known to exhibit interlayer exciton transitions where the electron-hole pairs are located in different constituent layers bounded by strong Coulomb interaction [38]. These interlayer excitons have been observed to be strain tunable in homobilayers of molybdenum disulfide ($MoS_2$) [39] and heterobilayers of molybdenum diselenide and tungsten diselenide ($MoSe_2/WSe_2$) [40] with deformation potentials of few millielectron volts.

The strain characteristics of momentum-space indirect interlayer exciton in a crumpled $MoS_2/WSe_2$ heterobilayer is investigated [59]. According to the theoretical calculations based on density functional theory (DFT) [60, 61], there is a considerable drop in the direct gap energy of the quasi-particle in $MoS_2$ with a biaxial strain. As biaxial strain is applied in $MoS_2$, an even greater fall in the indirect gap energy results, and a direct-to-indirect bandgap transition is confirmed. This is anticipated to occur in other families of 2D-TMDs as well. The practicality of strain-based band gap engineering of 2D semiconductors is demonstrated by the significant bandgap alterations achieved in both cases with the application of moderate strain levels. Many studies have experimentally proven that applying uniaxial and biaxial strain can tune the bandgap of mono and few layers homo or hetero structures of TMDs [62, 63].

## 2.5 Electronic and magnetic Properties of Two-Dimensional $WX_2$

### 2.5.1 Electronic properties

The band structure has been used to explain many important physical properties of a given material. In 2012, A. Kumar and P.K. Ahluwalia have performed an investigation of the electronic structure of all TMDs by using first principle calculations. The result of their investigations were in good agreement with the experimental measurements [64]. Family of tungsten dichalcogenide, $WS_2$, and $WSe_2$ [65] undergo a transition from indirect to direct gap when tuned from multilayer to monolayer. Many of the 2D TMDs show a number of interesting phases with unusual electronic properties including charge density wave (CDW) phases [66] and superconducting phases [67].

Due to their tunable direct band gaps, monolayer transition metal dichalcogenides (TMDs) are a preferred family of 2D materials. The range of these band gaps is also of interest to several scientific communities, who are looking for enhanced applications for them in electronic and optical devices [68, 69]. Due to their significant chemical and physical features molybdenum and tungsten dichalcogenides ($MoS_2$, $MoSe_2$, $WS_2$, $WSe_2$) with a band gap of 1.88, 1.57, 2.03, and 1.67 respectively have received high attention as a 2D-layered material [70]. The band gap values fall within the spectrum of photovoltaic materials. Moreover, 2D layered structures enable doping with additional atoms in substitution of one or more atoms to adjust and tune its electronic and optical properties [71, 72]. While the bulk material has an indirect band gap, the direct band gap is limited to mono-layered TMDs. First principles calculations show that direct band gap bi-layers with a range of 0.79 eV to 1.157 eV may be produced by alternating individual layers of distinct TMDs ($MoS_2$, $WS_2$, $WSe_2$, and $MoSe_2$) to build heterobilayers as shown in Figure 2.3 with specific stackings [73]. It is interesting to note that electrons and holes are concentrated in distinct layers and physically separated in this direct band gap.

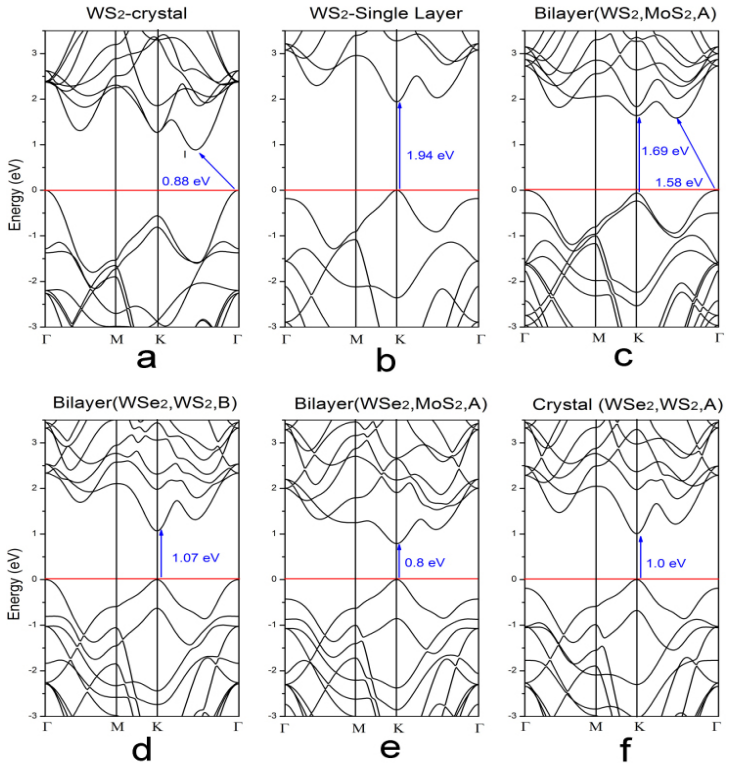


Figure 2.3: Band structure of transition metal dichalcogenides **a** - for bulk, **b**- for monolayer, **c** - for bilayer and **d-f** for heterostructure of different layers

### 2.5.2 Magnetism in Two-Dimensional $WX_2$ Doped with Transition Metals

The pristine monolayer transition metal dichalcogenides are nonmagnetic semiconductors [74, 75]. Thus, poor magnetism hinders their application in spintronic devices. Hence to broaden the applications of 2D-TMDs to spintronics it is essential to introduce the magnetic dopant into pure system in order to modulate electronic and magnetic properties. Transition metal element doping has been proven to be an effective means to introduce magnetism into 2D TMDs and has been widely used in many traditional magnetic semiconductors. Exploring the impact of transition metal doping on the magnetic properties of 2D-TMDs has the potential to advance the use of 2D TMDs in spintronics, and to introduce a new category of 2D magnetic materials for future technology. Currently in TMDs ($WX_2$), there are investigations supported by experiment [74] and theoretical simulations on monolayer TMDs by substitutional doping with different transition metals like Mn, Co, Fe and Ni instead of the molybdenum and tungsten atoms [74, 75, 76]. Still the magnetic properties of the doped monolayers and few layers of

TMDS with the selected transition metals is still not completely controlled open for further investigation.

Mn-doped $MoS_2$ [77] by first-principles calculations verified that the valley polarization depends on the strength of spin orbit coupling (SOC) and the exchange interaction. Separation of charge carriers in reciprocal space can lead to the formation of numerous quasi-particles including Dirac fermions [78], polaritons [79] and inter valley (bi)excitons [80, 81]. Several studies have been conducted on magnetism in W-based TMDs from bulk magnetization measurements. For instance, the formation of ferromagnetism conducted for Vanadium doped $WS_2$ [82] and $WSe_2$ [83] monolayers with ($\sim$ 0.5-4%) of V-content and these materials are classified as a dilute-magnetic semiconductor (DMS). Substitutional doping can bring new features in bandgap of TMDs, leading to variations in their electronic, optical and magnetic characteristics [72]. Doping a semiconductor with transition metals is a common method of making ferromagnetism for spintronic application in materials and such materials are known as diluted magnetic semiconductors (DMSs) [75, 84, 85], which provides an electronic means of manipulating magnetism since carriers mediate magnetism [86, 87]. TMDs are of particular importance among 2D semiconductors that can aid as a foundation for two dimensional diluted magnetic semiconductors (2D-DMSs). Greater magnetic anisotropy, which is necessary for magnetic order to exist in two dimensions [88] can result from TMD heavy atomic mass. Finding steady magnetic order in TMDs containing a transition metal impurity [89, 90, 91] has sparked additional interest in the area of TMDs based materials. DFT+U with Hubbard correction ($U_{eff}$) for Mn atom and high correlation effects are among the electronic and magnetic features of the Mn doped 2D-TMDs [92] and GGA+U becomes real. The Hubbard potential $U_{eff}$ strongly influences the impacts impurity states and the magnetic moment of impurity atom which signifies to a high spin state. When minority spin crosses the Fermi level, the occupied states clearly rise and the impurity states migrate to the valence band. In this scenario, the magnetic moment of the doped TMDs is greatly influenced by the significant correlation effects [93]. In Mn-doped monolayer $WSe_2$ it is revealed that the exchange interaction strongly depends on the spatial locations, concentrations, and distances between the dopant (Mn-Mn) atoms [92]. Under the effect of strain, which changes the way of charge distribution, the influ-

ence on the magnetic properties has also been investigated. This includes the coupling among orbitals of atoms $(Mn-3d, W-5d, Se-4p)$ and the potential for semiconductor spintronics is explored that Mn-doped $WSe_2$ monolayers under strain is promising for 2D-dilute magnetic semiconductors [93]. Magnetic response in Mn-doped bilayer $MoS_2$ is influenced by inter-layer interaction in a bilayer $MoS_2$ and estimated Curie temperature becomes higher than room temperature with noticeable variations for the dopant concentration and the neighboring distance $(Mn-Mn)$ between the impurity atoms [94].

The important parameter of a dilute magnetic semiconductor (DMS) is the Curie temperature ($T_C$) below which the system develops a long-range ferromagnetic ordering [modify]. The realization of two dimensional DMS and half-metallic behavior has received attention not only to enhance Tc but also due to both in fundamental aspects of physics [95, 96, 97] and for prospective applications such as the integration between 2D semiconductors and magnetic data storage enables the development of two dimensional spintronics devices such as spin valve and spin-based transistors [modfy]. It has been reported theoretically 2d DMS in ML MoS2 by replacing Mo by other transition metal atom [84] and their result demonstrate that room temperature 2d DMS can be achieved for the dopant concentrations in the range of 10-15 %. Besides, more recently room temperature ferromagnetism has been reported in manganese oxide doped $MoS_2$ experimentally [98]. The experimental measured intensity versus Raman shift for pure and Mn doped $MoS_2$ confirms that electronic state can be altered in the presence of magnetic impurities. In 2D-$WSe_2$, substitution of Ti and V results delocalized antiferromagnetism but localized ferromagnetism arises in doping with Cr, Mn, Fe, and Co [99].

Large magnetic moments and significant magnetic anisotropy is observed in single layer chromium trihalides with Curie temperatures as high as 90 K [100]. For monolayer VSe2, intrinsic ferromagnetism with lower limit, while increasing defect concentration will increase it to the upper limit and room-temperature ferromagnetism is confirmed [101]. Recently, clustering of dopant on $WSe_2$ doped with transition metals (Mn, Fe and V) made more stable than discretely doped and realized an interesting Curie temperature [102].

## 2.6 Optical Properties Two-Dimensional $WX_2$

The transition of the band gap has been studied theoretically and experimentally in the typical TMD, $MoS_2$, by DFT [103, 104] and angle-resolved photoelectron spectroscopy (ARPES) [105]. As the number of layers is reduced, there exists a point at which the band gap transitions from an indirect to a direct gap. Similar behaviour is predicted for other TMDs including tungsten dichalcogenides [104] and has been confirmed experimentally in $WS_2$ and $WSe_2$ [65] and $MoTe_2$ [106]. DFT simulations were used to determine the optical absorption characteristics of $WS_2$, and these characteristics make $WS_2$ a promising photovoltaic material [107]. $MoS_2$, $MoSe_2$, $WS_2$ and $WSe_2$ monolayers complex dielectric functions for photon energies between 1.5 and 3.0eV have been experimentally calculated and these materials have a peak absorbance of more than 15% and the dielectric functions predict extensive light-matter interactions in monolayers. Exciton splitting is extrapolated from the measured dielectric function in conformity with density functional models [108]. For 2D-$MoSe_2$ and 2D-$WSe_2$, the bi-axial strain has been used to identify the direct-to-indirect bandgap transition in compressive strain. It has also been reported that the peaks for real and imaginary values of the dielectric constant, optical absorption, and electron energy loss spectra, may allow for appealing applications for photovoltaic and electroluminescent devices. They were strong prospects for digital electronics and optoelectronics device applications due to their optical performance and light absorption under tensile strain [109]. As the layer number is reduced, the indirect PL peak moves to higher energy which indicates the increasing of band gap. The direct PL peak also becomes more intense with decreasing layer number [65]. Generally, the absorption spectrum of a 2D material within the infrared-visible part of the electromagnetic spectrum is dominated by a step function-like spectrum resulting from the joint density of states [110]. Doped TMD monolayers have also been observed to exhibit trion quasiparticles [111, 112], and there is evidence of bi-excitons [81, 113]in monolayer TMDs. A tunable excitonic LED has been demonstrated using monolayer $WSe_2$ p-n junctions [114]. Manipulation of the excitons can also allow for the nonlinear generation of light [115], by second-harmonic generation, which can be controlled electrically using a FET device structure [116]. Pure monolayer $WS_2$ system has larger absorption in range of 6-9.5ev and more suitable for high energy photodetectors but doped monolayer

$WS_2$ is preferable to make an infrared photodetector due to red-shift phenomenon near zero energy [117].

## 2.7 Applications of Two Dimensional-$WX_2$

2D TMD are considered to be promising materials for diverse applications including electronics, photonics, sensing, and energy storage [118, 119]. These applications are inspired by the unique properties of layered materials such as thin atomic profile that represents the ideal conditions for maximum electrostatic efficiency, mechanical strength, tunable electronic structure, optical transparency, and sensitivity [120]. Of particular interest for applications is flexible nanotechnology, which is considered for potentially ubiquitous electronics and energy devices that can benefit from the range of outstanding properties afforded by 2D materials. Flexible technology comprises a wide array of scalable large-area devices including thin film transistors (TFTs), displays, sensors, transducers, solar cells and energy storage on mechanically compliant substrates. Highly conductive nature together with large surface area, excellent chemical stability, and flexibility make 2D materials as suitable candidates for future technology applications [121].

# Chapter 3

# Methodology

## 3.1 Introduction

Computational simulations are growing in advance in theoretical materials science and engineering. These simulations are effective from different aspects in researching for new material innovations than the experimental method. First-principles calculations, which involve the density functional theory (DFT) has become vital tool in theoretical condensed matter physics research. Hohenberg and Kohn in 1964 [122] introduced the Density functional theory (DFT) [123] and currently this technique is one of the successful methods in quantum mechanical system of many body problems. A great range of material events have been successfully predicted, simulated, and explained by this approach with remarkable success. It has shown to be incredibly effective at characterizing the structural and electronic properties of a wide range of materials, from atoms and molecules to basic crystals and intricate extended systems [124].

According to the fundamental theory of DFT, properties of system of many interacting particles can be thought of as a functional $F[n]$ of the ground state density of the electrons $n(r)$. The first conceptual benefit of DFT is the ability to express an actual ground state property of a system in terms of its ground state electronic charge density [125]. This means that we can take essentially different approach and regard the electronic charge density, a simple scalar spatial coordinate function of $r$, as a fundamental quantity of the problem rather than immediately searching for the complex many-body wave-functions of a system. The ability to establish a

system of $N$ non-interacting Kohn-Sham electrons [126] in an effective Kohn-Sham potential $V_{KS}(r)$ with the same ground-state charge density onto a system of $N$ interacting electrons in an external potential $V_{ext}(r)$ is another fundamental concept of the density functional theory.

In this chapter, an overview of the fundamental theory (DFT) method in many body problems are discussed including the Born-Oppenheimer approximation, the Hohenberg-Kohn theorems as well as the Kohn-Sham equations of self consistent calculations. The local density approximation (LDA), the generalized gradient approximation (GGA) for calculation of the exchange-correlation, the spin polarized density functional theory and the Hubbard model for more accuracy and comprehensive output of the computations.

## 3.2 Challenges in Many-body Problems

The quantum mechanics of materials (condensed matter) needs the solution of Schrodinger equation of 3N spatial variables and N spin variables (for electrons) in a system of N number of particles. The fundamental challenge here is many-body problem (electrons and ions) for which the electrons strongly interact with each other. Their interactions govern the fundamental properties of several materials, ranging from metals and semiconductors to insulators. It is known that in a real solid, there are $10^{23}$ electrons interact to each other and with ion-cores to form crystal. In practice this is difficult to solve the wave equation for these interacting electrons and ion cores exactly. Because of this reality, the Schrodinger equation for many body problems is subjected to some reasonable approximation to overcome the problem with considerable range of errors.

### 3.2.1 The Born-Oppenheimer approximation

The Born-Oppenheimer (BO) approximation, which was introduced first by Max Born and J. Robert Oppenheimer that separates the motion of electrons and the nuclei. For a non-relativistic system of $N$-electrons (atom, molecule, or solid) the time independent Schrodinger equation for many body system can be given by;

$$\hat{H}\Psi(r_1, r_2, ..., r_N) = E\Psi(r_1, r_2, ..., r_N) \tag{3.2.1}$$

and the Hamiltonian (H) of electron-nuclei system is given by

$$\hat{H} = -\frac{\hbar^2}{2m_e}\sum_{i=1}^{N}\nabla_i^2 - \frac{\hbar^2}{2M_N}\sum_{i=1}^{N}\nabla_i^2 + \frac{1}{2}\sum_{i\neq j}\frac{e^2}{|r_i - r_j|} - \sum_{i,I}\frac{Z_I e^2}{|r_i - R_J|} + \frac{1}{2}\sum_{I\neq J}^{N}\frac{Z_I Z_J e^2}{|R_I - R_J|} \tag{3.2.2}$$

where, $Z_I$ and $R_I$ represent charges of the nuclei and location of the nuclei respectively [125]. The Hamiltonian is expressed in terms of;

- kinetic energy of the electron

$$\hat{T}_e = -\frac{\hbar^2}{2m_e}\sum_{i=1}^{N}\nabla_i^2 \tag{3.2.3}$$

- kinetic energy of the nuclei

$$\hat{T}_N = -\frac{\hbar^2}{2M_N}\sum_{i=1}^{N}\nabla_i^2 \tag{3.2.4}$$

- the electron-electron interaction

$$\hat{V}_{e-e} = \frac{1}{2}\sum_{i\neq j}\frac{e^2}{|r_i - r_j|} \tag{3.2.5}$$

- the electron-nuclei interaction, and

$$\hat{V}_{e-N} = -\sum_{i,I}\frac{Z_I e^2}{|r_i - R_J|} \tag{3.2.6}$$

- the nuclei-nuclei interaction

$$\hat{V}_{N-N} = \frac{1}{2}\sum_{I\neq J}^{N}\frac{Z_I Z_J e^2}{|R_I - R_J|} \tag{3.2.7}$$

The nuclei-nuclei interaction potential ($\hat{V}_{N-N}$) and kinetic energy ($\hat{T}_N$) of the nuclei in Born-Oppenheimer approximation are ignored. In this approximation, the response of the electrons to an external perturbation is much faster than that of the nuclei since the nuclei has much heavier mass than the electrons. In addition, the nuclei-nuclei repulsion is fixed for a given

nuclear geometry and the electrons could follow any movement of the nuclei almost instantly and could essentially move in a constant field that the nuclei at fixed places generated. Applying the Born-Oppenheimer approximation and replacing atomic units, the equations (3.2.2 to 3.2.7) can be modified more simpler way. Thus, the simplified form of Hamiltonian of the system is given as

$$\hat{H} = \hat{T}_{ee} + \hat{V}_{ee} + \hat{V}_{en}. \tag{3.2.8}$$

### 3.2.2 Hartree-Fock Approximation

Hartree presented a method for approximating the Schrodinger equation that he named the self-consistent field (scf) method. The energy and wave function of a quantum many-electron system in a stationary state are approximated using the Hartree method. The approximation assumes that the exact N-body wave function of the system can be approximated by a product of single electron wave function. Hartree approximation, muti-electron wavefunction, $\Psi(r_1, r_2, ..., r_N)$ of equations -3.2.1 can be expanded as a product of single electron wavefunction (orbitals)

$$|\psi(r_1, r_2, ..., r_N)\rangle \approx \psi(r_1)\psi(r_2)...\psi(r_N) \tag{3.2.9}$$

It assumes that electrons independent and interact only via mean field coulumb potential which yields one - electron Schrodinger equation of the form

$$[-\frac{\hbar^2}{2m}\nabla^2 + V(r)]\psi_i(r) = \varepsilon_i\psi_i(r). \tag{3.2.10}$$

The potential V(r), includes electron-electron and electron-ion interactions (equations -3.2.5 and 3.2.6) respectively. The charge density

$$n(r) = \sum_{i}^{occupied} |\psi(r)|^2 \tag{3.2.11}$$

The Hartree equations are nonlinear and must be solved iteratively by starting with trial electron charge density using the algorithm shown below (Figure-3.1)

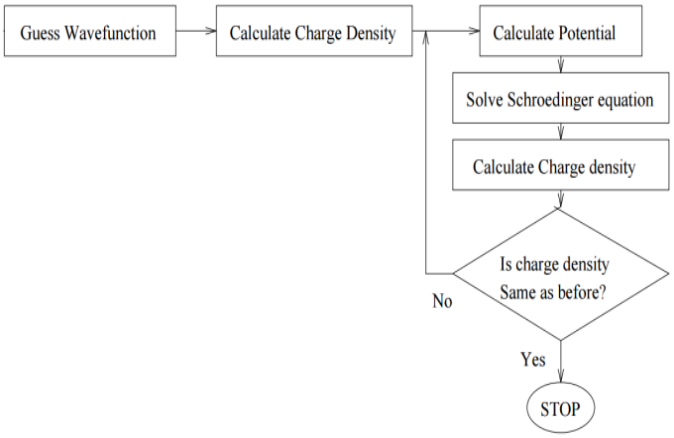


Figure 3.1: Hartree self-consistent-field algorithm

Fock improved the Hartree method by using untisymmetrized wavefunction instead of single electron wavefunction that is the Hartree Fock method. The spatial distribution of electrons in a molecule can be described by spatial orbitals $\phi(r)$. However, a spatial orbital is not sufficient to completely describe an electron since it is necessary to specify its spin. It is possible to define a function which describes simultaneously the spin and spatial distribution of the particles. The Pauli exclusion principles demands that the many body wave function must be anti-symmetric with respect to interchange of any two electron (fermionS) coordinates.

$$\psi(r_i, r_j) = -\psi(r_j, r_i) \tag{3.2.12}$$

In the Hartree model, the trial many-electron wavefunction (Equation-3.2.9) did not satisfy the required fermionic antisymmetry. Now we consider the case of two electrons with spin. The total wavefunction is then expressed as

$$\psi(1,2) = \phi(r_1, r_2)\chi(\sigma_1, \sigma_2) \tag{3.2.13}$$

where $\sigma_i$ is the spin degree of freedom of electron i and $\chi$ is the total spin wavefunction. Now, the overall antisymmetry of the wavefunction $\psi$ is satisfied by two combinations: $\phi_s\sigma_a$, singlet spin state, or, $\phi_a\sigma_s$, triplet spin state. The subscripts s, a refer to symmetric and antisymmetric, respectively.

Therefore, it is appropriate to consider a Slater determinant of single-particle wavefunctions

instead, as

$$\psi(r_1, r_2, ..., r_i, ..., r_N) = \frac{1}{\sqrt{N!}} \begin{vmatrix} \psi_1(r_1) & ... & \psi_i(r_1) & ... & \psi_N(r_1) \\ ... & ... & ... & ... & ... \\ \psi_1(r_N) & ... & \psi_1(r_N) & ... & \psi_N(r_N) \end{vmatrix} \tag{3.2.14}$$

where the $\psi_i$s are products of spin and space wave functions. Depending on the parity of permutation, the N! determinant terms are each multiplied by either -1 or 1. The concept of HF-method can be found in more detail on various quantum mechanics text books including [127, 125].

## 3.3 Density Functional Theory (DFT)

For system of many body problems, solving the Schrodinger equation is highly challenging and additional strategies are required to tackle such problems and one of these techniques is the density functional theory. Density functional theory (DFT) is a quantum-mechanical modeling technique that is used in various disciplines to calculate a wide range of atomic system characteristics. DFT belongs to the family of first principles (ab initio) methods, so named because it can predict material properties for unknown systems from scratch without any experimental input. Moreover, DFT has earned popularity due to the relatively low computational effort required. The Schrodinger equation for $N-$numbers of particles with Born-Oppenheimer approximation into consideration for the Hamiltonian given as in equation 3.2.1 is

$$\hat{H}\psi(r_i) = E\psi(r_i), \tag{3.3.1}$$

In this context, the ground-state energy $E_0$ is the quantity that is of primarily interest. The following minimization yields $E_0$, according to the variational theorem. The variation theorem states the lowest energy associated with the Schrodinger equation,(3.3.1), is the ground state energy given by

$$E_0 = min_\psi \langle \psi | H | \psi \rangle . \tag{3.3.2}$$

The true ground state energy of a system is a minimum of the functional $F[n]$, and the density that minimizes the functional is the true density of the electrons in their ground state. For the hypothetical Kohn-Sham system, the universal density-functional, $F[n(r)]$, corresponds to the kinetic energy of the non-interacting electrons, $T_0[n(r)]$. For the interacting electron system, $F[n(r)]$ can then be expressed as the sum of the kinetic energy of the non-interacting electron gas with the same density and the additional terms describing the inter-particle interactions as

$$F[n(r)] = T_0[n(r)] + \frac{1}{2}\int \frac{n(r)n(r')}{|r-r'|}drdr' + E_{xc}[n(r)], \tag{3.3.3}$$

where,

$\int \frac{n(r)n(r')}{|r-r'|}drdr'$ is the classical Coulomb electron-electron repulsion, and $E_{xc}[n(r)]$ is the exchange-correlation energy which accounts for all the many-body effects which is not described in the first two terms. The total energy functional of the original system of interacting electrons in general becomes,

$$E = T + V + \frac{1}{2}\int \frac{n(r)n(r')}{|r-r'|}drdr' + E_{xc}. \tag{3.3.4}$$

### 3.3.1 The Hohenberg-Kohn Theorems

Hohenberg and Kohn (HK) published two essential theorems in 1964 and these theorems laid the foundation for the modern density functional theory [122]. The first theorem states that for non-degenerate ground electronic state, the density of an interacting system uniquely determines all properties including the wave function and energy of the ground as well as the exited state. More precisely, all properties of systems are completely determined given only the ground state density $n_0(r)$. Applying equation (3.2.8) for the ground state electrons the density functional becomes

$$E[n_0] = T_e[n_0] + V_{ee}[n_0] + V_{ne}[n_0] = E_0. \tag{3.3.5}$$

Where the functionals $T_e[n_0]$, $V_{ee}[n_0]$, $V_{ne}[n_0]$ designate the expectation values of the kinetic-energy, electron-electron repulsion and the electron-nuclear attraction interactions respectively.

The second HK theorem states that for every external potential $V_{ext}(r)$, a universal functional for the energy $E[n]$ in terms of the density $n(r)$ can be defined. The global minimum value of this functional, for any of the given $V_{ext}(r)$, represents the exact ground state energy of the system. Therefore, the exact ground state density, $n_0(r)$, is the density that minimizes the energy functional. For any arbitrary density function $n(r)$ with $n(r) \geqslant 0$, the density that minimizes the total energy is the exact ground state density and the ground state energy can be derived in variation as

$$E[n] > E[n_0] = E_0. \tag{3.3.6}$$

By adjusting the electron density to determine the ground-state electron density, one can attempt to reduce the energy. If the true functional form is known all of the attributes can be computed once the ground-state electron density is determined exactly. The detail proof of the HK theorems are found in many standard condensed matter physics books [125, 128] and others.

According to Hohenberg and Kohn formalism, the ground state energy depends on the density of electrons and the minimum energy is determined by the ground state density $n_0$. Thus, minimizing the total energy of the system with respect to variations in the density function $(n(r))$ would result the exact ground state density and energy. The HK approach formulates DFT as an exact theory of many-body systems. The formulation is applicable to any system of interacting particles in an external potential $V_{ext}(r)$, and the Hamiltonian, $\hat{H}$ is determined as

$$\hat{H} = -\frac{1}{2}\sum_i \nabla_i^2 + \sum_i V_{ext}(r_i) + \frac{1}{2}\sum_{i\neq j}\frac{1}{|r_i - r_j|} \tag{3.3.7}$$

The ground state wave function $\Psi[n]$, for the potential $v(r)$ itself is a function of $n$, Hohenberg and Kohn took use of it to define the universal density functional as

$$F[n] = \left\langle \Psi[n] | \hat{T} + \hat{V_{ee}} | \Psi[n] \right\rangle, \tag{3.3.8}$$

which could be used to express the total electronic energy functional

$$E[n] = F[n] + E_{ext}(r). \tag{3.3.9}$$

Using external energy, $E_{ext}[n]$, for the system specific external potential

$$V_{ne}(r) = \int v_{ne}(r)n(r)dr.$$

It should be noted that for degenerate ground states, $\Psi[n]$ is not unique and can refer to any degenerate ground-state wave function. However, all $\Psi[n]$ give the same $F[n]$, indicating that $n$ has a unique functional.

Hohenberg and Kohn further showed that the density functional $E[n]$ satisfies a variational property so as the ground-state energy $E_0$ of the system considerably obtained by minimizing this functional with respect to $v$ which is function of the density $n(r)$.

$$E_0[n] = min_n\Big\{F[n] + \int v_{ne}(r)n(r)dr\Big\}, \tag{3.3.10}$$

the minimum being reached for a ground-state density $n_0(r)$ corresponding to the potential $V_{ne}(r)$.

### 3.3.2 Kohn-Sham Equations

Hohenberg-Kohn and Sham introduced the significant turning point in the advancement of DFT in 1965. The Kohn-Sham (KS) equations [126] consist of N-single particle Schrödinger equations with a modified effective potential ($V_{KS}$) more advanced and much easier to solve than the real many-body problem and more preferable than the previous approach. The KS-formalism centers on mapping the full interacting system, onto a virtual non-interacting system. However, Kohn-Sham equations incorporate the correlation of electrons in addition to exchange interactions. Each electron flows independently in a potential formed by the ion and other electrons in the Kohn-Sham method to non-interacting electrons, where the ground state density is thought to be the same as the real system. According to Kohn-Sham, the energy functional can be written as

$$E_n = T_s[n] + E_{ext}[n] + E_H[n] + E_{xc}[n], \tag{3.3.11}$$

for the Hartree potential of the electron-electron repulsion

$$E_H[n(r)] = \frac{1}{2}\int\int \frac{n(r)n(r^{'})drdr^{'}}{|r-r^{'}|}, \tag{3.3.12}$$

and

$$E_{ext}[n(r)] = \int n(r)V_{ext}(r)dr \tag{3.3.13}$$

represents energy due to electron-nuclear interaction and $E_{xc}[n]$ is the exchange-correlation functional which is discussed in the next section 3.4.

Thus, the effective potential $(V_{eff})$ in Kohn-Sham approach is then given by

$$v_{eff}(r) = \frac{\partial E[n(r)]}{\partial n(r)} = v_{ext}(r) + \frac{1}{2}\int \frac{n(r^{'})dr^{'}}{|r-r^{'}|} + \frac{\delta E_{xc}}{\delta n(r)} \tag{3.3.14}$$

where, on the right hand side of equation, the first term is external potential, the second term is Hartree potential and the third term

$$v_{xc} = \frac{\delta E_{xc}}{\delta n(r)} \tag{3.3.15}$$

is exchange-correlation potential. The kinetic energy functional for non-interacting electrons with total ground state density $n_0$ is given by

$$T_s = -\frac{1}{2}\int \phi_k^*(r)\nabla^2\phi_k(r)dr. \tag{3.3.16}$$

Finally, the equations (3.3.11 - 3.3.16) lead to basic equation in Kohn-Sham DFT which is the one-electron Schrodinger equation expressed as

$$\left(-\frac{\nabla^2}{2} + v_{eff}\right)\phi_n = \varepsilon_n\phi_n. \tag{3.3.17}$$

Where the Kohn-Sham one electron orbitals $(\phi_n)$ and the corresponding electron number density is given by as

$$n(r) = \sum_n |\phi_n(r)|^2, \tag{3.3.18}$$

results with the total energy of the system,

$$E_s = \sum_n \varepsilon_n, \tag{3.3.19}$$

The derivation of the single-particle Kohn-Sham equation (3.3.17) from the many-body Schrodinger equation where all interaction terms in equation (3.3.15) are known, the solution of the problem would be exact.

## 3.4 Approximations for the Exchange-Correlation ($E_{xc}$) and Self-Consistent Calculations

The Kohn-Sham equations provide a theoretically exact method for finding the ground state energy of an interacting system provided that the form of exchange-correlation is known. Unfortunately, the exact analytical expression of the exchange-correlation interaction $v_{xc}$ is not known exactly. $E_{xc}$ is exact for a uniform electron gas and is considered to be a reasonable approximation for slowly varying densities. Various approximations can be used for this correction and they usually determine the accuracy of the calculations. The most commonly used approximations are the local density approximation (**LDA**) and the generalized gradient approximation (**GGA**), which are presented below.

### 3.4.1 The Local Density Approximation (LDA)

The local density approximation (LDA) is one of the first and most standard approximation for the exchange-correlation interaction. In local density approximation, the exchange-correlation functional depends on the density of electrons. It assumes that the exchange-correlation energy of the system is equal to an integral of a homogeneous electron gas with the density $n(r)$. The exact expression of the exchange-correlation energy of such a homogeneous electron gas is taken as,

$$E_{xc}[n] = \int d^3 r n(r) \varepsilon_{xc}(n). \tag{3.4.1}$$

Where $\varepsilon_{xc}(n)$ is the exchange-correlation energy of uniform electron gas with density n for,

$$n(r) = \sum_{i=1}^{N} |\psi_i(r)|^2. \tag{3.4.2}$$

By this formulation, the original many-body problem become simplified into a set of single-particle equations that has to be solved self-consistently. The LDA approximation is satisfactory for system with a low spatial variations of the electron density. The approximation also applicable for various types of materials. However, it significantly fails in the description of many properties of transition metals of $(d)$ and $(f)$ block elements and their compounds. Binding energies are in particular overestimated for LDA approximation [129].

### 3.4.2 The Generalized Gradient Approximation (GGA)

The generalized gradient approximation (GGA) is physically more appropriate for the exchange-correlation interaction, which includes non-uniform character of the electron density and the magnitude of its gradient $\nabla n(r)$. The generalized gradient pproximation is a more elaborated approximation of the exchange-correlation interaction, which consists in taking into account the non-uniform character of the electron density by replacing $\varepsilon_{xc}$ with semi-local function of the electron density and the magnitude of its gradient as various GGAs are successful for many cases in which the electrons have stronger effects of correlations, such as transition metals [125]. The exchange-correlation function with GGA is therefore,

$$E_{xc}[n] = \int f(n(r), |\nabla n(r)|) d^3r. \tag{3.4.3}$$

where $f$ is an analytical function which can also be described in various ways. The most common ones are the Perdew-Burke-Ernzerhof (PBE) [130] and the Perdew-Wang (pw) [131] parametrizations. For most materials, GGA improves the LDA over-binding. However, both GGA and LDA approximations are known to underestimate the band gap of semiconductors to inaccurately describe the band structure of strongly correlated materials. In some cases, both the LDA and GGA approximations predict a metallic behavior for instance in Mott insulators [132] whereas the materials are insulators. The failure of standard DFT (LDA and GGA)

is generally attributed to the use of a local potential to treat exchange many-body electron correlations.

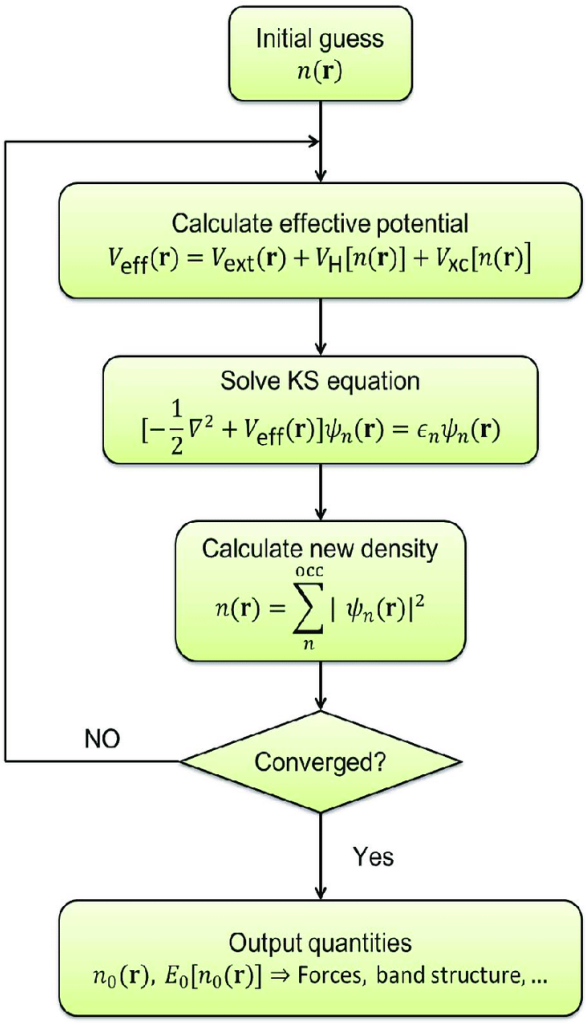


Figure 3.2: Kohn-Sham Self Consistent Field Calculations (SCF) loop

### 3.4.3 Self Consistent Calculations in DFT

The Kohn-Sham equation, the $E_{xc}$ of equation (3.3.17) can be solved interactively. A self-consistent iterative procedure would start from an initial electron density that can be used to calculate the KS potential $v_{KS}$. Then, through solution of equation (3.3.18), we can obtain a new electron density continuously following steps. The obtained results reveal that the ground state density is the density that minimize the total energy, such ground state density $n_0(r)$ can be found in iterative method which is self consistent as shown in Figure 3.2 and following the

listed steps below here:

1. First defining an initial and the trial electron density, $n(r)$.

2. Inserting the density, into equation (3.3.14) to construct new effective (KS) potential, $V_{eff}(r) = V_{KS}$, which depends on density $n(r)$.

3. Using $V_{eff}[n(r)]$ obtained from step two to solve Kohn-sham orbital equation in equation (3.3.18)

4. Computation of the new Kohn-sham orbitals using equation (3.3.17).

The steps followed to do the self-consistent calculation is to make initial trial guess for the wave functions of all electrons and calculate its effective Kohn-Sham potential, $V_{eff}$. Based on this effective potential the Kohn-Sham equation is solved to get a new wave function. From this, a new $V_{eff}$ is calculated, and so on. The procedure is terminated when the charge density does not vary much any more. At this point, the wave function and the effective potential are self-consistent with each other.

For complete description of the property of materials the standard DFT of the local density approximation (LDA) or generalized-gradient approximation (GGA) is not satisfactory. Therefore, extending DFT with important modifications to some comprehensive approaches become important. For instance, spin-polarization (Spin polarized DFT) to treat the electron spin, Hubbard corrections (LDA+U and GGA+U) to consider correlation effect and other corrections are currently available.

## 3.5 Spin polarized Density functional Theory

In density functional theory (DFT), particles interacting in electrostatic external potential is considered in the above sections. This functional theory can also be extended to a system in the presence of the magnetic interactions. The importance of including the effects of an external magnetic field is to consider more comprehensive and physically realistic approximation about the material. Within this model, one can rigorously generalize all the above arguments to

include two types of densities, the charge density $n(r)$ and the spin (magnetization) density $m(r)$. Thus, in spin-polarized system, magnetization density, $m(r)$, in addition to the charge density, $n(r)$, is to be taken into account irrespective of the DFT. In spin-density-functional theory the electronic (charge) density, $n(r)$, is scalar whereas the magnetization density, $m(r)$, is vector. Therefore, the spin-polarized DFT can be revised including spin system and the charge density, $n(r)$, and magnetization density, $m(r)$, can be related in terms of spin-up density $n\uparrow(r)$ and spin-down density $n\downarrow(r)$ as

$$n(r) = n\uparrow(r) + n\downarrow(r) \tag{3.5.1}$$

and

$$m(r) = n\uparrow(r) - n\downarrow(r) \tag{3.5.2}$$

In spin polarized DFT, the Hohenberg-Kohn theorem is generalized to state that the true ground state energy is variational functional of the spin densities. The coulomb terms remain functional of the total density but the kinetic of the electron $T_s$ and exchange-correlation energy ($E_{XC}$) become functional of the two densities. Therefore, the energy functional in equation(3.3.11) now modified in spin polarized DFT to

$$E[n^{\alpha\beta}(r)] = T_s[n^{\alpha\beta}(r)] + \int\int \frac{n(r)n^{'}(r)}{|r-r^{'}|}drdr^{'} + \int V_{ext}^{\alpha\beta} n^{\alpha\beta}(r) + E_{ext}[n^{\alpha\beta}(r)] \tag{3.5.3}$$

where $\alpha$ and $\beta$ are spin indices and can have two values either spin-up ($\uparrow$) or spin-down ($\downarrow$) and the kinetic energy functional and electron density are given by

$$T_s = -\frac{1}{2}\sum_{n=1}^{N}\int \phi_n^{*\alpha}(r)\nabla^2\phi_n^{\beta}(r)dr \tag{3.5.4}$$

and

$$n^{\alpha\beta}(r) = \sum_{n=1}^{N}\phi_n^{*\alpha}(r)\phi_n^{\beta}, \tag{3.5.5}$$

where the sum over includes all occupied orbitals.This, leads to the Kohan-Sham equations

$$-\nabla_r^2 \phi_i^\beta(r) + \sum_\beta V_{eff}^{\alpha\beta} \phi_i^\beta(r) = \varepsilon_i \phi_i^\beta(r) \tag{3.5.6}$$

The effective one particle potential in equation (3.5.6) is given by

$$V_{eff}^{\alpha\beta}(r) = \delta^{\alpha\beta} \int \frac{n(r')}{|r-r'|} dr' + V_{ext}^{\alpha\beta}(r) + V_{xc}^{\alpha\beta}(r) \tag{3.5.7}$$

## 3.6 Hubbard model (DFT+U method)

The description and understanding of electronic structure for strongly correlated materials is a very important in ab initio calculations. Both the LDA and GGA approximations are not always accurate enough for calculating material properties of partially filled d and f orbitals [43, 133]. For systems containing a partially filled d or f shell one obtains a partially-filled band with a metallic-type electronic structure. All these errors lead the DFT to dramatic failures in predicting the insulating character of Mott insulator, where the insulating character of the ground state arises from the strong Coulomb repulsion between electrons that prevail over the kinetic energy, forcing the electrons to localize on atomic-like orbitals. To rationalize the physics of correlated materials, the most reliable method is the Hubbard model [132, 133, 134] . In general, the Hubbard Hamiltonian is given by

$$H = -t \sum_{\langle i,j \rangle, \sigma} (c_{i,\sigma}^\dagger c_{j,\sigma} + h.c.) + U \sum_i n_{i\uparrow} n_{j\downarrow} \tag{3.6.1}$$

where $\langle i, j \rangle$ represents nearest-neighbor atomic sites. $c_{i,\sigma}^\dagger$ and $c_{j,\sigma}$ are the creation and annihilation operator for electrons of spin $\sigma$ on atomic site i respectively and $n_{i\sigma} = c_{i,\sigma}^\dagger c_{i,\sigma}$ is the number operator.

In normal materials, the hopping term dominates ($t \gg U$) and the problem could be described well by the standard DFT. In contrast, in the correlated materials the second term prevails so that electrons cannot hop easily because a sufficient energy is required to overcome the large Coulomb repulsion from other electrons on neighbor sites. In other words, the large Coulomb

repulsion makes the electrons more localized, resulting in an insulating behavior. In the large U limit, the Hubbard model gives an atomic-picture-like solution. In DFT+U method, the orbital-dependent Coulomb **U** and exchange-interactions **J** is added onto some localized states of the system, which have not been considered in standard DFT. So that the delocalized states are treated by normal DFT only whereas the localized states are treated by the Hubbard model in DFT+U. The on-site Coulomb U and exchange J corrections on some localized states, the DFT+U method gives a qualitative improvement [43]. More over, integration of U and J does not significantly disrupt the computational result compared to DFT. So that the DFT+U method ts proper to study the Mott insulators such as transition metal and rare-earth metal oxides, long ranged ordered magnetism [43]. The total energy in DFT+U is typically the summation of the standard DFT energy functional $E_{DFT}$ for all the states and the energy of the Hubbard functional $E_{Hub}$ minus the double counting term ($E_{dc}$) that describes the correlated states [43]. Then the total energy in DFT+U is [135],

$$E_{DFT+U}[n(r)] = E_{DFT}[n(r)] + E_{Hub}[n^{I\sigma}_{mm'}] - E_{dc}[n^{I\sigma}]. \tag{3.6.2}$$

Where $I$ is the atomic site index, $\sigma$ denotes the spin index, and $m$ and $m'$ are magnetic quantum numbers associated with specific angular momentum and $n^{I\sigma}_{mm'}$ is the occupation matrix measuring the occupation of the localised orbitals ($d$ or $f$ ) at site $I$ [134, 136]. The double counting term $E_{dc}[n^{I\sigma}]$ is so important because in $E_{DFT}[n(r)]$ partial exchange-correlations have already been taken into account, the interactions contained in DFT should be eliminated from the additive Hubbard correction to avoid double counting in $E_{Hub}[n^{I\sigma}_{mm'}]$. The occupation numbers $n^{I\sigma}_{mm'}$ is usually defined as projections of occupied Kohn-Sham orbitals $\Psi^{\sigma}_{nk}$ onto the states of a localized basis set $\varphi^{I}_{m}$:

$$n^{I\sigma}_{mm'} = \sum_{nk} f^{\sigma}_{nk} \langle \Psi^{\sigma}_{nk} | \varphi^{I}_{m} \rangle \langle \varphi^{I}_{m} | \Psi^{\sigma}_{nk} \rangle, \tag{3.6.3}$$

where the coefficients $f^{\sigma}_{nk}$ represent the occupations of Kohn-Sham states $\Psi^{\sigma}_{nk}$, determined by the Fermi-Dirac distribution with n and k being the band and k-point indexes, respectively. Index m labels the localized states of the same atomic site I. The energy functional of 3.6.3 is

reformulated [132, 133, 137] for the on-site Coulomb interaction U as

$$E_{DFT+U}[n(r)] = E_{DFT}[n(r)] + \sum_I \frac{U^I}{2} \sum_{m,\sigma \neq m'\sigma'} n_m^{I\sigma} n_{m'}^{I\sigma'} - \sum_I \frac{U^I}{2} n^I (n^I - 1). \tag{3.6.4}$$

where,

$$E_{Hub} = \sum_I \frac{U^I}{2} \sum_{m,\sigma \neq m'\sigma'} n_m^{I\sigma} n_{m'}^{I\sigma'}, and$$

$$E_{dc} = \sum_I \frac{U^I}{2} n^I (n^I - 1)$$

and $n_m^{I\sigma}$ are the diagonal elements of occupation number matrix, $n_m^{I\sigma} = n_{mm}^{I\sigma}$, and

$$n^I = \sum_{m,\sigma} n_m^{I\sigma}. \tag{3.6.5}$$

With these relations, equation 3.6.4 become

$$E_{DFT+U}[n(r)] = E_{DFT}[n(r)] + \sum_I \frac{U^I}{2} [\sum_{m,\sigma} n_{mm}^{I\sigma} - \sum_{m,\sigma} n_{mm}^{I\sigma} n_{mm}^{I\sigma}]. \tag{3.6.6}$$

Taking the variational derivative of the $DFT+U$ energy functional $E_{DFT+U}[n(r)]$ with respect to $\langle \varphi_m^I |$ we obtain

$$E_{DFT+U}[n(r)]|\Psi_{nk}^{\sigma}\rangle = E_{DFT}[n(r)]|\Psi_{nk}^{\sigma}\rangle + \sum_{I,m} U^I (\frac{1}{2} - n_m^{I\sigma}) |\varphi_m^I\rangle \langle \varphi_m^I | \Psi_{nk}^{\sigma}\rangle. \tag{3.6.7}$$

As obvious from equation 3.6.7, the Hubbard potential (the last term of 3.6.7) is repulsive for less than half-filled orbitals $n_m^{I\sigma} < \frac{1}{2}$, whereas it is attractive for more than half-filled orbitals $n_m^{I\sigma} > \frac{1}{2}$. This means that the DFT+U method favors the localization of electrons, i.e $n_m^{I\sigma} \to 1$ or $n_m^{I\sigma} \to 0$. For an occupied band, the energy is increased by $\frac{U^I}{2}$, while for an unoccupied band the energy is decreased by $\frac{U^I}{2}$. Therefore, an energy gap appears with the size of approximately $U^I$, consistent with the picture of the Hubbard model. Finally we get the required Hubbard

potential $V_u$ in the last term of equation 3.6.7 as

$$V_u = \sum_{I,m} U^I (\frac{1}{2} - n_m^{I\sigma}) |\varphi_m^I\rangle\langle\varphi_m^I|. \tag{3.6.8}$$

Next we have an expression for the modified Kohn-Sham equations by taking functional derivatives of the DFT+U total energy functional with respect to the complex conjugate Kohn-Sham wave function;

$$\big[-\frac{1}{2}\nabla^2 + \hat{V}_{ks}^{\sigma} + \hat{V}_U^{\sigma}\big]\Psi_{nk}^{\sigma} = \varepsilon_{nk}^{\sigma}\Psi_{nk}^{\sigma}, \tag{3.6.9}$$

where, $V_{ks}$ is given as

$$\hat{V}_{ks}^{\sigma} = \hat{V}_{DFT} = \hat{V}_{ne} + \hat{V}_H + \hat{V}_{xc}^{\sigma}, \tag{3.6.10}$$

where the first and second terms in equation 3.6.10 are operators that correspond to the electron-ion interaction and electron-electron interactions respectively, and the third term exchange correlation potential$V_{xc}$, which can be given as:

$$V_H = \int_V \frac{\sum_\sigma \rho^\sigma(r')}{|r-r'|} dr', \tag{3.6.11}$$

where V is the volume the crystal and,

$$\hat{V}_{xc}^{\sigma} = \frac{\delta E_{xc}}{\delta \rho^\sigma(r)}, \tag{3.6.12}$$

where, $\rho^\sigma(r)$ is spin charge density

$$\rho^\sigma(r) = \sum f_{nk}^{\sigma} |\Psi_{nk}^{\sigma}|^2,$$

and the Hubbard potential, $V_u^\sigma$ with effective Hubbard parameter $(U_{eff} = U^I - J^I)$ is

$$V_U^{\sigma} = \sum_{I,m,m'} U_{eff}^I \big(\frac{\delta_{mm'}}{2} - n_{mm'}^{I\sigma}\big) \big|\varphi_m^I\big\rangle\big\langle\varphi_{m'}^I\big|, \tag{3.6.13}$$

From a piece-wise linearity condition implemented in DFPT, we obtain Hubbard parameters by methods of the linear-response theory [136, 138].we recall basic aspects of the linear response constrained density functional theory(LR-cDFT) approach as in [138] for calculations of the effective Hubbard parameter U. In this approach DFPT-based reformulation of linear response constrained density functional theory is used. The Hubbard parameters are constituted of an effective interaction matrix, which is estimated from the difference between raw and screened inverse susceptibilities. With this method, U is computed as the second derivative of the total energy of the system with respect to atomic occupations that are defined as the 'on-site' trace of the occupation matrices, $n^I = \sum_\sigma Tr[n^{I\sigma}] = \sum_{\sigma,m} n^{I\sigma}_{mm}$. However, in applications of DFT, where a plane-wave basis set and pseudopotentials are used, atomic occupations are obtained as output quantities (developed from the solution of the KS equations) and cannot be controlled from input. To overcome this problem, the LR-cDFT method performs a Legendre transformation of the total energy. In application, the total energy functional $E_{DFT}[\rho_\sigma]$ is augmented with a linear combination of the products of atomic occupations $n^I$ and Lagrange multipliers $\{\lambda_I\}$. Then, this functional is minimized with respect to the spin charge densities $\rho_\sigma$ which gives the ground-state energy as a function of the coefficients $\{\lambda_I\}$,

$$E\{\lambda^I\} = min_{\rho_\sigma}\left\{E_{DFT}[\rho_\sigma] + \sum_I \lambda^I n^I\right\}, \tag{3.6.14}$$

this gives the total energy as a function of the ground-state atomic occupations $n^I$ is recovered by a Legendre transformation,

$$E(\{n^I\}) = E(\{\lambda^I\}) - \sum_I \lambda n^I, \tag{3.6.15}$$

Here, this definition of the total energy, equation (3.6.15), can be used to evaluate derivatives with respect to $n^I$. Based on these definitions, the first and second derivatives gives

$$\frac{dE}{dn^I} = -\lambda^I \tag{3.6.16}$$

$$\frac{d^2E}{(dn^I)^2} = -\frac{\lambda^I}{dn^I} = -\left(\chi^{-1}\right)_{II} \tag{3.6.17}$$

This represents the form in which the final equality determines the response matrix $\chi$. This matrix contains the response of atomic occupations to the potential shift used to perturb the ground state of the system as given in equation (3.6.13), $\chi_{IJ} = \frac{dn^I}{d\lambda^J}$ (I and J being atomic indices). Now from linear-response theory, the Hubbard U parameter is will be,

$$U^I = \left(\chi_0^{-1} - \chi^{-1}\right)_{II} \tag{3.6.18}$$

where $\chi_0$ is the non-interacting analog of $\chi$. equation 3.6.18 expresses $U$ as the difference between two total energy second derivatives of equation (3.6.13): the one obtained at self consistency $(-\chi^{-1})$ and the one evaluated at the first iteration of the perturbed run $(-\chi_0^{-1})$, meaning the curvature of the total energy of the non-interacting KS system. The latter term has no relation with electron-electron interactions, so can be removed. From a supplementary perspective, equation (3.6.18) can be seen as the solution of the Dyson equation for $\chi$ and $\chi_0$ , where $U$ acts as the interaction kernel ($\chi = \chi_0 + \chi_0 U \chi$). In practice, one need solve modified KS equations in which atomic potentials are perturbed one at a time in order to determine the variations of atomic occupations which is given by,

$$(H_\sigma + \lambda^J \hat{V}^J_{pert})|\Psi_{\nu k\sigma}\rangle = \varepsilon_{\nu k\sigma}|\Psi_{\nu k\sigma}\rangle \tag{3.6.19}$$

Where, $H_\sigma$, $\Psi_{\nu k\sigma}$, and $\varepsilon_{\nu k\sigma}$ are the Hamiltonian, the KS wave functions, and the KS energies of the perturbed system, respectively. These equations can be evaluated by taking the functional derivatives of equation (3.6.14) with respect to $\Psi^*_{\nu k\sigma}(r)$. Using equation (3.6.10), the perturbing potential is becomes

$$\hat{V}_{pert} = \sum_m \hat{P}^J_{mm'} \tag{3.6.20}$$

which is a sum of the projections on the localized atomic orbitals of the $J^{th}$ atom, and also $\hat{P}_{mm'} = |\psi^I_m\rangle\langle\psi^I_{m'}|$ is the projector. The final results (the effective Hubbard parameters) thus have to be converged with respect to the super cells size. In practice, after solving equation

(3.6.16), the response matrices can be easily computed using finite differences:

$$\chi_{IJ} = \frac{\delta n^I}{\delta \lambda^J} \tag{3.6.21}$$

In this case, the variation in the strength $\lambda^J$ of the perturbing potential should be small, for the response of the system to be in linear but large enough for the response to be significant with respect to numerical noise. As a result, the full response matrix $\chi$ is constructed by perturbing one at a time the crystallographically in equivalent Hubbard manifolds of the individual Hubbard atoms. When one Hubbard atom or manifold is perturbed, the response of all the atoms is recorded, so that one column of the response matrix $\lambda$ is determined. The other matrix elements (in the columns corresponding to equivalent Hubbard atoms) are then reconstructed by symmetry.The dimension of the response matrix $\chi$ is $N_H^{sc} \times N_H^{sc}$ , where $N_H^{sc}$is the number of Hubbard atoms in the super-cell. It also point out that the change in the occupations of the non-Hubbard atoms (not explicitly included in the response matrices) contributes to the screening of the effective interaction.

## 3.7 Self Consistent Calculation with Hubbard Correction

The increased computational efficiency, the higher level of automation, and the user-friendliness promoted by the use of DFPT in the calculation of the Hubbard parameters. This can be exploited to make the calculation fully 'self-consistent' and to obtain Hubbard parameters that are fully consistent with both the electronic structure of the system and,in addition, with the crystal structure. The idea is to recompute the effective $U$ parameters from a $DFT+U$ ground state until the values obtained from the DFPT calculation $U_{out}$ coincide (within a fixed precision $\delta$ ) with those used in determining the ground state that DFPT is based on $U_{in}$ [139],

$$|U_{out} - U_{in}| < \delta, \tag{3.7.1}$$

Now, the convergence of the iterative procedure in most cases is guaranteed by the observed smooth and monotonic dependence of output interaction parameters $U_{out}$ on the input one $U_{in}$.

This iterative procedure yields the final self-consistent values of the Hubbard interactions, labeled $U_{scf}$. The use of LR-cDFT (or DFPT) to recalculate iteratively the Hubbard parameters until self-consistency is straightforward. However, in order to prevent the Hubbard correction from responding to the perturbation thus spuriously contributing to the calculation of the total energy curvature [138], it is important to maintain the Hubbard potential unchanged during the iterative solution of linear-response equations as in [134], as was discussed in section 3.6.

The self-consistent values of $U$ in addition to a given crystal structure, it is also important to obtain consistency of the final Hubbard parameters with the crystal geometry When structural optimization is necessary. Moreover, one can envision an overall iterative procedure, as illustrated by the flowchart diagram in Figure 3.3. The workflow of Figure 3.3 drives the system to a global minimum also with respect to the changes in the Hubbard parameters.The procedure to compute $U_{scf}$ is summarized as follows as follows:

- Set up the initial crystal structure for the system of interest and choose the initial values for U mostly of order of $10^{-8}$.

- Perform a self-consistent field (SCF) ground-state calculation using DFT+U with the current input values of Hubbard parameters $U_{in}$

- Perform a DFPT calculation to determine the new values of the Hubbard parameters ($U_{out}$ ).

- Perform a structural optimization using DFT+U with the current values of U (i.e., $U_{out}$).

- Return to Step 2 with updated values of the Hubbard parameters (i.e., $U_{in} = U_{out}$) and iterate the procedure until the point when the variations of the Hubbard parameters as in Equation (3.6.18) and of the crystal structure are both within fixed thresholds.

## 3.8 Density Functional Perturbation Theory

Density functional theory is effective for ground state density and energy. The Density Functional Perturbation Theory (DFPT) is the application of perturbation theory on the DFT [140].

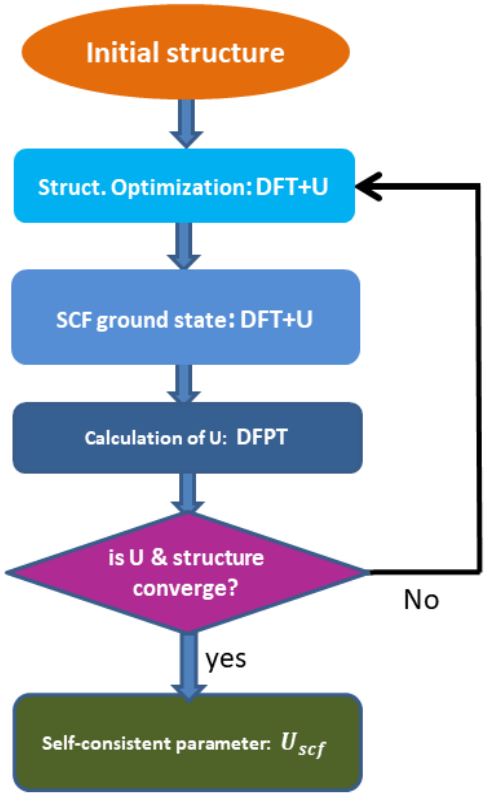


Figure 3.3: The algorithm for the calculation of self-consistent Hubbard parameters $U_{scf}$(onsite)

An accurate way to calculate the energy-derivatives was proposed by X. Gonze [141, 142] which is based on a variational principle involving a minimization procedure rather than solving the Sternheimer equation and giving also access to non-linear responses. Perturbations associated to atomic displacements R, homogeneous strain, and homogeneous electric field E, and summarize them into a single parameter $\lambda$, then the energy functional $E(\lambda)$ can be expanded in a power series of $\lambda$ around the ground state structure $\lambda = 0$. DFPT studies the response of a quantum system under small perturbation at the level of first principle electronic structure theories as that of Kohn-Sham DFT. The most important application of DFPT in this study is to calculate of lattice vibration (phonon), which will be important for further calculations of many physical properties of the crystal structures.

Many interesting response functions are the result of application of an external perturbation to a system. These response functions include the second, third, or higher order derivatives of the total energy with respect to applied perturbation. Some of the important response functions

are

$1^{st}$ order: forces, stress, dipole moment, ...

$2^{nd}$ order: phonon dynamical matrix, elastic constants, dielectric susceptibility, piezoelectricity, internal strain

$3^{rd}$ order: non-linear dielectric susceptibility, phonon-phonon interaction anharmonic elastic constants etc.

Let's take an external potential which depends on certain parameter $\lambda$ as,

$$V_\lambda(r) \simeq V(r) + \lambda \frac{\partial V(r)}{\partial \lambda} + \frac{1}{2}\lambda^2 \frac{\partial^2 V(r)}{\partial \lambda^2} + ... \tag{3.8.1}$$

and expanding the charge density,

$$n_\lambda(r) \simeq n(r) + \lambda \frac{\partial n(r)}{\partial \lambda} + \frac{1}{2}\lambda^2 \frac{\partial^2 n(r)}{\partial \lambda^2} + ..., \tag{3.8.2}$$

in addition, the energy functional with respect to $\lambda$ can be expressed as

$$E_\lambda(r) \simeq E(r) + \lambda \frac{\partial E(r)}{\partial \lambda} + \frac{1}{2}\lambda^2 \frac{\partial^2 E(r)}{\partial \lambda^2} + ... \tag{3.8.3}$$

The first order derivative, which is important for higher order derivatives depends on n(r) is;

$$\frac{\partial E}{\partial \lambda} = \int n(r) \frac{\partial V(r)}{\partial \lambda} dr. \tag{3.8.4}$$

Second order derivative depends on the first derivative of charge density

$$\frac{\partial^2 E}{\partial \lambda^2} = \int \frac{\partial V(r)}{\partial \lambda} \frac{\partial n(r)}{\partial \lambda} dr + \int n(r) \frac{\partial^2 V(r)}{\partial \lambda^2} dr. \tag{3.8.5}$$

Or can be generalized to mixed derivatives as

$$\frac{\partial^2 E}{\partial \lambda_1 \lambda_2} = \int \frac{\partial V(r)}{\partial \lambda_1} \frac{\partial n(r)}{\partial \lambda_2} dr + \int n(r) \frac{\partial^2 V(r)}{\partial \lambda_1 \lambda_2} dr. \tag{3.8.6}$$

Then, linear charge response becomes

$$\frac{\partial n(r)}{\partial \lambda} = 2\sum_i \psi_i^*(r)\frac{\partial \psi_i(r)}{\partial \lambda} \tag{3.8.7}$$

## 3.9 The Bloch Theorem

The use of the crystal lattices spatial periodicity is a requirement for a rational approach to DFT. A unit cell, which is repeated in all spatial directions, is what determines a periodic structure. For any lattice vector **R**, the KS potential is hence periodic and defined by,

$$V_{ks}(R) = V_{ks}(r+R), \tag{3.9.1}$$

A Blochs function is the generalization of a plane wave for an electron in periodic potential. Blochs theorem states that in a periodic solid each electronic wave function can be written as the product of cell-periodic part and wave like part.

$$\Phi_{ik} = e^{i\mathbf{K}.\mathbf{R}}u_{i\mathbf{k}}(r), \tag{3.9.2}$$

with the periodic

$$U_{i\mathbf{k}}(r) = U_{i\mathbf{k}}(r+R), \tag{3.9.3}$$

The energy spectrum is periodic with reference to the reciprocal lattice is an obvious conclusion. That is,

$$E_{i\mathbf{k}}(k) = E_{i\mathbf{k}}(K+G), \tag{3.9.4}$$

for every reciprocal lattice vectors **G**. Therfore, the energy spectrum is fully represented within the Brillouin zone (BZ), the primitive cell of all reciprocal lattices.

## 3.10 Plane wave basis set and Cuttoff energy

A Bloch function is the generalization of a plane wave for an electron in periodic potential. According to Bloch theorem, the wave function can be written as the product of cell-periodic part and wave like part.

$$\phi_k(r) = e^{\vec{i}G.\vec{r}} u_{i\mathbf{k}}(r), \tag{3.10.1}$$

where $u_k(r)$ is periodic in space with the same periodicity as the super cell. That is,

$$u_{ik}(\mathbf{r+R}) = u_{ik}(\mathbf{r}), \tag{3.10.2}$$

The cell-periodic part of the wave function can be expanded using a basis set consisting of a discrete set of plane waves whose wave vectors are reciprocal lattice vectors of the crystal,

$$u_{nk}(\mathbf{r}) = \sum_G c_{ik}(\mathbf{G}) e^{i(\mathbf{G.r})}, \tag{3.10.3}$$

where $c_{i\mathbf{k}}, \mathbf{G}$ are expansion coefficients and the reciprocal lattice vectors. Therefore each electronic wave function can be written as a sum of plane waves,

$$\phi_{ik}(\mathbf{r}) = \sum_G c_{i\mathbf{k}}(\mathbf{G}) e^{i(\mathbf{K+G}).\mathbf{r}}, \tag{3.10.4}$$

The electronic wave functions at each k-point can be expressed in terms of a discrete plane wave basis set. In practice we can not work with an infinite basis set, it has to be truncated to allowable precision. The number of plane waves can be restricted by placing an upper boundary to the kinetic energy of the plane waves. This boundary is called energy cut-off $(E_{cut})$ [143]. The kinetic energy is related to plane waves in this expansion by $(\mathbf{k+G})^2/2$. The summation over $\mathbf{G}$ is infinite and thus for practical reasons an upper boundary, the cutoff energy $E_{cut}$ should be set so that $(\mathbf{k+G})^2/2 < E_{cut}$ . The cutoff energy can be viewed of as a "resolution" details in the wave function smaller than $2\pi/\mathbf{G}_{max}$ are neglected. It results in the second important advantage of the plane wave basis set, namely, the accuracy can be improved systematically by increasing $E_{cut}$.

## 3.11 K-point grid: Integration Over the First Brillouin Zone

Density functional theory uses electron density as a source of information for all quantities. The electron density used in DFT is given by,

$$n(r) = \int_{BZ} d\mathbf{k} \sum_{i=1}^{N_k} f_{i\mathbf{k}} |u_{i\mathbf{k}}(r)|^2, \tag{3.11.1}$$

where the sum runs over all bands at point $\mathbf{k}$, $N_\mathbf{k}$ and $f_{i\mathbf{k}}$ are the occupancy of the band, either "1" below the Fermi level or "0", otherwise. It is desirable to substitute out the step function for a smooth function in order to hasten the integration's convergence with regard to the number k-points. Since it imitates the impact of temperature, this strategy is known as a finite-temperature approach, also known as smearing [123]. This smearing is typically described by Gaussian functions.

From an infinitely extended real space lattice, k is continuous variable, constrained to the first BZ owing to periodicity. In numerical calculations, integration over a continuous variables is not attainable. Therefore, a k-point grid is constructed to sample the first BZ, Commonly, a Monkhorst-Pack grid, an equally spaced grid, is selected [144]. Additionally, sampling of the irreducible BZ (IBZ), the reduction of the first BZ by the lattice symmetries, is sufficient for calculation of the density. The normalized weight $w_k$ has to be included, to take into account the multiplicity of each k-point. Consequently, the electron density can be expressed as,

$$n(r) = \sum_{k \in IBZ} w_k \sum_{i=1}^{N_k} f_{i\mathbf{k}} |u_{i\mathbf{k}}(\mathbf{r})|^2, \tag{3.11.2}$$

## 3.12 Plane wave approximations and Pseudopotentials

For electronic structure calculations of periodic systems, the most widely used approach is to employ a plane wave basis to represent the orbitals, the electron density, and other quantities in terms of Fourier expansions. According to Bloch theorem, the Kohn-Sham orbitals of a system with periodic external potential can be written as a product of a cell-periodic part and a

wave-like part with periodicity of the underlying lattice.

$$\psi_{nk}(r) = e^{i\mathbf{k}.\mathbf{r}} u_{nk}(r), \tag{3.12.1}$$

where $\mathbf{k}$ is a Brillouin zone (BZ) sample or k-point. Taking into account its periodicity, the wave-like part is expanded as a set of plane waves. And

$$u_{nk}(r) = \frac{1}{\sqrt{\Omega}} \sum_j c_{jnk} e^{i\mathbf{g}_j.\mathbf{r}}, \tag{3.12.2}$$

where $\mathbf{g}_j$ are vectors of the reciprocal lattice, and $\Omega$ is the unit cell volume. The number of basis functions is controlled by the energy cut-off $E_{cut}$. Only expansion coefficients $c_{jnk}$ related to plane waves with a kinetic energy $\frac{1}{2}|k+g_j|^2 < E_{cut}$ are retained. This allows easy and systematic control of the quality of a plane wave basis set.

Plane wave basis sets are usually used in combination with Pseudo-potentials (PP) [145, 146] such that the plane waves have to describe only the valence orbitals and valence electron density. Expanding core orbitals and the features of other orbitals close to the atomic nuclei would otherwise require a very large number of plane waves of large energy cut-off.

The pseudo-potential method is based on the fact that the spectrum of intrinsic states does not specify a well-defined potential, so that one may find a weak potential (pseudo-potential) such that its spectrum coincides with the spectrum of the actual potential. The real and the pseudo wave-function and potentials match above a certain cut-off radius $r_c$ (Figure-3.4). This method involves orthogonalization of the wave functions of valence electrons $\psi_v$ with respect to wave functions of the electrons of the ion core $\psi_c$. Modern pseudo-potentials come in three varieties, norm-conserving pseudopotentials (NCPP) [147], ultra-soft pseudo-potentials (USPP) [145, 148], and projector-augmented wave (PAW) [146]. The NCPPs their construction ensures that they reproduce the logarithmic derivatives, i.e., the scattering properties, of the true potential in a wide range of energies. USPPs significantly reduce the grid resolution necessary to converge the electron density which generalizes the eigen-problem and adds charge density dependence to the non-local potential. All pseudopotential libraries are tested based on the

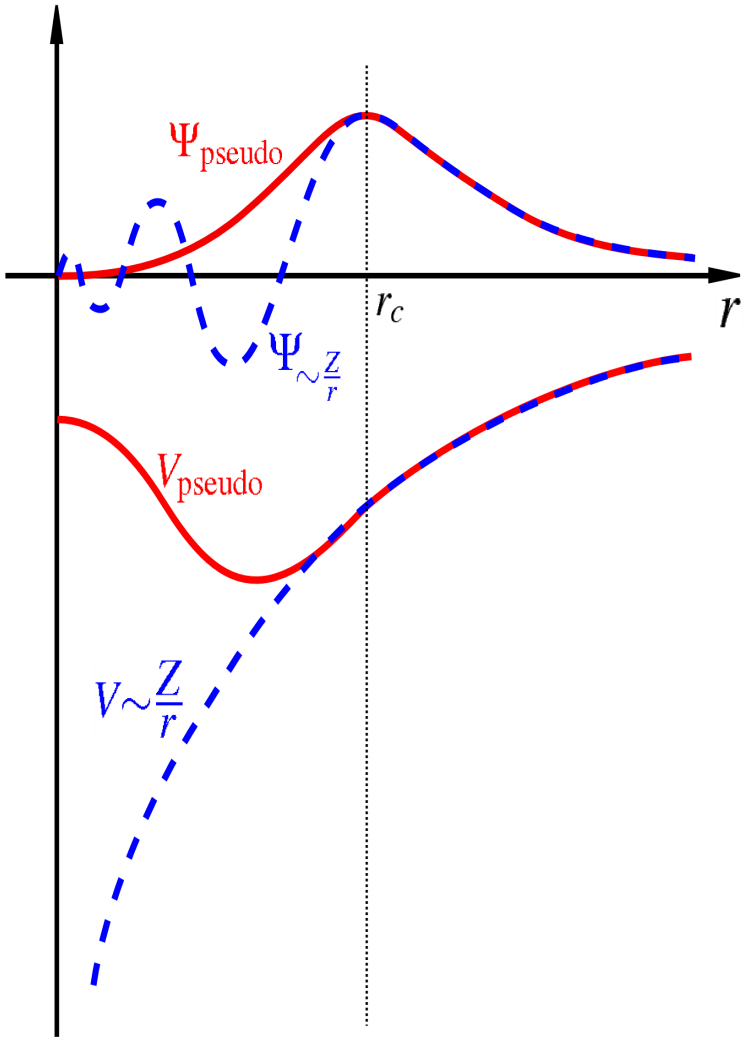


Figure 3.4: Comparison of a wave-function in the Coulomb potential of the nucleus to the one in the pseudo-potential.

generalized gradient approximation (GGA) for the exchange correlation functional of Perdew, Burke and Ernzerhof (PBE) [130]. The choice of pseudo-potential type mainly depends on two factors, the transferability and softness, in DFT calculation. Currently, modified standard solid-state pseudopotential (SSSP) libraries are also available. The libraries are prepared by testing all type of pseudopotentials and selecting a PP which performs best for a specific material [149].

## 3.13 Quantum-Espresso Software Package

Quantum espresso (QE) is an integrated suite of computer codes for electronic structure calculations and materials modeling based on density functional theory, plane wave basis set and pseudopotentials to represent electron-ion interactions. It is free software distributed under the terms of the GNU(Gnu's Not Unix) General Public License (GPL) [150]. Quantum-ESPRESSO stands for Quantum open-Source Package for Research in Electronic Structure, Simulation, and Optimization. The codes are constructed around the use of periodic boundary conditions, which allows for a straight forward treatment of infinite crystalline systems. The full Quantum ESPRESSO distribution contains the core packages, such as PWscf, PHonon, etc for the calculation of electronic-structure properties within Density Functional Theory (DFT), using a Plane-Wave basis set and pseudopotentials [150]. In considering DFT for many body problems, we are dealing with solving a many body system problems. Now adays DFT is consequently quantitatively applied in numerous soft ware programs, such as ABINIT, Gaussian, Quantum ESPRESSO, SIESTA, VASP, WIEN2k, and others. These differ in a number of respects, including the basis function choices, the pseudo-potentials, and the diagonalization procedures for the KS Hamiltonian. The advantage is that Quantum ESPRESSO is a collection of packages as opposed to a single, tightly integrated monolithic package. website: https://w.w.w quantum-espresso.org/.

## 3.14 Computational Details

Single layer of $WX_2$ a P63/mmc space group symmetry with the W atoms having a trigonal prismatic coordination with the chalcogen atoms, is taken into consideration. In this study we have used density functional theory (DFT) with the implementation of quantum espresso package (QE), applying the generalized gradient approximation (GGA) with the Perdew-Burke-Ernzerhof (PBE) functional and GGA + U approximations for the electron exchange-correlation interactions. The corresponding valence electrons of the elements considered for this work, W = [Xe]$4f^{14}5d^{4}6s^{2}$, Mn = [Ar]$3d^{5}4s^{2}$ and for the chalcogens S = [Ne] $3s^{2}3p^{4}$, Se = [Ar] $3d^{10}4s^{2}4p^{4}$ and Te = [Kr]$4d^{10}5s^{2}5p^{4}$ were used. The structure of monolayers of $WX_2$ are re-

laxed and optimized using the plane wave of cut-off energy of 55 Ry and the Brillouin zone (BZ) with a 661 Monkhorst-Pack grid in accord with the convergence criteria (energy $10^{-5}$ Ry), (force $10^{-4}$ Ry/Bohr). Under these conditions, the lattice parameters a=b and the vacuum space, normal to the plane of the layer was 15$\mathring{A}$ used for monolayers this work. Spin-polarized first-principles calculation was also employed to analyze the electronic and magnetic properties of 2D-$WSe_2$ doped with manganese. In case of $WS_2$/$WSe_2$ heterobilayer we used the minimum energy principle to calculate the interlayer spacing between $WS_2$ and $WSe_2$ monolayers. The ultrasoft pseudopotentials (USPs) and norm conserving pseudopotentials (NCPs) were used to treat the interaction of electrons with ion cores.

# Chapter 4

# Result and Discussions

## 4.1 Structural, electronic, dynamic, and optical properties of monolayer $WTe_2$ under small biaxial strain

### 4.1.1 Introduction

In this study, we have investigated the structural, electronic, vibrational, and optical properties of 2H-$WTe_2$, (space group p63/mmc) for low dimensional electronic and optical applications. The structural and electronic properties are investigated using the GGA and GGA + U approximations for exchange-correlation potential. Moreover, the effect of tensile or compressive strain on the electronic structure of $WTe_2$ is determined. The phonon dispersion is calculated using density functional perturbation theory (DFPT) and density functional perturbation theory with Hubbard correction (DFPT + U). The optical properties are determined using time-dependent density functional theory (TD-DFT). Finally, the obtained results are compared with the existing experimental and theoretical results.

Tensile and compressive straining circumstances were taken into consideration to the monolayer following optimization of the equilibrium lattice parameters. The structural, electronic, lattice vibration, and optical properties were computed under both stressed and unstrained circumstances. Biaxial strain is applied to the monolayer from 2% tension to 2% compression to analyze the electronic property, lattice vibration, and dielectric function. The effective Hubbard

Table 4.1: The calculated effective Hubbard parameter for $WTe_2$ for 2% biaxial compressive strain, equilibrium (no strain), and 2% bi-axial tensile-strain.

| Type of strain | W(d)$U_{eff}$(eV) |
|---|---|
| 2% compression | 3.036 |
| Unstrained | 3.045 |
| 2% tension | 3.053 |

parameter ($U_{eff}$) was calculated iteratively for W-d orbitals using a linear response formalism utilizing DFPT with an ortho-atomic projection method [139, 151] and the values for Hubbard correction are shown in Table 4.1.

### 4.1.2 Structural properties of Monolayer $WTe_2$

The crystal structure of two dimensional 2H-$WTe_2$ is indicated in Figure 4.1. Two dimensional $WTe_2$ is a family of TMDs of hexagonal lattice with W atom is sandwiched in two Te atoms in each individual single layer of its lattice structure. The lattice constants, a=b, have been calculated with GGA and GGA+U approximations leaving the vacuum gap of 15$\mathring{A}$ normal to the plane of the next layer. And the lattice constants are compared as indicated in Table-4.2 with previously calculated reference values and our computed values are in good agreement with the references. The structural parameters have been computed for important parameters to

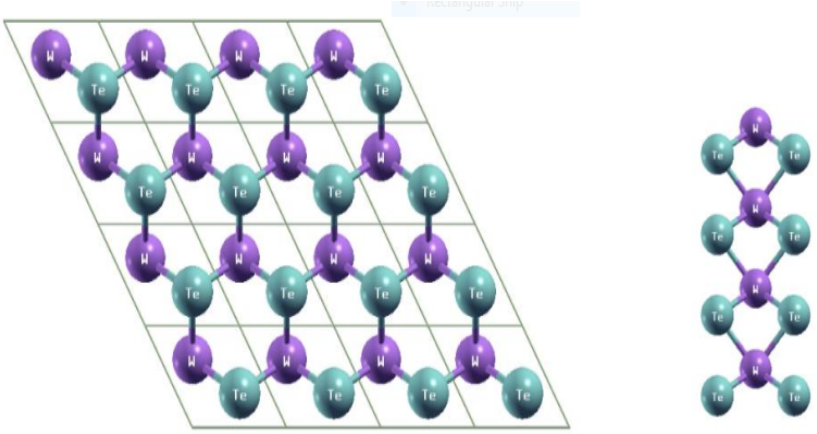

Figure 4.1: Structure of $WTe_2$ monolayer with the transition metal sandwiched between the chalcogen atoms

check the structural stability of $WTe_2$ monolayer. The computed structural parameters for the layer are in a good agreement with the Birch Murnaghan equation of state (EOS) [152] given

Table 4.2: Calculated values for structural parameters of $WTe_2$ monolayer in reference with other previous results

| Methods | Lattice parameter ($\AA$) | $V_0(\AA)^3$ | B(Gpa) | B' |
|---|---|---|---|---|
| GGA | 3.565 | 654.98 | 49.7 | 3.91 |
| GGA+U | 3.539 | 641.45 | 49.9 | 4.55 |
| Theoretical | 3.57 [6], 3.59 [7], 3.55 [23, 24] | - | - | - |
| Experimental | - | - | - | - |

by

$$E(v) = E_0 + \frac{B_0 V}{B' - 1}\left[\frac{\left(\frac{v_0}{v}\right)^{B'_0}}{B' - 1} + 1\right] - \frac{B_0 V}{B' - 1} \tag{4.1.1}$$

Where $E_0$ is for minimum energy, $V_0$-volume of the unit cell, $B_0$ -bulk modulus and $B'_0$-derivative of the bulk modulus. The calculated volume versus energy and volume versus pressure diagrams are indicated for $WTe_2$ monolayer of $2 \times 2 \times 1$ supercell is described in Figure 4.2. Moreover, the obtained results are indicated in Table 4.2.

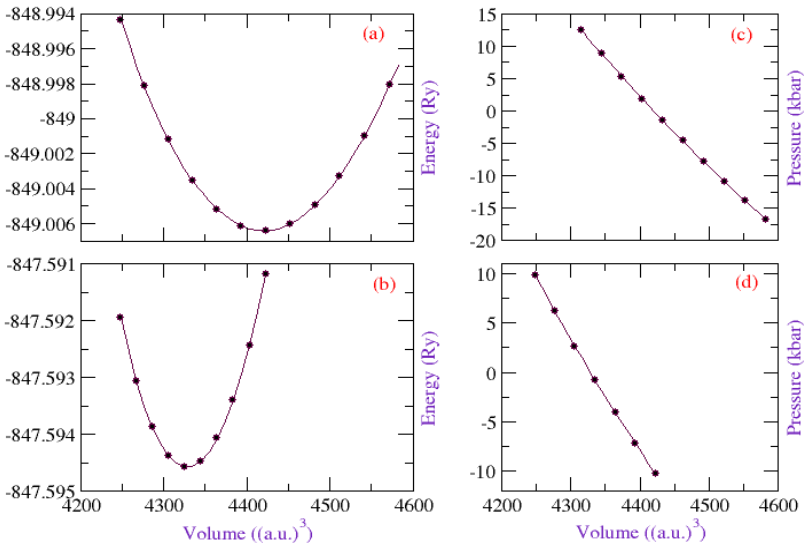


Figure 4.2: Volume versus energy diagram of 2H-$WTe_2$ using (a) GGA (b), GGA+U and pressure versus volume diagram using (c) GGA and (d) GGA+U

The response of monolayer $WTe_2$ on external stresses in lower limit results in elongation of bond length of W-Te from 2.747 $\AA$ in equilibrium to 2.802 $\AA$ in 2% tensile strain and shortening of the bond length to 2.692 $\AA$ in 2% compressive strain. However, the is no change in the bond angle of the monolayer because of 2% strain compressive or tensile strain.

### 4.1.3 Electronic Properties of Monolayer $WTe_2$

Different methods have been applied when analyzing the electronic properties of the system including the Hubbard model. The band structure of monolayer $WTe_2$ is shown in Figure 4.3(a-c) and it has a direct band gap. When the system is imposed to small strain (0-2%) both in tension and compression, the band gap of the system increases with biaxial compression and decreases with biaxial tensile strain.

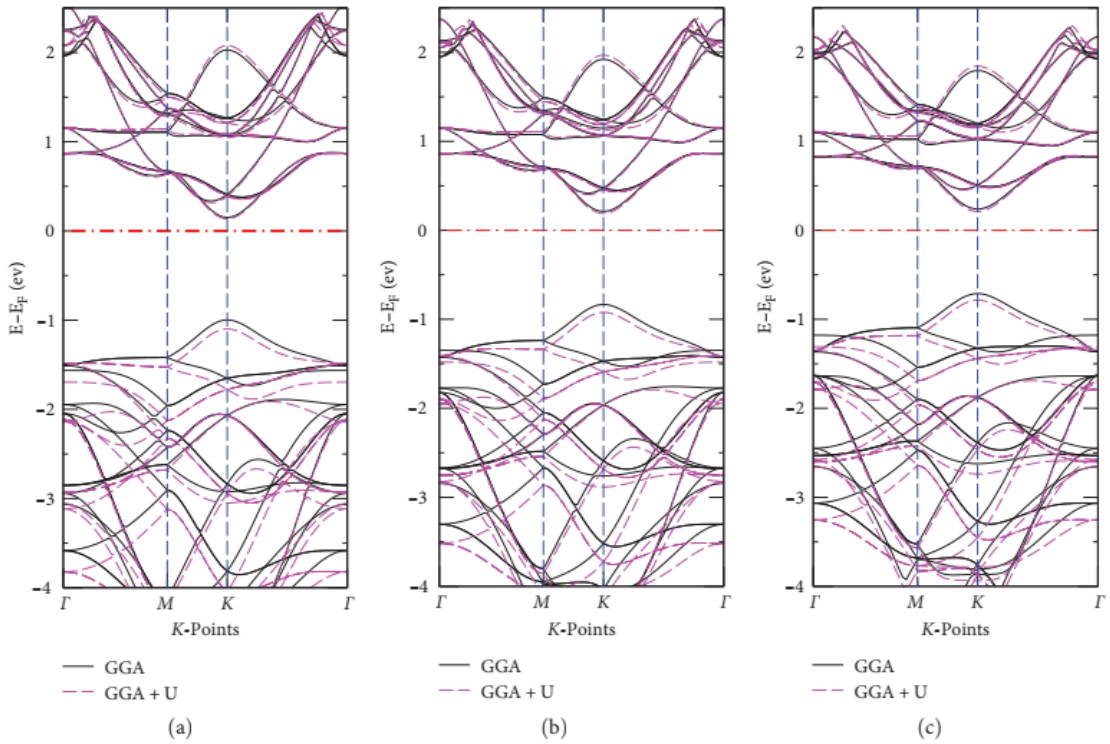


Figure 4.3: Band structure of 2D-$WTe_2$ (a) 2% biaxial compression, (b) unstrained, and (c) 2% biaxial tensile strain using GGA and GGA + U

The band structure of monolayer 2D $WTe_2$ using GGA and GGA+U approximations for exchange correlation potentials has been indicted in Figure 4.3 with the black (solid) line and magenta (broken) line respectively. The band gap values obtained for 2% biaxial compression of the system are 1.1487 eV (GGA) and 1.2332 eV (GGA +U) respectively as shown in Figure 4.3(a). For unstrained condition, the band gap values are 1.0439 eV (GGA) and 1.1089 eV (GGA +U) as described in Figure 4.3(b). In case of 2% biaxial tensile strain the band gap values are 0.9439eV (GGA) and 0.9945 eV (GGA+U) as demonstrated in Figure 4.3(c). We determined some basic and important properties of the 2D-$WTe_2$ from these computations. The direct band gap cannot be altered by small strain and this may result in materials to be

Table 4.3: The band gap values (eV) of monolayer 2H $WTe_2$ calculeted in GGA(PBE) approximation and GGA+U (Hubbard model)

| Type of strain | GGA | GGA+U | Theoretical | Experimental |
|---|---|---|---|---|
| unstrained (0%) | 1.0439 | 1.1089 | 0.974 (GGA) [7]<br>0.75 (GGA) [24] | |
| 2% biaxial compression | 1.1487 | 1.2332 | - | - |
| 2% biaxial tension | 0.9439 | 0.9945 | - | - |

preferable for some electronic and optical properties. Moreover, the effect of electron-electron interaction in the band diagram is noticeable with the same manner in both strained and unstrained conditions and hence the Hubbard correction is significant for the system. The range of band gap values of the monolayer 2D 2H $WTe_2$ both in an unstrained and strained conditions are interesting for photovoltaic applications. The calculated values in this work is and other previous works are compared as shown in Table 4.3 and the results are in good agreement with the previous works.

In addition to the band structure, the total density of states (TDOS) and partial density of states (PDOS) were calculated for 2% biaxial compression, unstrained and 2% biaxial tensile strain using GGA and GGA+U approximation for exchange correlation potentials as shown in Figure 4.4 - (a-c) and Figure 4.5 - (a) and (b) respectively. The gap from the valence band maximum to the conduction band minimum decreases when the system is imposed to biaxial tensile strain and increases for biaxial compression. The partial density of states (PDOS) result describes that for the low-lying states, the W(3d) orbitals contributed most to the maximum valence band and minimum conduction band. In first principles calculations using DFT of the GGA approximation, monolayer 2H-WTe2 under biaxial compression exhibits an expanded energy band resulting in blue shift. In the case of biaxial tension, red shift happens by narrowing of the energy band gap in comparison to the equilibrium. The GGA+U approximation, when used under small strain, modifies the band gap without changing the VBM and CBM, making 2D-$WTe_2$ a viable material for electronic and optical applications.

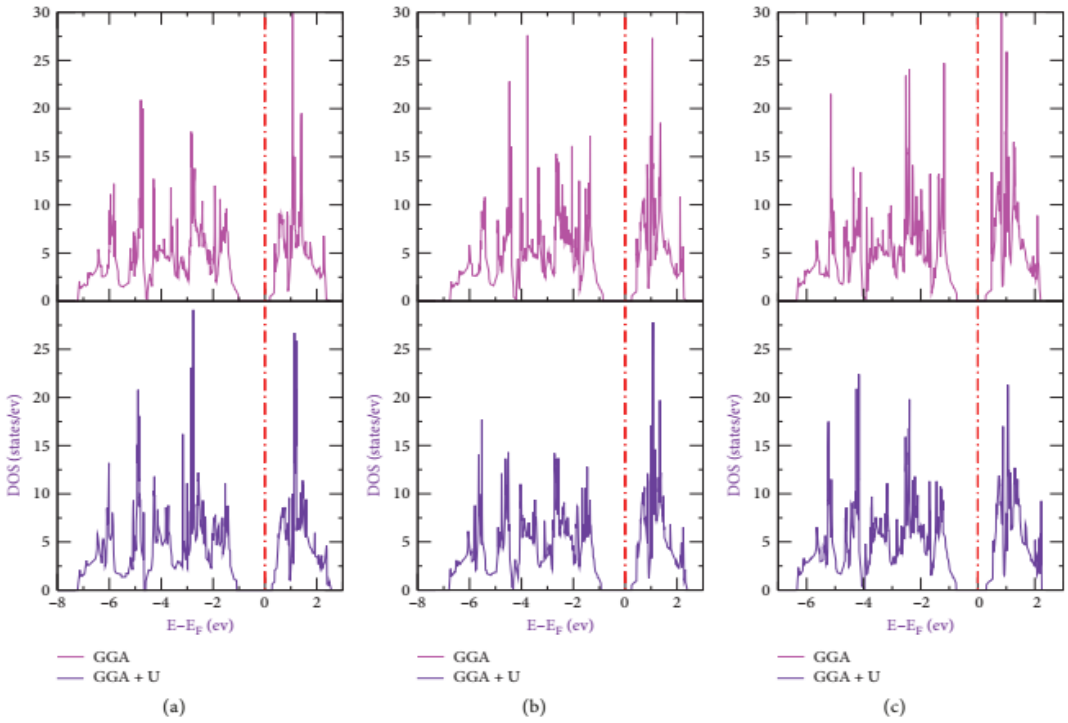


Figure 4.4: The density of states of monolayer $WTe_2$ (a) with 2% biaxial compression, (b) with no strain, (c) with 2% biaxial tension

### 4.1.4 Lattice vibration of Monolayer $WTe_2$

Concerning the lattice vibration, it is important to know the dynamic property of the material for its stability. We have calculated the phonons dispersion for 2% biaxial compression, unstrained and 2% biaxial tensile stress in accord with DFPT and DFPT+ U for exchange-correlation potential respectively as shown in Figure 4.6 - (a-c). The obtained result for DFPT shows that the unstrained condition is dynamically stable and has no an imaginary part as shown in Figure 4.6 - (b). However, when the monolayer of 2H - $WTe_2$ is subjected to biaxial strain the dispersion relation has negative frequency and it is dynamically unstable with respect to DFPT as described in Figure 4.6 - (a) and 4.6 - (c) respectively. However, the phonon dispersions obtained for biaxal compression, unstrained and biaxial tensile stresses using the Hubbard correction (DFPT +U) are dynamically stable as described in Figure 4.6 (magenta or broken lines). That is DFPT + U is used to capture the effect of electronic localization of vibrational frequencies and give full access to all quantities requiring well converged sums over the entire vibration spectrum.

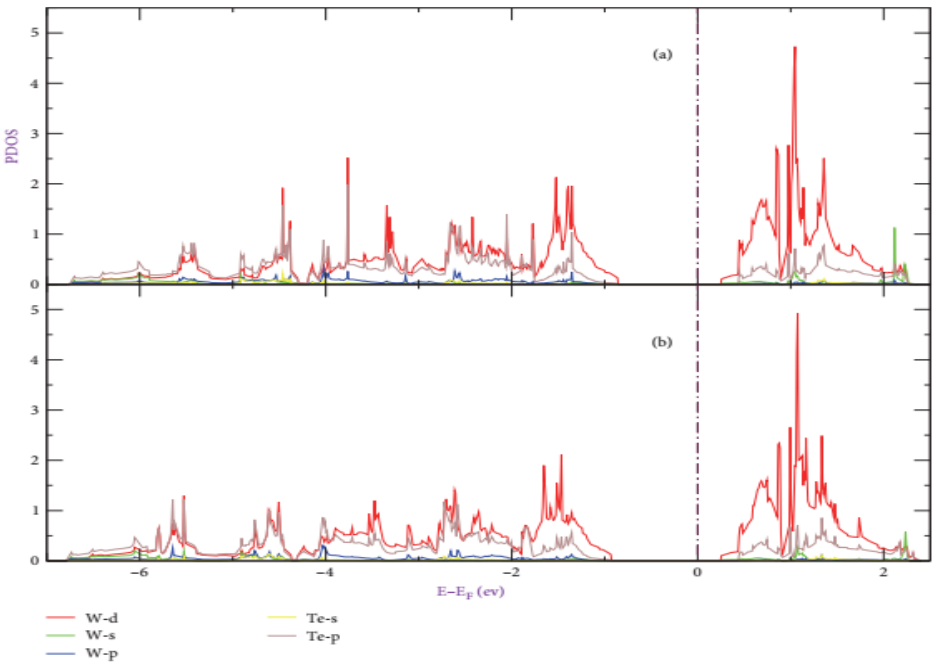


Figure 4.5: Partial density of states for unstrained monolayer of $WTe_2$ (a) using GGA approximation and (b) GGA+U approximation

### 4.1.5 Optical properties Monolayer $WTe_2$

To calculate the optical properties, the complex dielectric function $\varepsilon(\omega)$ within an independent particle formalism is used [153] in terms of the real $\varepsilon_1$ and imaginary parts as;

$$\varepsilon(\omega) = \varepsilon_1(\omega) + i\varepsilon_2(\omega) \tag{4.1.2}$$

The imaginary part $\varepsilon_2(\omega)$ is determined from the momentum dipole transition matrix elements between the valence band and the conduction band electronic states with long wave length approximations [154],

$$\varepsilon_2^{ij}(\omega) = \frac{4\pi e^2}{Vm\omega^2} \sum_{knn'\omega} \langle \chi_{n\sigma}|U_\alpha|\chi_{n'\sigma}\rangle\langle \chi_{n'\sigma}|U_\beta|\chi_{n\sigma}\rangle \times f_{kn}(1-f_{kn'})\sigma(\varepsilon_{kn'} - \varepsilon_{kn} - \hbar\omega) \tag{4.1.3}$$

where, $|\chi_{n'\sigma}\rangle$ are the electron states. The dispersion of the real part of the dielectric function

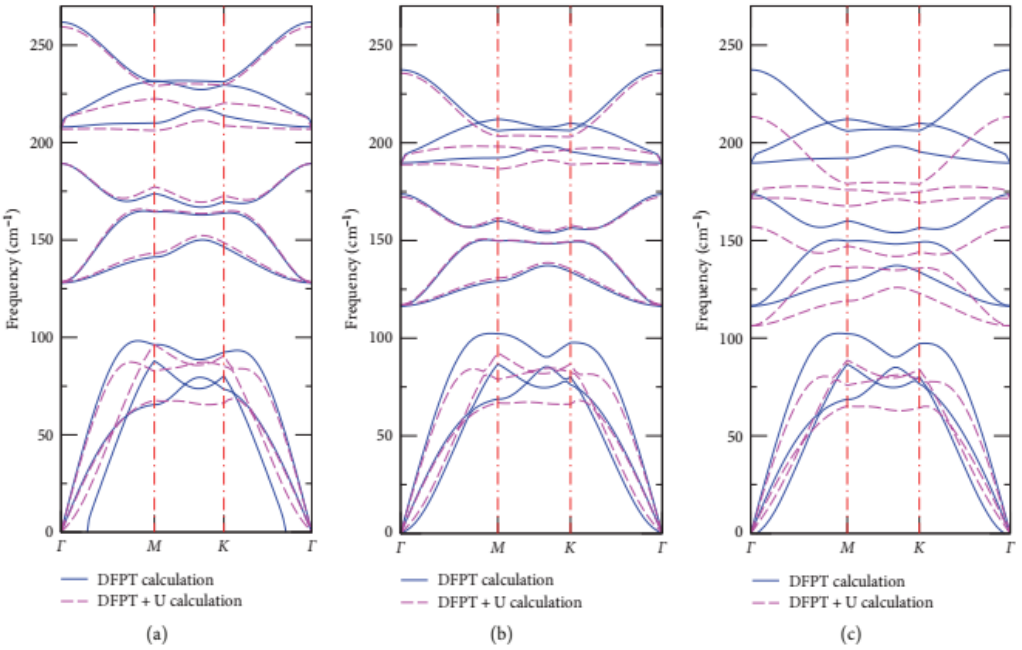


Figure 4.6: Monolayer $WTe_2$ phonon dispersion (a) for compressed, (b) undisturbed (c) stretched in GGA and GGA+U approximation

$\varepsilon_1$ was determined using the imaginary part by Kramers-Kronig relations [155],

$$\varepsilon_1(\omega) = 1 + \frac{2}{\pi} p \int_0^{\infty} \frac{\omega \varepsilon_2(\omega')}{\omega'^2 - \omega^2} d\omega' \tag{4.1.4}$$

Where the symbol P represents the principal value of the integral. The complex index of refraction is written as,

$$N(\omega) = n(\omega) + ik(\omega) \tag{4.1.5}$$

Here, $n(\omega)$ is refractive index and $k(\omega)$ is extinction coefficient that can be evaluated from complex dielectric function. The refractive index $n(\omega)$, the reflectivity ($R(\omega)$), absorption coefficient ($\alpha(\omega)$) and energy loss function ($L(\omega)$) can be determined from dielectric functions by,

$$n(\omega) = \sqrt{\frac{\sqrt{\varepsilon_1^2(\omega) + \varepsilon_2^2(\omega)} + \varepsilon_1(\omega)}{2}}, \tag{4.1.6}$$

$$k(\omega) = \sqrt{\frac{\sqrt{\varepsilon_1^2(\omega) + \varepsilon_2^2(\omega)} - \varepsilon_1(\omega)}{2}}, \tag{4.1.7}$$

$$\alpha(\omega) = \frac{\sqrt{2}\omega}{c}\sqrt{\sqrt{\varepsilon_1^2(\omega)+\varepsilon_2^2(\omega)}-\varepsilon_1(\omega)}, \tag{4.1.8}$$

$$R(\omega) = \frac{(n(\omega)-1)^2+k(\omega)^2}{(n(\omega)+1)^2+k(\omega)^2}, \tag{4.1.9}$$

and

$$L(\omega) = -\Im\frac{1}{\varepsilon(\omega)} = \frac{\varepsilon_2(\omega)}{\varepsilon_1^2(\omega)+\varepsilon_2^2(\omega)}. \tag{4.1.10}$$

The optical properties including dielectric function, optical absorption and energy loss function, reflectivity, and the refractive index are investigated in parallel and perpendicular direction to the plane of the monolayer 2H-$WTe_2$ in the photon energy range from 0 to 10 eV, and the details of the calculations are presented. The real part of the dielectric function $(\varepsilon_1(\omega))$ when the monolayer of 2H-$WTe_2$ is exposed to the polarization parallel and perpendicular direction to the monolayer plane is shown in Figure 4.7 - (a) and 4.7 - (b) respectively. From the result it is possible to deduce that the static dielectric function values for near zero energy $(\varepsilon_1(0))$ is 7.4 (unstrained), 7.7 (biaxial tensile stress) and 7.2 (biaxial compression) arb. unit for the polarization parallel to the plane of monolayer. However, the static dielectric constant $(\varepsilon_1(0))$ decreases when the polarization is perpendicular to the plane of monolayer and the values are 1.85 (unstrained) and 1.84 for 2% biaxial compressive strain and 1.81 for biaxial tensile strain. The magnitude of the real part of the dielectric function for the polarization parallel to the plane is magnified as compared to the perpendicular direction. The peak of the real part of the dielectric constant is 11.77 at 1.77 eV for biaxial tensile strain, 12.10 at 1.9 eV for unstrained and 12.8 at 2.0 eV for biaxial compression (parallel to the plane) and 5.17 at 4.17 eV for biaxial tensile strain, 5.37 at 4.44 eV for unstrained and 5.21 at 4.68 eV for biaxial compression (perpendicular to the plane). Moreover, the peak of linear dielectric function for the polarization perpendicular to the plane of monolayer shifts toward high energy for all cases. The biaxial compression and tensile strain also reduce the magnitude of the real part of the dielectric function as compared to the unstrained one. On the other hand, the imaginary part of the dielectric function is described in Figure 4.7 - (c) for the polarization parallel to the plane and Figure 4.7 - (d) perpendicular to the plane with respect to the incoming photon. The

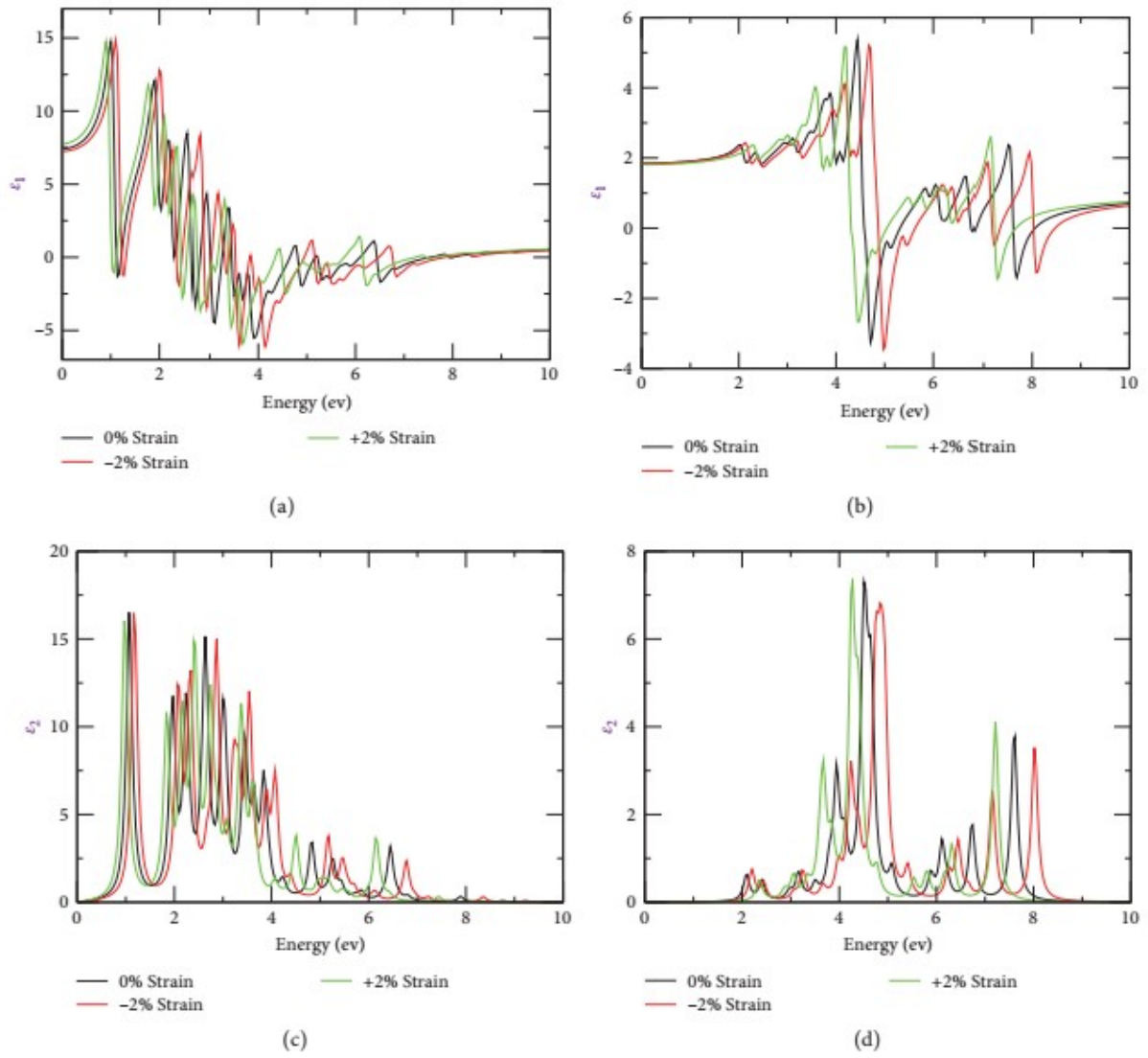


Figure 4.7: The real and imaginary part of the dielectric function versus photon energy (a, and c) with polarization parallel to the plane (b, and d) perpendicular to the plane respectively for the monolayer of 2H-$WTe_2$

imaginary part of the dielectric function has a peak value 16.02 at 0.97 eV for biaxial tensile strain, 16.5 at 1.06 eV for unstrained and 16.48 at 1.17 eV for biaxial compression respectively when the polarization is parallel to the plane of monolayer. The peak value is 7.36 at 4.27 eV for biaxial tensile strain, 7.14 at 4.54 eV for unstrained and 6.81 at 4.84 eV for biaxial compression when the polarization is perpendicular to the plane of monolayer. The magnitude of the imaginary part of the dielectric function is quenched as the monolayer of 2H-$WTe_2$ forced to tensile stress or compression. The negative value in the$(\varepsilon_1(\omega))$ spectra at 4.5, 4.8, and 5 eV corresponds to the peak in the reflectivity spectra. The other important parameters of optical

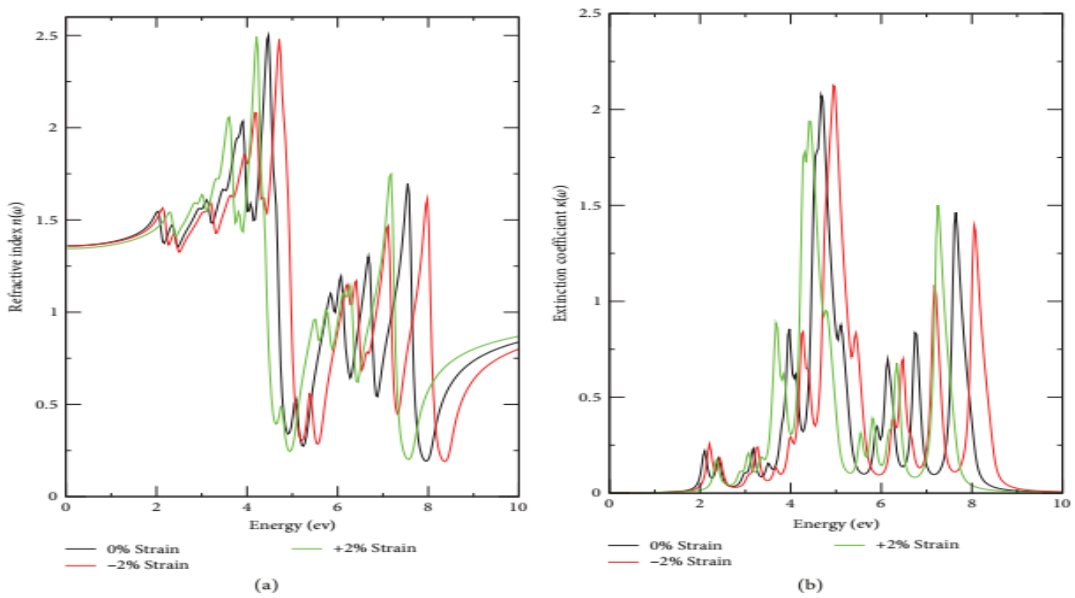


Figure 4.8: (a) Refractive index (b) extinction coefficient with different strain conditions to the plane of 2D - $WTe_2$ layer.

properties are the refractive index $n(\omega)$ and extinction coefficient $\kappa(\omega)$ as shown in Figure 4.8 - (a) and 4.8 - (b) for polarization perpendicular to the plane of monolayer respectively. The value of static refractive index $n(\omega)$ is 1.36 for the case equilibrium and biaxial compression and 1.34 for biaxial tensile stress. The peak values of the refractive index are 2.5 at 4.2 eV for tensile strain, 2.5 at 4.47 eV for unstrained, and 2.48 at 4.7 eV for biaxial compression. The magnitude of the refractive index is nearly the same when the monolayer of 2H - $WTe_2$ is imposed to small tensile or compressive strain. Moreover, the peak of the refractive index shifts toward higher energy when the monolayer of 2H - $WTe_2$ is imposed to biaxial compression than tensile strain. The peak value of the extinction coefficient is 1.94 at 4.4 eV for tensile strain, 2.07 at 4.67 eV for unstrained and 2.13 at 4.94 eV for biaxial compression. The peak value of the extinction coefficient for monolayer of $WTe_2$ shows blue shift in biaxial compression as compared to the tensile stress.

The absorption coefficient of monolayer 2H-$WTe_2$ for unstrained, biaxial compression, and biaxial tensile strain is also described in Figure 9 (a), (b) and (c) respectively. The peaks of the absorption coefficients are $1.3510^6 cm^{-1}$ at poton energy of 8.0473 eV (2% biaxial compression), $1.1310^6 cm^{-1}$ at 7.6467 eV (unstrained) and $1.1010^6 cm^{-1}$ at 7.25 eV (2% biaxial tension). The magnitude of the absorption coefficient of the monolayer of 2H - $WTe_2$ has a

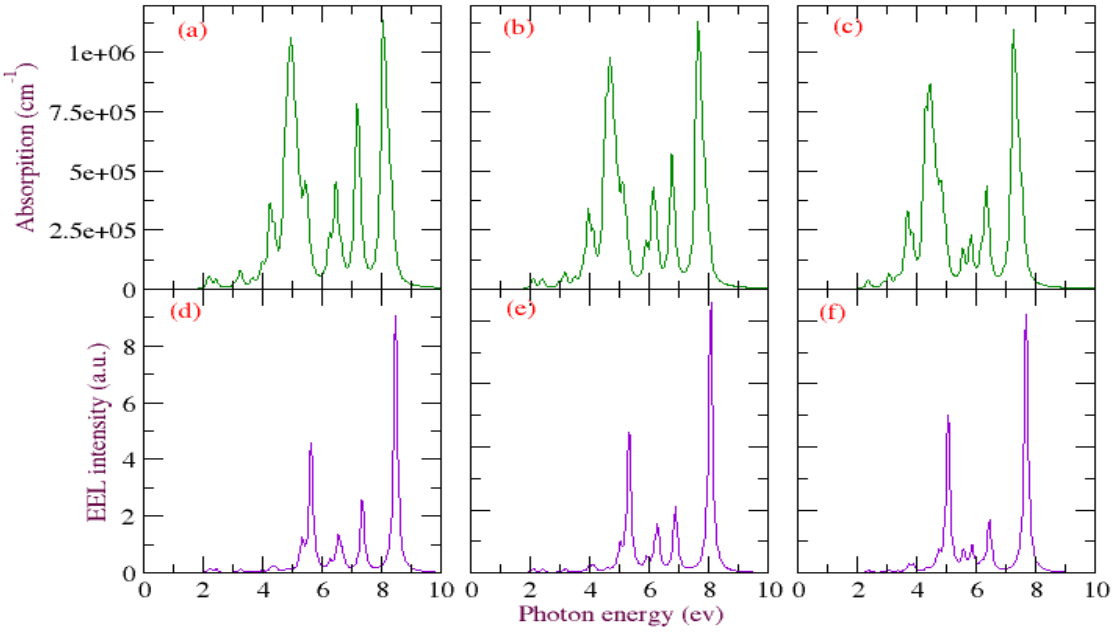


Figure 4.9: Absorption coefficient and electron energy loss function of the monolayer 2H - $WTe_2$ with (a and d) no strain (b and e) -2% strain and (c and f) +2% strain respectively.

little variation in three cases. However, red shift is observed when the monolayer is imposed to biaxial tension as compared to biaxial compression. The large value of absorption coefficient in 2H-$WTe_2$ monolayer coupled with its optimum bandgap enables it for application of solar cell with high power conversion efficiency.

The electron energy loss function of monolayer $WTe_2$ for unstrained, biaxial compression, and biaxial tensile strain is described in Figure 4.9 - (d), (e) and (f) respectively. The energy loss function (EELS) which shows the energy loss of fast electron moving across the medium is a complicated mixture of inter-band transition and plasmon. The electron energy loss spectra are related to the plasma frequency. Peaks in the measured spectra can thus derive zeros of $\varepsilon_1(\omega)$ (when $\varepsilon_2(\omega)$ is not too large), which correspond to collective plasmon excitations, or from structures $\varepsilon_2(\omega)$ which are due to valence-conduction inter-band transitions. The electron energy loss function for a polarization perpendicular to the plane of monolayer has a peak 8.5756 at 8.0807 eV (unstrained), 9.0381 at 8.4814 eV (biaxial compression) and 8.2058 at 7.6801 eV (biaxial strain). Finally, the reflectivity is computed for unstrained (a), biaxial compression (b) and biaxial stress (c) as shown in Figure 10 for polarization perpendicular to the plane of monolayer 2H - $WTe_2$. The value of static reflectivity R(0) are 2.30%, 2.32% and

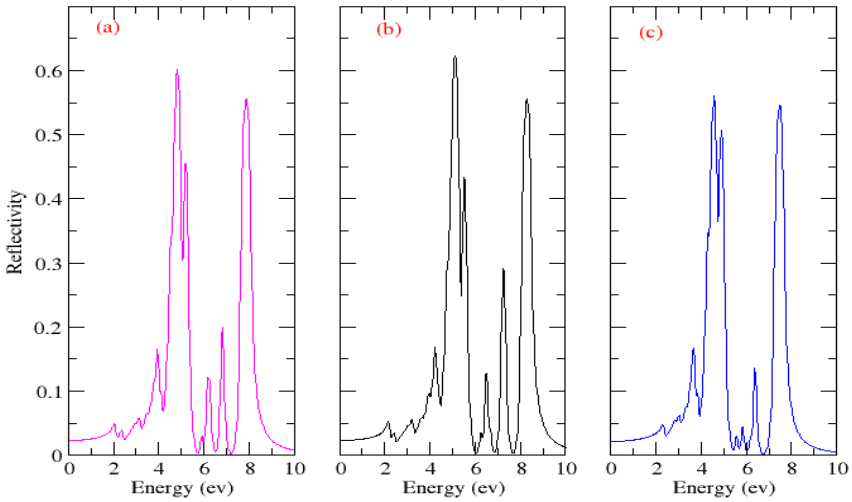


Figure 4.10: Reflectivity of $WTe_2$ monolayer for (a) unstrained (b) -2% strained (c) +2% strained

2.16% for biaxial compression, unstrained and biaxial tension respectively. The peak values of optical reflectivity are 62.3% at 5.1 eV (biaxial compression), 60.2% at 4.8 eV (unstrained), and 56% at 4.575 eV (biaxial tension).

## 4.2 Effects of Mn-doping on the structural, electronic, magnetic and optical properties of $WSe_2$ monolayer

### 4.2.1 Introduction

In this study, Mn-doped monolayer $WSe_2$ is subjected to first-principles calculations utilizing GGA and GGA + U approximations for exchange-correlation functionals. The structural stability and formation energy have been scrutinized revealing more strong bonding compared to pristine $WSe_2$. The electronic structure and magnetic properties of the Mn-doped monolayer - $WSe_2$ have been carefully analyzed. Calculations have been performed to ascertain the energy difference between two dopants in ferromagnetic (FM) and antiferromagnetic (AF) configurations considering nearest neighboring (NN), next nearest neighboring (NNN) and impurity concentration (0-22.22%). The Curie temperature ($T_c$) of the FM to AF phase transition has been determined. Finally, the optical properties of the doped system in various concentrations of the dopant are investigated by substitution of Manganese to Tungsten in a monolayer $WSe_2$. The lattice parameters were calculated for the minimum energy to supercells of 331, 441 and 551 with the vacuum gap c=15$\mathring{A}$ to avoid the interaction between the adjacent monolayers. The system of supercells of $WSe_2$ with different sizes were constructed with the constituent of W and Se-atoms and analyzed without doping. Moreover, the doped monolayers of $WSe_2$ for the mentioned sizes of supercells were analyzed by substituting W atom with a single Mn and two Mn atoms (in nearest-neighbor (NN) and next-nearest-neighbor (NNN) sites). The substitutional doping was done in a range of 0 to 22.2% with a maximum of 2-atoms with NN and NNN sites for the dopant atoms in the supercell. The effective Hubbard parameters ($U_{eff}$) was calculated iteratively for Mn(d) orbitals using a linear response formalism utilizing density functional perturbation theory (DFPT) with ortho-atomic projections method. The effective Hubbard parameter is the difference between the spherically averaged on-site repulsion and on-site Hund's exchange $(U^I=\chi_0^{-1}-\chi^{-1})_{II}$. The computed Value of the effective Hubbard correction parameter $U_{eff}$=6.0 eV for the Mn-atom is utilized in GGA +U calculation.

### 4.2.2 The structure of Mn-doped monolayer $WSe_2$

A pristine 2D-$WSe_2$ is nonmagnetic semiconductor. The electronic structure, band gap, and density of states of the pure $WSe_2$ monolayer were investigated before addressing the Mn-doped monolayer. Then Mn atom substitutions to certain sites of tungsten in monolayer of $WSe_2$ are performed as shown in Figure - 4.11 to Figure - 4.13 for supercell 4x4x1. The optimized pure monolayer has a bond length W–Se = 2.545$\mathring{A}$ and bond angle of $81.4^0$. After doping the Mn-atom on sites of pure $WSe_2$, the bond length Mn-Se = 2.4294$\mathring{A}$ which is slightly shorter than W-Se. But only small increment in the bond angle Se-Mn-Se ($81.94^0$) in comparison to Se-W-Se. For a single Mn to the W atom in a 4×4×1 supercell of $WSe_2$ as shown in Figure - 4.12.

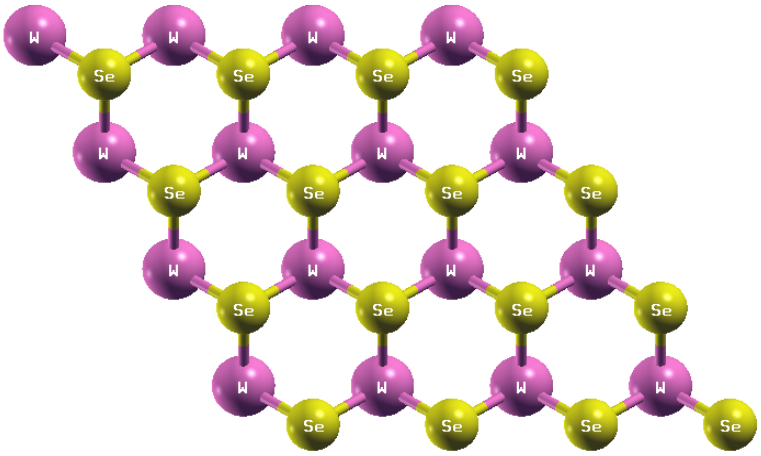


Figure 4.11: Top view of 4x4x1-pristine-$WSe_2$ monolayer

### 4.2.3 Formation Energy

In this part, the electronic and magnetic properties of Mn-doped monolayer $WSe_2$ were investigated. After computing the structural parameters of pristine $WSe_2$, the formation energy

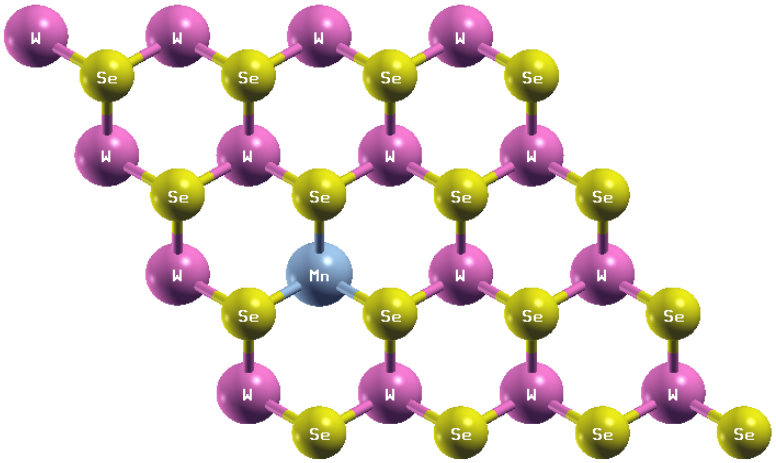


Figure 4.12: Top view optimized single Mn doped 4x4x1 monolayer $WSe_2$

($E_{form}$) was calculated to see the stability of the Mn-doped $WSe_2$ monolayer as,

$$E_{form} = E_{doped} - E_{Pure} - n(\mu_{Mn} - \mu_W) \tag{4.2.1}$$

where, $E_{doped}$ and $E_{pure}$ are the total energies of the monolayer $WSe_2$ with and without doping Mn atom respectively, n is the corresponding number of Mn/W atoms that have been added or removed during substitutional doping, and $\mu_{Mn}$ and $\mu_W$ are chemical potentials of Mn and W atoms, respectively.

Chemical potential calculations for tungsten were conducted under W-rich and Se-rich conditions. Under W-rich conditions, the chemical potential for W is derived from its bulk body-centered cubic (BCC) structure per individual W atom. Conversely, in the Se-rich scenario, the chemical potential of tungsten is determined by the following relationship,

$$\mu_W = \mu_{WSe_2} - 2\mu_{Se} \tag{4.2.2}$$

Were, $\mu_{WSe_2}$ is the total energy per individual primitive cell of pure - $WSe_2$ and $\mu_{Se}$ is the chemical potential of selenium. For Se-atom, the chemical potential $\mu_{Se}$ is the total energy of a

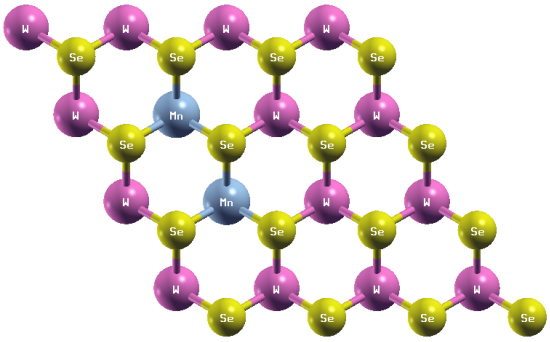

(a)

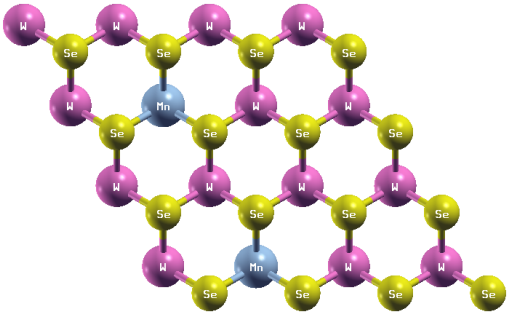

(b)

Figure 4.13: Optimized structure monolayer 4x4x1-$WSe_2$ doped with two Mn atoms doped Mn-Mn in a) nearest neighboring and b) Mn-Mn second-nearest neighboring

single selenium atom in the bulk monoclinic phase of Se. The chemical potential of the dopant (Mn) is also calculated as the total energy of the most stable bulk BCC-structure per individual Mn-atom. All calculated values under both conditions are given in Table1. The result reveals that doping of Mn atom in a monolayer of $WSe_2$ makes the system more strongly bonded in case of Se-rich condition. That is all computed formation energy values in Se-rich condition are negative for different sizes and number of impurity atoms. These results are also in a good agreement with previous theoretical findings on Mn-doped 2D-TMDs [93, 156].

Table 4.4: Formation energy of Mn-doped monolayer-$WSe_2$ in different concentration and neighboring conditions

| size of the layer | Doping sites | $E_{doped}(Ry)$ | $E_{pure}(Ry)$ | $E_{Form}$ (W-rich) | $E_{form}$ (Se-rich) |
|---|---|---|---|---|---|
| 4x4x1 | 1 | -3996.705 | -3944.797 | 0.090 | -0.133 |
| 4x4x1 | 2-NN | -4048.656 | -3944.797 | 0.135 | -0.311 |
| 4x4x1 | 2-NNN | -4048.651 | -3944.797 | 0.140 | -0.306 |
| 3x3x1 | 2-NN | -2322.849 | -2218.950 | 0.094 | -0.352 |
| 3x3x1 | 2-NNN | -2322.772 | -2218.950 | 0.171 | -0.275 |
| 5x5x1 | 2-NN | -6267.648 | -6163.746 | 0.092 | -0.354 |
| 5x5x1 | 2-NNN | -6267.619 | -6163.746 | 0.121 | -0.325 |

### 4.2.4 Electronic and magnetic Properties pristine and Mn-doped $WSe_2$

The electronic structure calculation shows pure $WSe_2$ monolayer is a semiconducting material with a direct band gap of 1.55 eV as demonstrated in Figure 4.14 - (a-c). The direct band gap nature of this monolayer is promising to study further properties of the material for different applications. The spin-up and spin-down configurations have equal energy band gaps and density of states. The results agree with the previously conducted theoretical and experimental works on pristine $WSe_2$ [157]. The total density of states for the constituent elements of pure $WSe_2$ monolayer have equal spin-up and spin-down states with zero net magnetization, confirming the material is a nonmagnetic semiconductor. Doping Manganese or other magnetic elements to certain tungsten atoms in 2D-$WSe_2$ is necessary to address the magnetic properties. Here is a detailed analysis on electronic and magnetic properties of Mn-doped 2D-$WSe_2$.

Doping Manganese or other magnetic elements in substation to certain tungsten atom sites is necessary to address the 2D-$WSe_2$ magnetic properties, and inspiring findings have been observed in this perspective on 2D-TMD materials. We have made detail analysis on the impact of Mn-doping to 2D-$WSe_2$ from different corners such as concentration of the impurity and interaction distance between impurity atoms for nearest and next nearest neighboring cases. The Mn-doped monolayer-$WSe_2$ adopts a semi-metallic nature, deviating from the nonmagnetic characteristics of the pristine 2D $WSe_2$, showcasing impurity bands dispersion near the Fermi level.

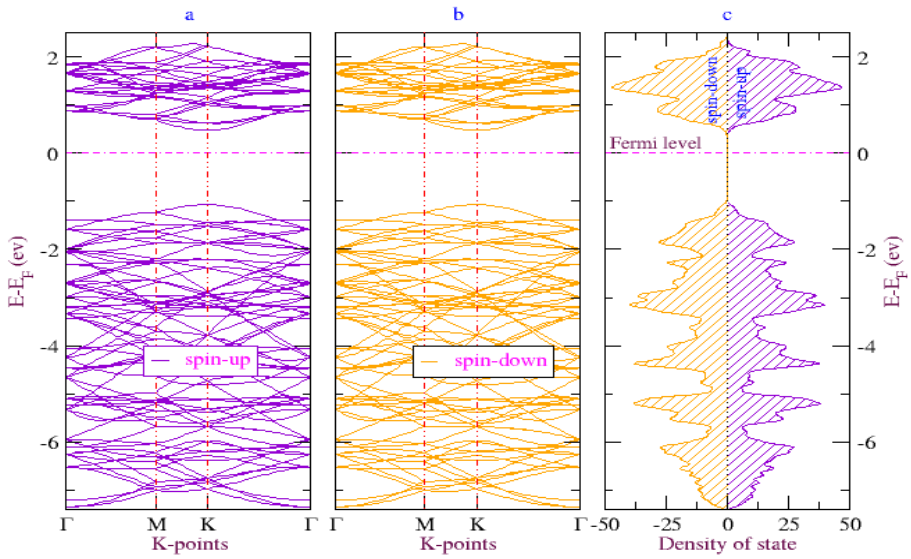


Figure 4.14: The band structure of Pure-$WSe_2$ with (a) spin-up, (b) spin-down, and (c) Density of states respectively.

**Doping of Single Mn-atom**: A monolayer $WSe_2$ doped with a single Mn-atom in substitution to W-atom shows different properties as compared to the monolayer of pristine $WSe_2$. To study the electronic structures and magnetic properties of the Mn-doped monolayer, the band structures are computed using GGA and GGA+U approximations for exchange-correlation potentials independently as shown in Figure 4.15. These results indicate that the spin-up and spin-down states are asymmetric and the substitution of Mn with W-atom can induce magnetic properties in the Mn-doped $WSe_2$ monolayer. The system shows magnetic semiconductor features with a total magnetic moment of $1.00\mu_\beta$. The band crossing at the Fermi level occurs with little dispersion in spin-up band structures (Figure 4.15 - (a)). However, in the spin-down band structure, there is a band gap value of 1.298ev Figure 4.15 - (a) and 1.416ev in Figure 4.15 - (b) with the GGA and GGA+U approximations respectively. The Fermi energy is slightly lower in GGA+U approximations.

**Doping of 2Mn-atoms**: In the case of doping with two Mn-atoms to 3x3x1 and 4x4x1 supercell, the computation is performed with two arrangements in which the Mn-Mn distances are in nearest-neighbor (NN) and the next nearest-neighbor (NNN). The total magnetic mo-

ments of the supercell are 2 $\mu_\beta$ and 4 $\mu_\beta$ according to GGA and GGA+U approximations, respectively for the nearest neighbor arrangement of the impurity atoms. This result agrees with previous theoretical findings [93, 92, 158]. However, doping with two manganese atoms in the second nearest neighbor yields the same total magnetic moment of 2.00 $\mu_\beta$ for GGA and GGA+U approximations. In both configurations, there are greater band overlaps at the Fermi level in spin-up cases in comparison to the single Mn-substitution condition. The band overlap for the nearest-neighbor and next-nearest-neighbor of the 4x4x1 supercell for the two dopant atoms of different setups is described in Figure 4.16 - (a) and Figure 4.17 - (a) respectively. On the other hand, the value of spin-down band gaps is 0.888 eV and 1.01eV for the Mn-Mn in nearest-neighbor for GGA (Figure 4.16 - (a) ) and GGA+U (Figure 4.16 - (b)) approximations, respectively.

For the configuration of Mn-Mn distance in the next-nearest-neighbor, the band gap becomes wider than the Mn-Mn distance in the nearest-neighbor. The calculated values of the spin-down band gap for Mn-Mn distance in the next-nearest-neighbor, are 1.143 eV (GGA, Figure 4.17 - (a)) and 1.396 eV (GGA+U, Figure 4.17 - (b)) approximations, respectively. These results show that the Mn-doped $WSe_2$ monolayer can be tuned to half-metallic or diluted magnetic semiconductors (DMS) based on the direction of spins. The total density of states (TDOS) and partial density of states (PDOS) for one Mn atom substitution are computed for GGA and GGA + U approximations, respectively as described in Figure - 4.18. The overall density of states for the Mn-doped $WSe_2$ monolayer reveals an asymmetry between the spin-up and spin-down components, illustrating the magnetic semiconductor characteristics of the Mn-doped $WSe_2$ system as depicted in Figure - 4.18 - (a) and (b). The polarized spins predominantly originate from the localized 3d electrons of the Mn atom with a minor contribution from the 5d electrons of the W atom and the 4p electrons of the Se atom in the vicinity of the Fermi level. The spin density distribution is primarily concentrated at the Mn atom, as highlighted in the partial density of states (PDOS). Moreover, the total and partial density of states are analyzed for two Mn atom substitutions to W atoms in pure-$WSe_2$ monolayer for the NN and NNN conditions as shown for partial density of states Figure - 4.19 (a and b) and total density of states (Figure - 4.20 - (a) and (b)), respectively. It can be observed that there are

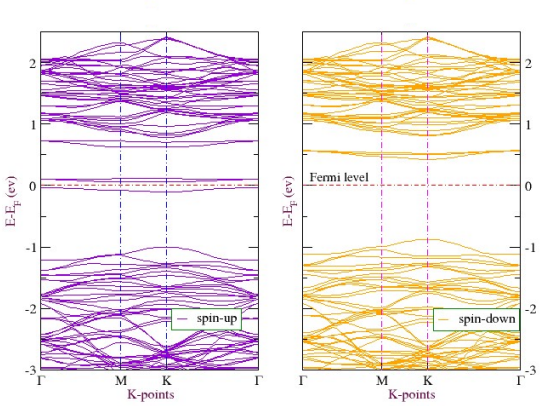


(a)

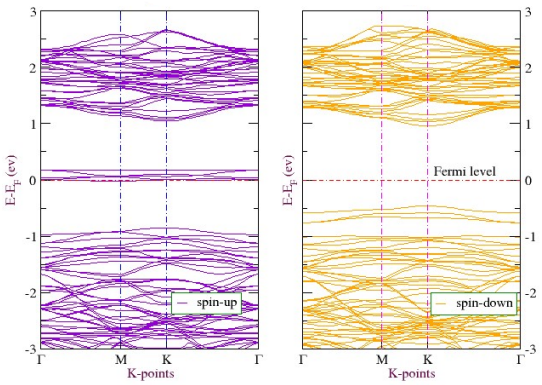


(b)

Figure 4.15: The band structure of 1Mn-doped 4x4x1- $WSe_2$ (a) GGA approximation for spin-up and spin-down, (b) GGA+U approximation for spin-up and spin-down

.

more enhanced band overlaps in the case of two Mn-atom substitutions as indicated in Figure - 4.20 - (a) and (b) compared to a single Mn substitution in Figure - 4.18 - (b)

### 4.2.5 Magnetic interaction and transition temperature ($T_c$)

The magnetic exchange interactions are investigated with two Mn-atoms doped at different spatial positions for different sizes of monolayer supercells with different concentrations of the impurity atoms in the system based on their size. For the doped monolayer, the magnetic interaction depends on both the Mn-Mn site distance and the size of the monolayer. The GGA+U calculations are performed for the doped system with the effective Hubbard parameter for Mn-

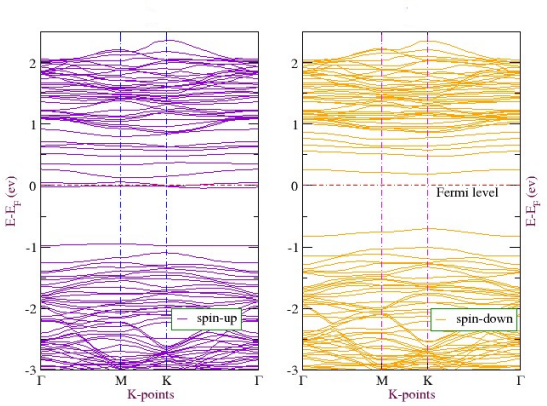


(a)

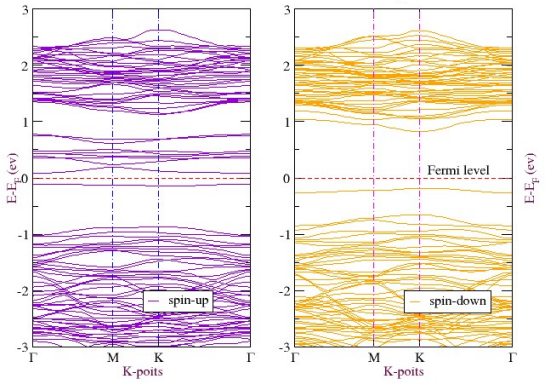


(b)

Figure 4.16: The band structure of 2Mn-doped 4x4x1- $WSe_2$ in nearest-neighbor (a) spin up and spin down in GGA approach (b) spin up and spin-down in GGA+U approach respectively

.

atom ($U_{eff}$=6 eV) determined using density functional perturbation theory (DFPT), which is consistent with previous works [100, 101]. The resulting magnetic moments for the ferromagnetic and antiferromagnetic orders with the GGA and GGA+U approximations is given in Table - 4.5. For the nearest-neighbor (NN) interactions of the impurity atoms, the magnetic moment becomes greater in the GGA+U method ($4.05\mu_{mB}$) in $3 \times 3 \times 1$ supercell and 4.00 $\mu_{mB}$ in $4 \times 4 \times 1$ supercell) than the GGA approximation.

However, the magnetic moment for the second nearest neighbor is 2.00 $\mu_{mB}$ according to GGA and GGA+U approximations, respectively. We can understand from these results that the correlation effect is strongly noticeable for the Mn-3d electrons in the nearest neighboring arrangement of the dopant atoms for the 2D-Mn-doped $WSe_2$. This result agrees with theoret-

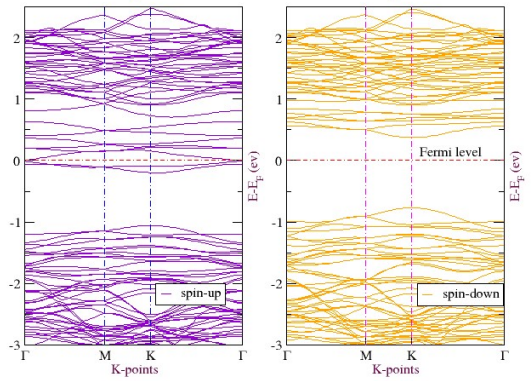


(a)

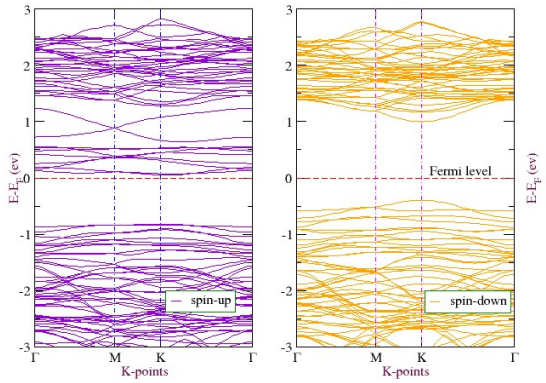


(b)

Figure 4.17: Band structures for 2Mn-doped 4x4x1- $WSe_2$ in second-nearest-neighbor (a) GGA approximation for spin up and spin down , (b) GGA+U approximation for spin up and spin down respectively

.

ical findings [92, 93] for an increment of the magnetic order in nearest neighboring sites of the dopant atoms.

In addition to the total magnetic moment for the nearest-neighbor (NN) arrangement of the dopant atoms, the energy difference between the ferromagnetic and antiferromagnetic interactions is also calculated in both the GGA and GGA+U approaches. The calculated energies are indicated in Table - 4.6. This energy is influenced by the site distance of the constituent impurity atoms, and electron-correlation and hence Hubbard correction becomes vital for interaction energy.

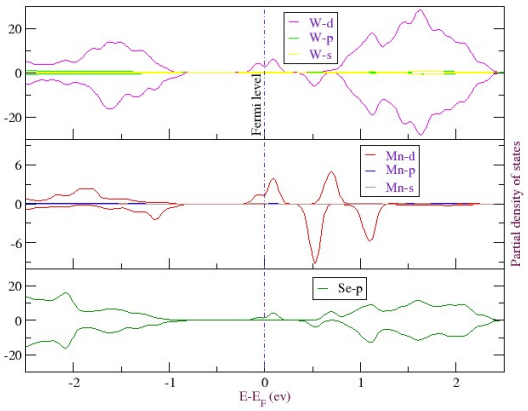


(a)

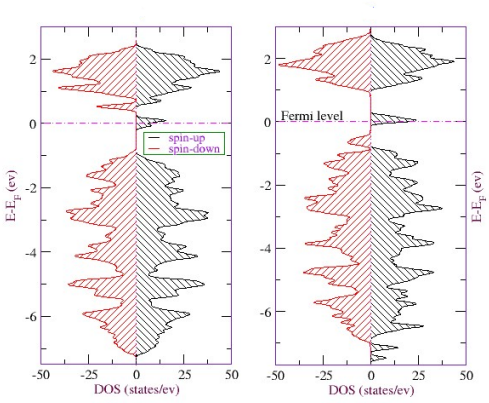


(b)

Figure 4.18: Density of states (DOS) for 1Mn-doped 4x4x1- $WSe_2$ (a) PDOS (b) Total DOS in GGA approximation (left hand side) and in GGA+U approximation (right hand side)

.

### 4.2.6 Ferromagnetic-antiferromagnetic Transition Temperature ($T_c$)

By associating the Heisenberg Hamiltonian with the mean field approximation, one can calculate the Curie temperature ($T_c$) which represents the temperature below which the system exhibits long-range ferromagnetic ordering [159] using Equation (4.2.3)

$$\frac{3}{2}k_B T_c = \frac{-\Delta E}{n} \tag{4.2.3}$$

Where n-is the number of the nearest neighboring impurity atoms (Mn) which is 2 in this calculation. Nevertheless, magnetic ordering in the doped system is significantly influenced by magnetic percolation and the mean-field approximation tends to overestimate $T_c$ in these

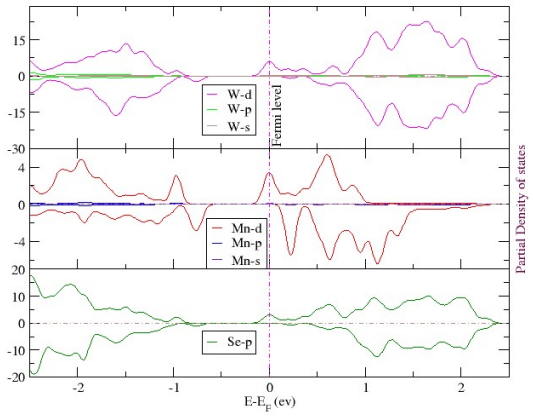


(a)

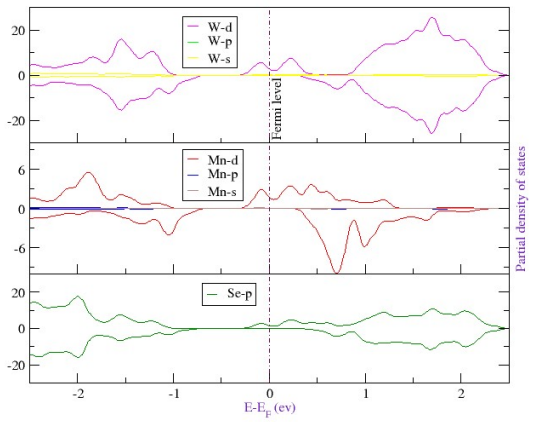


(b)

Figure 4.19: Partial density of states (PDOS) for 2Mn-doped 4x4x1- $WSe_2$ in (a) nearest-neighboring of Mn-Mn (b) next nearest-neighboring of Mn-Mn

.

systems. The overestimation becomes adjusted by using empirical relation which relates the critical temperature of the mean-field approximation ($T_c^{MFA}$) with corrected critical temperature ($T_c^{corr}$ ) as [94]

$$T_c^{corr} = 0.506 T_c^{MFA} \tag{4.2.4}$$

where $T_c^{corr}$ is corrected critical temperature for 2D hexagonal lattice determined utilizing Ising model and $T_c^{MFA}$ is the predicted critical temperature using mean field approximation and the calculated values using DFT and DFT+U methods. The values indicate that the FM to AFM transition is above the room temperature in lower concentration of dopant and for Mn-concentration between 8-12.5%. However, for higher concentration of dopant (22.2%) the

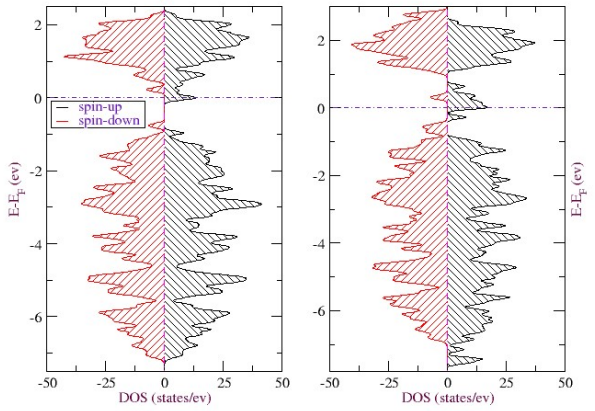


(a)

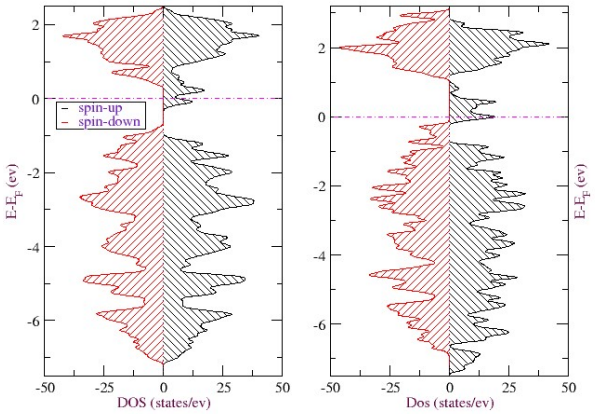


(b)

Figure 4.20: Total density of states for doped 2D-$WSe_2$ (a) in NN Mn-Mn for GGA approximation (left-hand side) and for GGA+U approximation (right-hand side) (b) in NNN Mn-Mn for GGA approximation (LHS) and for GGA+U approximation (RHS)

.

FM to AFM transition is below the room temperature. Thus, the dopant clustering weakens the magnetic interaction and the magnetic ordering becomes itinerant in agreement with other finding [102]. Furthermore, the material is a viable option for high temperature 2D-DMS. The result confirms that ferromagnetism in this system can be altered by varying the concentration of magnetic dopants (Mn-atoms).

Table 4.5: Summary of the magnetic properties of Mn-Doped monolayer-$WSe_2$

| size of the layer | Number of the dopant | $\mu_m$ in FM (GGA) | $\mu_m$ in AFM (GGA) | $\mu_m$ in FM (GGA+U) | $\mu_m$ in AFM (GGA+U) |
|---|---|---|---|---|---|
| 4x4x1 | 2-NN | 2.00 | 0.00 | 4.00 | 0.03 |
| 4x4x1 | 2-NNN | 2.00 | -0.04 | 2.00 | 0.00 |
| 3x3x1 | 2-NN | 2.00 | 0.00 | 4.05 | 0.03 |
| 3x3x1 | 2-NNN | 2.00 | 0.00 | 2.00 | 0.03 |
| 5x5x1 | 2-NN | 2.00 | -0.02 | 4.00 | -0.02 |
| 5x5x1 | 2-NNN | 2.00 | 0.00 | 2.00 | 0.00 |

Table 4.6: Calculated transition temperature with the corresponding energy in GGA+U method in nearest neighboring interaction of the dopant.

| size of the layer | content of the dopant | Mn-atoms in NN | $\Delta E(ev)$ | mean-field ($T_c^{MFA}$) | Corrected $T_c(k)$ |
|---|---|---|---|---|---|
| 5x5x1 | 8 | 2.00 | -0.227 | 877.12 | 443.82 |
| 4x4x1 | 12.5 | 2.00 | -0.230 | 890.21 | 450.45 |
| 3x3x1 | 22.22 | 2.00 | -0.113 | 436.31 | 220.77 |

### 4.2.7 Optical properties of pure and Mn-doped $WSe_2$ monolayer

To compute the optical properties, the complex dielectric function $\varepsilon(\omega)$ is employed within an independent particle formalism [153] given in equations 4.1.2. The imaginary part, $\varepsilon_2(\omega)$, is ascertained through the momentum dipole transition matrix elements between the electronic states in the valence band and the conduction band, utilizing long-wavelength approximations [154], 4.1.3. The dispersion of the real part of the dielectric function $\varepsilon_1(\omega)$ was determined using the imaginary part by Kramers-Kronig relations [155], as in 4.1.4. The refractive index, the extinction coefficient, both derivable from the complex dielectric function. Absorption coefficient ($\alpha(\omega)$), and energy loss function ($L(\omega)$) and other optical parameters were also derived from dielectric functions, Equations- 4.1.5-4.1.10

The optical properties encompassing the dielectric function, optical absorption, and energy loss function, as well as the refractive index and extinction coefficient, are explored in both parallel and perpendicular directions to the plane of the monolayer of pure and Mn-doped 2D-$WSe_2$. This investigation spans the photon energy range from 0 to 12 eV, with the calculation details provided. The real part of the dielectric function, $\varepsilon_1(\omega)$, for parallel and perpendicular polarizations are shown in Figure - 4.21 (a) and 4.21 (b) respectively. It shows that the static dielectric function values for near zero energy $\varepsilon_1$ (0ev) is 6.4 for undoped and 9.0 to 18.75% dop-

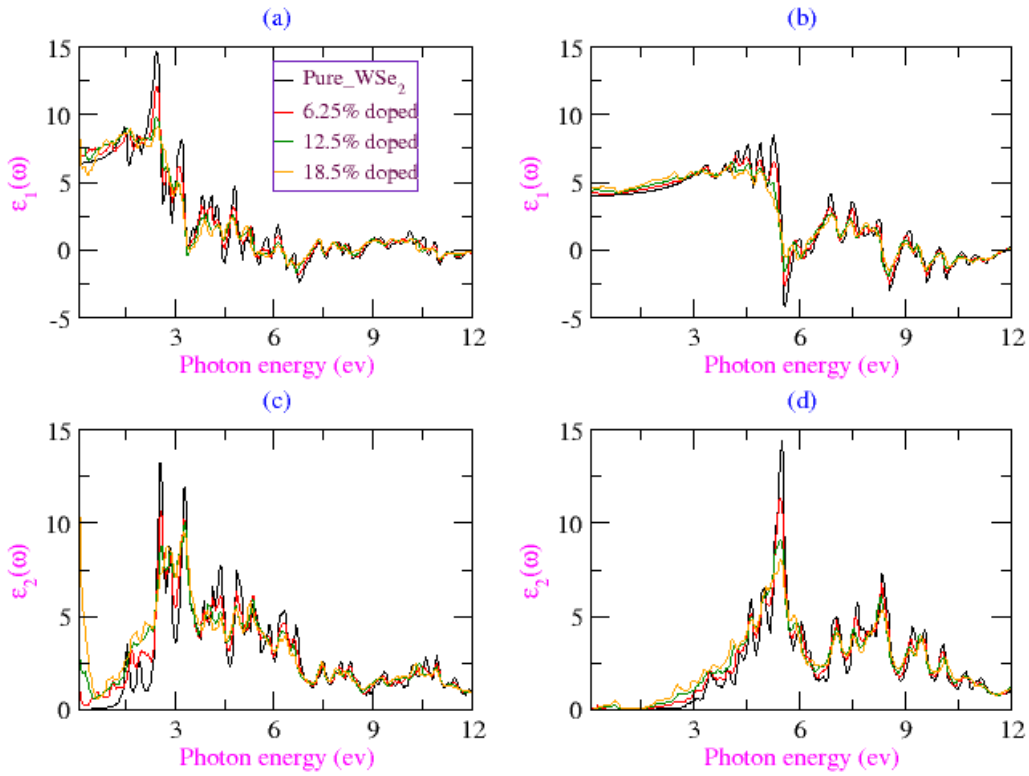


Figure 4.21: Dielectric function versus photon energy, parallel polarization (a) for real and (b) for imaginary and perpendicular polarization (c) for real and (d) for imaginary part to Mn-doped 2H-$WSe_2$ monolayer respectively

ing which indicates larger dielectric impurity added to the system. The static dielectric constant near zero energy $\varepsilon_1$ (0ev) for perpendicular polarization also increases with the amount of impurity but slower than the parallel with 4.0 (0%) and 4.6(18.75%). The peak of the real part of the dielectric constant decreases in both polarizations with $\varepsilon_1$ (2.43ev)=14.67,12.1,9.8 and 9.0 to 0%, 6.25%, 12.5% and 18.75% substitution in parallel and for $\varepsilon_1$ ($\varepsilon \approx$5.0ev)=8.55,6.85,6.0,5.8 in perpendicular respectively. The imaginary part of the dielectric constant increases with the amount of impurity (0-11.43)arb.unit for doping (0-3) Mn-atoms at $\varepsilon_2$ ($\varepsilon \approx$0ev) respectively to 4×4×1-$WSe_2$. Then $\varepsilon_2$ decreases by increasing dopant, $\varepsilon_2$ ($\varepsilon \approx$2.7ev) with 13.2(0%), 10.68(6.25%), 8.8(12.5%) 8.75(18.75%) respectively, in parallel propagation as in Figure 4.21 (c). For perpendicular polarization, $\varepsilon_2$ the peak values appear at the same region with slight variation in the impurity content as shown in Figure 4.21 - (d). The refractive index ($n(\omega)$), Figure - 4.22 (a), increases with the photon energy (0-2.5ev) to parallel and (0-5ev) for perpen-

dicular propagation then decreases and becomes constant for high energy in both polarizations. The extinction coefficient ($\kappa(\omega)$), shown in Figure - 4.22 (c) and (d) for polarization parallel and perpendicular to the plane of the monolayer respectively is slightly larger with high impurity and all drops down to zero at photon energy of 0.75ev then increases to peak 2.2 at 3.4ev in parallel polarization. The extinction coefficient for perpendicular propagation becomes slightly larger for higher impurity concentration for the photon energy less than 5ev and attain the highest peak value 2.75 at 5.5ev and near zero for higher energy photons for both propagations. The absorption coefficient, $\alpha(\omega)$, is calculated for the parallel and perpendicular polarizations

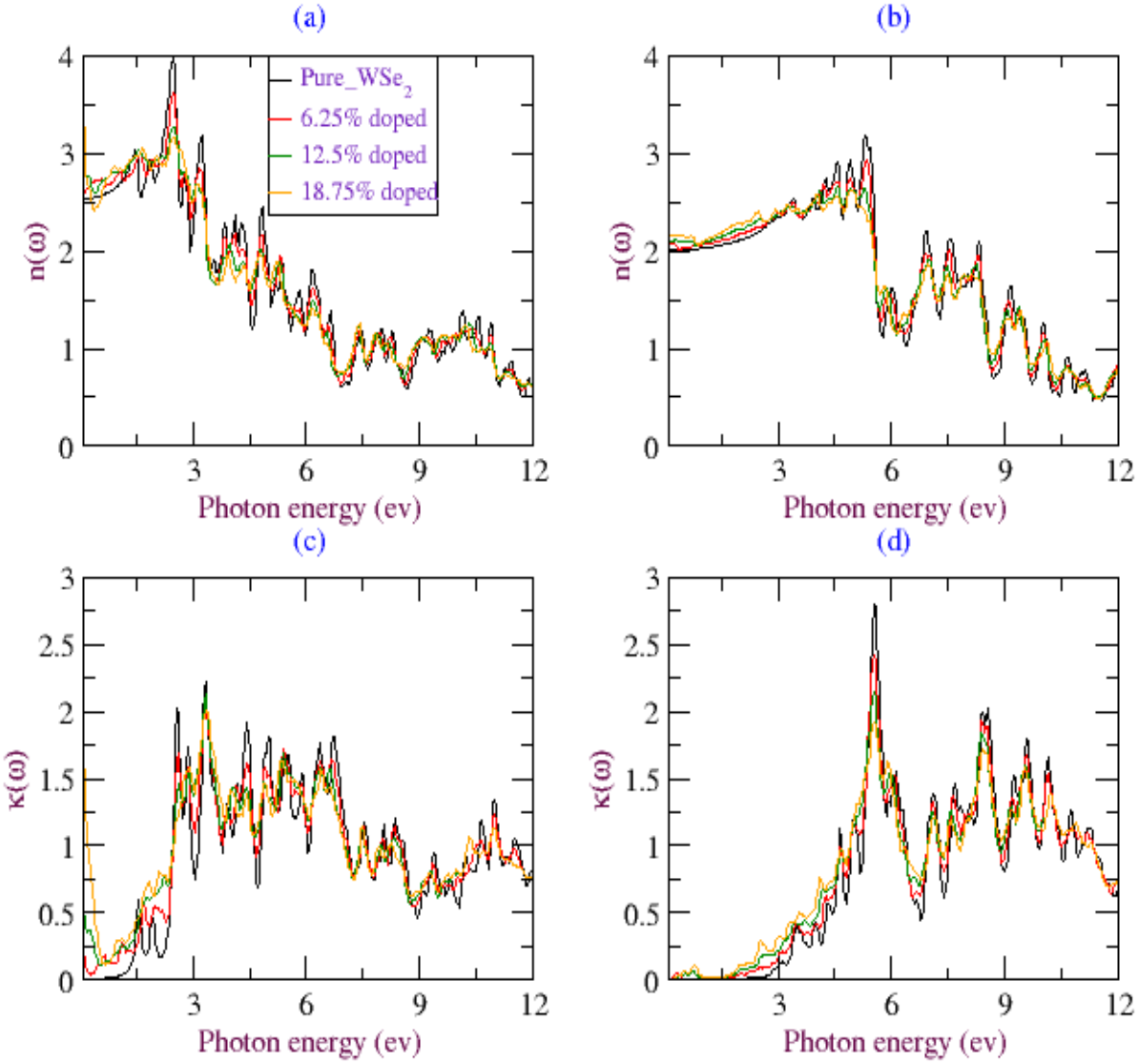


Figure 4.22: (a) Refractive index (b) extinction coefficient for parallel and (c) refractive index (d) extinction coefficient for perpendicular propagation of Mn-doped 2D-$WSe_2$

with the electron energy loss (EEL) function as shown in figure-4.23 (a-d). In lower energy band it has highly increasing absorption (2.5ev-6.75ev) in parallel and (2.5ev-5.55ev) in perpendicular) to the system as shown in Figure -4.23 (a) and (b). The maximum peak values of absorption appear at 8.6ev with $1.73\times10^{6}cm^{-}1$ in perpendicular and $1.47\times10^{6}cm^{-}1$ at 11ev in parallel propagation. On the other hand, the absorption coincides with the undoped system and becomes continuous with larger Mn substitution to the pure monolayer of 2H-$WSe_2$. The elec-

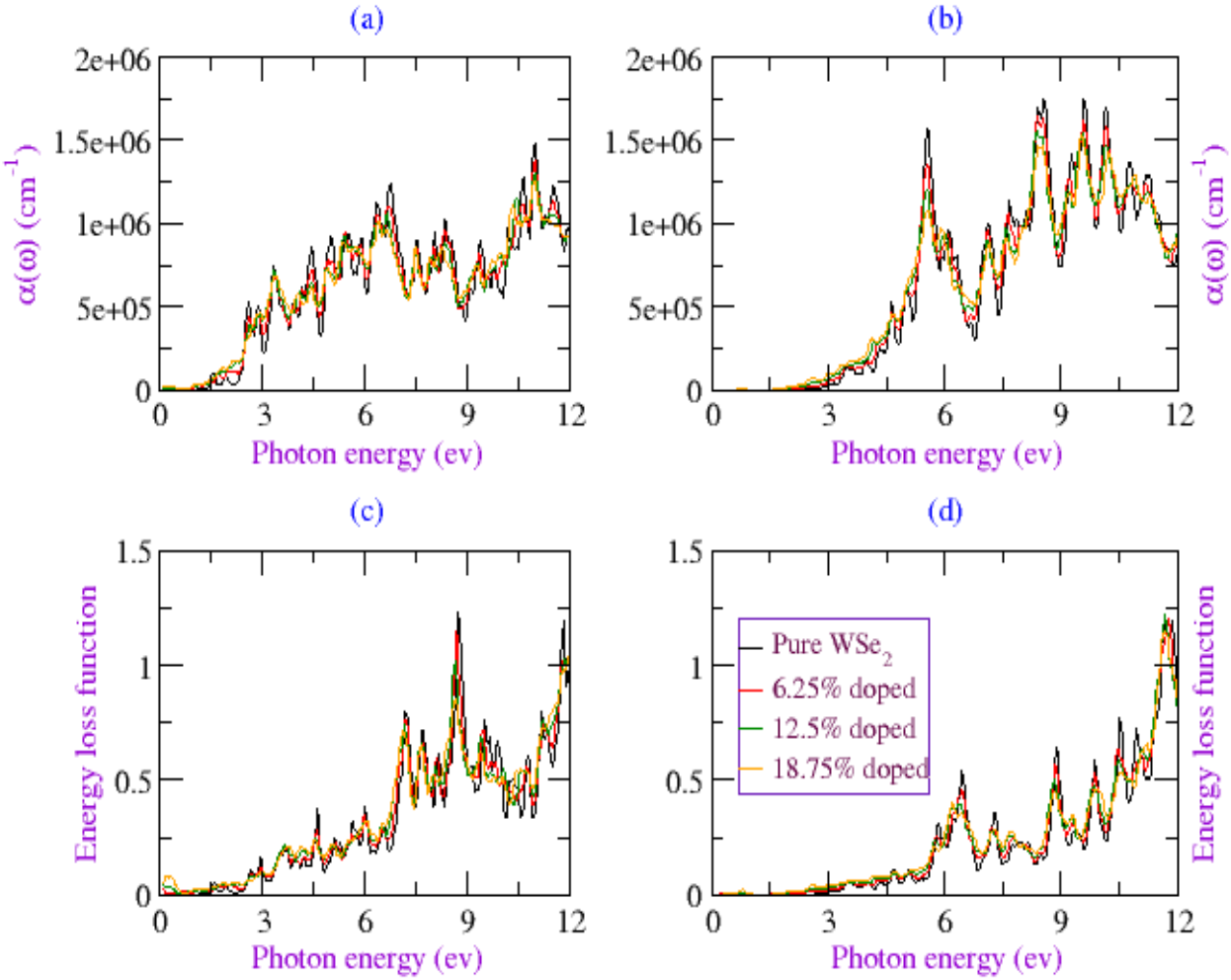


Figure 4.23: Absorption coefficient (a) parallel (b) perpendicular propagation and electron energy loss function (c) parallel (d) perpendicular propagation for Mn-doped monolayer 2D-$WSe_2$

tron energy loss (EEL) function of Mn-doped 2D-$WSe_2$ with various impurity concentration

is indicated in Figure -4.23 (c) and (d) for parallel and perpendicular polarization respectively. Peaks in the measured spectra can thus derive zeros of $\varepsilon_1(\omega)$ (when $\varepsilon_2(\omega)$ is not too large), which correspond to collective plasmon excitations, or from structures $\varepsilon_2(\omega)$ which are due to valence-conduction inter-band transitions. The EEL function for parallel polarization is 2.4 at 17ev and 2.5 at 16.43ev perpendicular polarization to the plane of doped monolayer. The doping will be important for low energy optical devices because of the red shift observed in infrared region.

## 4.3 Tuning the electronic and optical properties of 2D $WS_2/WSe_2$ heterobilayer under biaxial strain

### 4.3.1 Introduction

In this work we have studied the $WS_2/WSe_2$ heterobilayer with the application of biaxial strain on the two-dimensions leaving the optimum vertical free vacuum space of the gap between the layers undisturbed. The effect of biaxial strain, both in compression and tension, in this scenario is the key for tuning the band structure and the optical properties of the $WS_2/WSe_2$ heterobilayer. The analysis is based on DFT with generalized gradient approximation (GGA) approximation and all results have been discussed in detail and necessary conclusions have been summarized about the findings in this work. For structural and electronic parameter calculations, a 3x3x1 supercell of 2H-bilayer heterostructure of $WS_2/WSe_2$ vertically stacked in AB-stacking. The lattice parameters a=b and the interlayer spacing c of the heterolayer was calculated for the minimum energy. Biaxial strain in tension and compression was considered for the heterobilayer in two-dimensions of the plane the heterostructure keeping the gap between individual layers unaffected. The optical properties are determined using time-dependent density functional theory (TD-DFT). The strain dependent electronic and optical properties had been under compressive and tensile stresses with biaxial strain of -4% to 4% to the plane of the heterostructure.

### 4.3.2 Structural properties of $WS_2/WSe_2$ heterobilayer

The structure of 2D-$WS_2/WSe_2$ heterobilayer is composed of two kinds of strongly bonded monolayers which are stack together by a weak van der Waals interaction. The lattice structures of $WS_2/WSe_2$ heterobilayer is shown in Figure-4.24a-4.24c below with top, front and side views. Both the individual layer lattice constant and the vertical offset between the two layers of $WS_2/WSe_2$ are calculated with the minimum energy principle of the heterostructure. The two-dimensional lattice constant a=b is achieved with a=b=3.28$\mathring{A}$ for individual unit cell of $WS_2/WSe_2$ heterobilayer as shown in Figure-4.25 with the lowest energy below. On the other

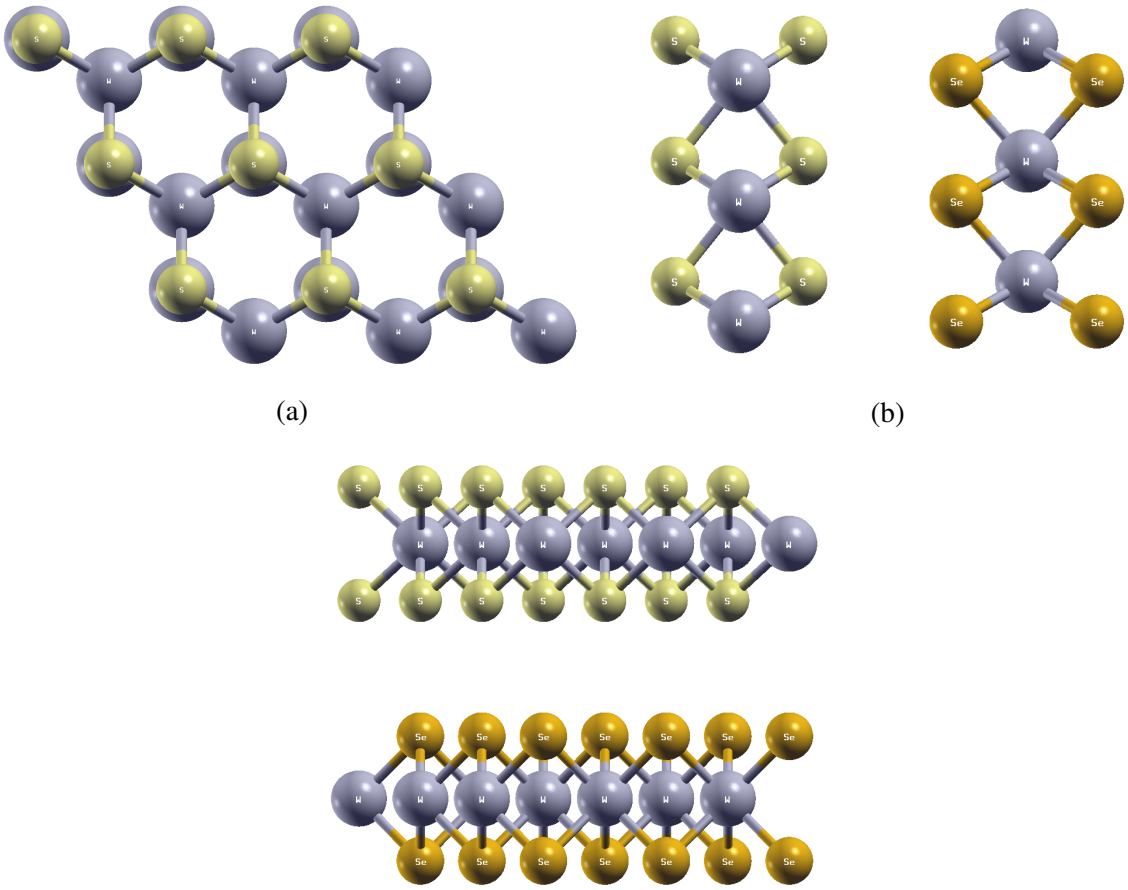

Figure 4.24: Optimized structure of $WS_2/WSe_2$ heterobilayer (a) top view (b) side view and (c) front view

.

hand, the vertical interlayer distance between the two slabs of $WS_2/WSe_2$ layers c=13.14$\mathring{A}$ is achieved with the minimum energy as shown in Figure-4.26. The interlayer gap and the lattice constants are necessary parameters in the structure. In Addition to free $WS_2/WSe_2$ heterostructure is considered with the effect of biaxial strain. The structural parameters, the bond lengths and the bond angles are affected by stain. In case of the biaxial compression both bond length and bond angle decrease with strain whereas both parameters increase with increasing tensile strain.

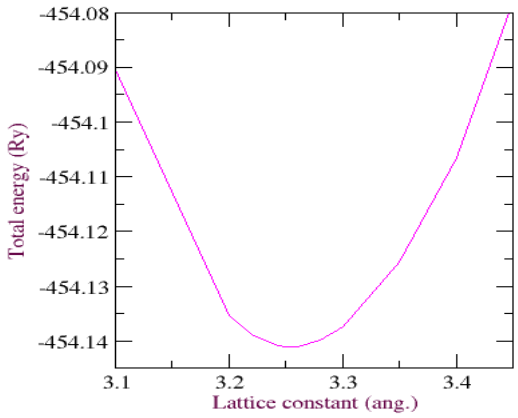


Figure 4.25: Lattice constant of $WS_2/WSe_2$ heterobilayer using the GGA approximation.

### 4.3.3 Electronic properties of $WS_2/WSe_2$ heterobilayer under biaxial strain

The band structure and density of states have been analyzed in existence of both compressive and tensile strain along the two-dentitional plane (slabs) of the heterobilayer. The response of the material for both tensile and compressive strains is considered with varying the amount of strain imposed. The computations have been performed using GGA approximation approximations as shown in Figure-4.27 for compressive to tensile strain. In this computation (Figure-4.27), the undisturbed (no stress) is indicated in the middle and the valence band maximum (VBM) and conduction band minimum (CBM) attained at the momentum space gamma-point and has a direct band gap of 0.52ev which indicates that $WS_2/WSe_2$ heterobilayer is direct band gap semiconductor having narrower energy band gap in comparison to the individual $WS_2$ and $WSe_2$ monolayers. Meanwhile, when the heterostructure is in compression and the compressive stress is gradually increasing (to left-hand-side of Figure-4.27), the band gap increases with more negative strain and shift from direct to indirect band gap for more than 4% compressive strain is forced to the heterobilayer. On the other hand, when the heterobilayer is under tensile stress, the band gap decreases with tensile strain (to right-hand-side of Figure-4.27) and the conduction and valence bands overlap for 3% and higher tensile (positive) strain. This

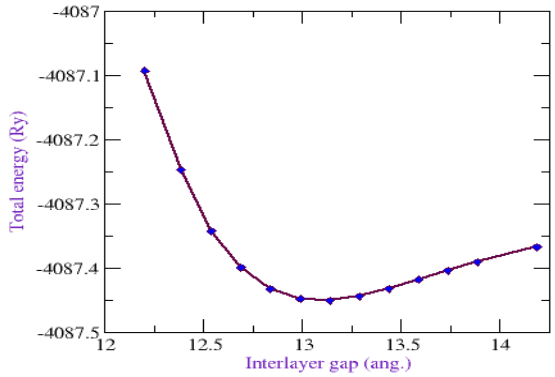


Figure 4.26: The inter-layer spacing between the layers of $WS_2/WSe_2$ bilayer using the GGA approximation.

shows that $WS_2/WSe_2$ heterobilayer has fascinating tunable direct band gap which depends on external strain and suitable for various low band gap electronic applications.

The total density of states (DOS) and partial density of states (PDOS) are also calculated for $WS_2/WSe_2$ heterobilayer in strained and unstrained conditions indicated in Figure-4.28 to Figure-4.29. Again, in DOS calculations, the analysis is done considering both the GGA and GGA+U approximations for compressive and tensile strain annoyance as well as unstrained.

In case of unstrained condition, as shown in Figure-4.28, the LHS of Figure-4.28(a) is the total DOS is above the partial density of states and on the right-hand side. In this computation, the fermi level is above the valence band maximum and below the conduction minimum and the obtained output is equivalent and the W(5d)-orbital is major for the CBM and VBM. When the system is under compressive stress with negative strain of 4% as shown in Figure-4.29, the VBM is more of Se-atoms with p-orbital and the orientations of the fermi level is different from the previous case that the fermi level is at higher energy nearer to the conduction band.

Finally, we have calculated the DOS and PDOS to which the heterobilayer is under tensile strain and the result is indicated in Figure-4.30 in the GGA approximations. As seen from the DOS/PDOS/ diagram, the W-3d state is free of barrier between the valence band maximum and

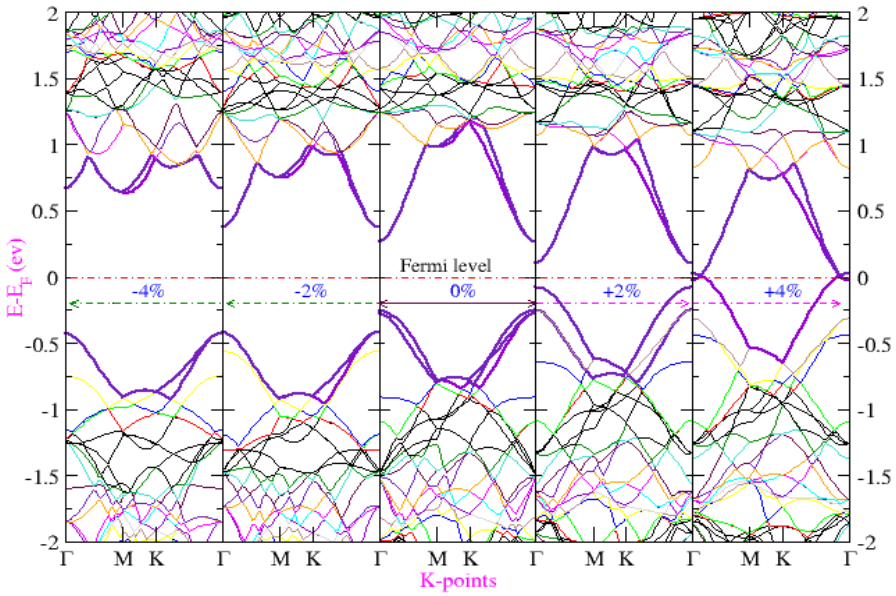


Figure 4.27: The band structure of $WS_2/WSe_2$ heterobilayer in GGA approximation with tension, compression and undisturbed cases.

conduction band minimum for large tensile strain to $WS_2/WSe_2$ heterostructure.

### 4.3.4 Optical properties of $WS_2/WSe_2$ heterobilayer under biaxial strain

In order to determine the optical properties of $WS_2/WSe_2$ heterobilayer, the complex dielectric function $\varepsilon(\omega)$, within an independent particle formalism is used [153] with the refractive index n($\omega$) and extinction coefficient $\chi(\omega)$ evaluated from complex dielectric functions and the resulting absorption coefficient $\alpha(\omega)$ and energy loss function $L(\omega)$ have been determined referring equations 4.1.2 to 4.1.10

The optical properties, are investigated in perpendicular polarization to the plane of the heterobilayer of $WS_2/WSe_2$ in the photon energy range of 0 to 20eV. The dielectric function $\varepsilon_1(\omega)$ when the heterolayer $WS_2/WSe_2$ is exposed to the polarization perpendicular to the two-dimensional plane of the layer, as shown in Figure-4.31, the static dielectric constant for zero energy $\varepsilon_1(0)$ is 7.95 when the system is unstrained. On the other hand, the dielectric function slightly increases with compressive strain (Figure-4.31a) and decreases with the tensile strain

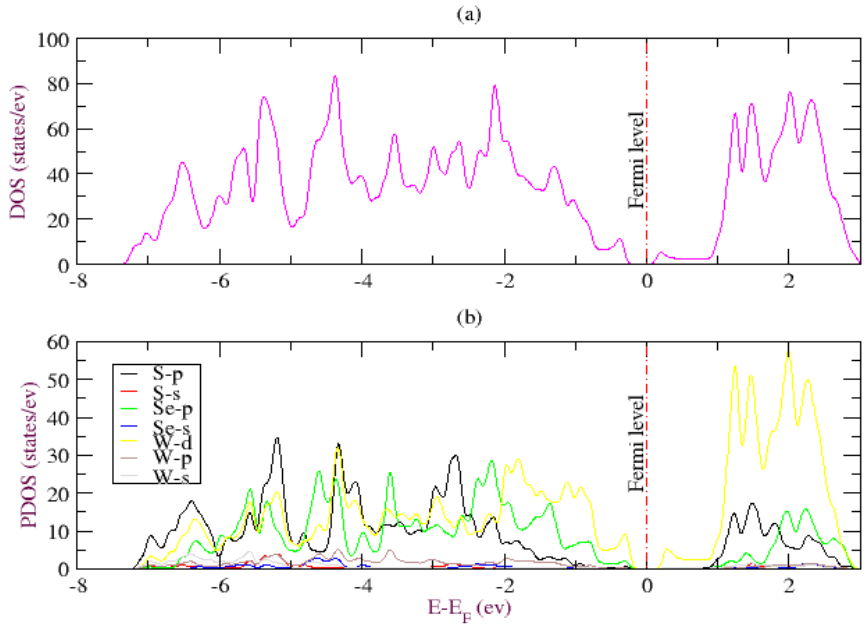


Figure 4.28: The density of states (DOS) of the $WS_2/WSe_2$ heterobilayer without strain for in GGA approximation (a) Total DOS and (b) Partial DOS

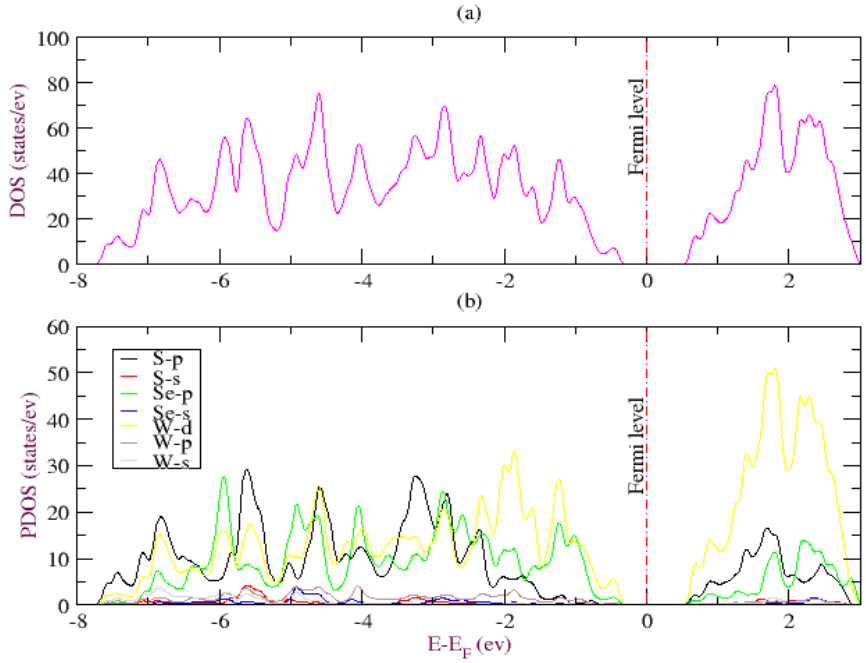


Figure 4.29: The density of states of $WS_2/WSe_2$ heterobilayer in compressive strain (-4%) (a) Total DOS (b) Partial DOS.

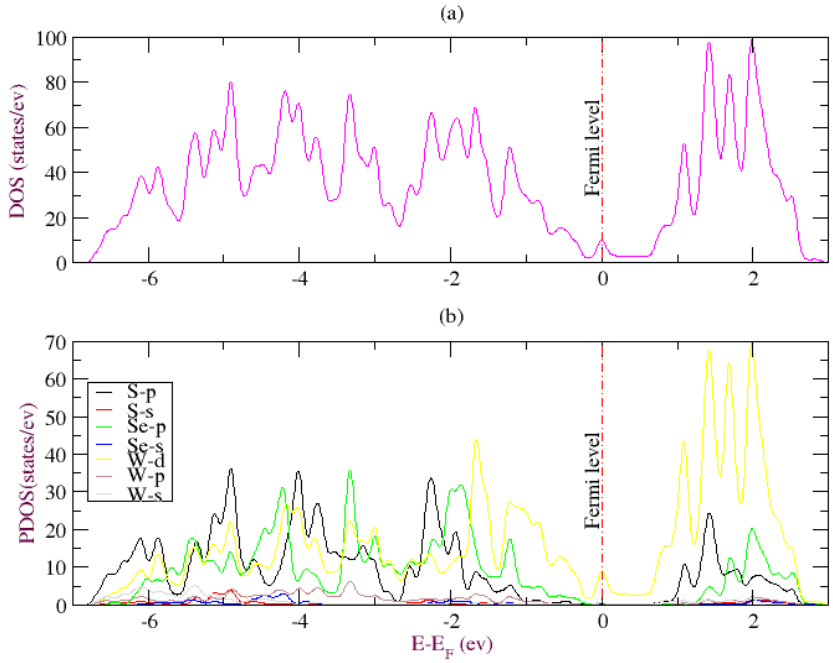


Figure 4.30: The density of states of $WS_2$/$WSe_2$ heterobilayer under tensile stress with strain (+4%) GGA approximation (a) TDOS (b) PDOS

in 0-5ev energy range and irregular for 5-15ev and becomes constant for higher energy photons.

The peak of $\varepsilon_1(\omega)$ is 14.42 at 3.57 eV for unstrained, 15.68 for 3.67 eV, and 15.5 for 3.7ev in 2%, and 4% respectively for biaxial compression as shown in Figure-4.31a. The peak values of $\varepsilon_1(\omega)$ are also calculated biaxial tension with tensile strain 2%, and 4% as 13.22 at 4.7ev, and 13.0 at 4.57ev respectively as shown in Figure-4.31b. The negative values in the $\varepsilon_1(\omega)$ spectra (-6.63) at 6.40 eV in 4% compressive strain corresponds to the peak in the reflectivity spectra. The imaginary part of the dielectric function perpendicular to the plane of $WS_2$/$WSe_2$ heterobilayer with respect to the incoming photon is shown in Figure-4.32 with biaxial compressive and tensile strain as indicated in Figure-4.32a and Figure-4.32b respectively.

The imaginary part of the dielectric function is zero below the photon energy of 2eV and has peak values in range of 5eV-6eV and finally decreases down to zero for high energy photons. The other optical parameters such as the refractive index $n(\omega)$, extinction coefficient $\chi(\omega)$ for polarization perpendicular to the plane of the heterobilayer are shown in Figure-4.33(a) and (b) and Figure-4.34 (a) and (b) in compression and tension respectively. The value of static

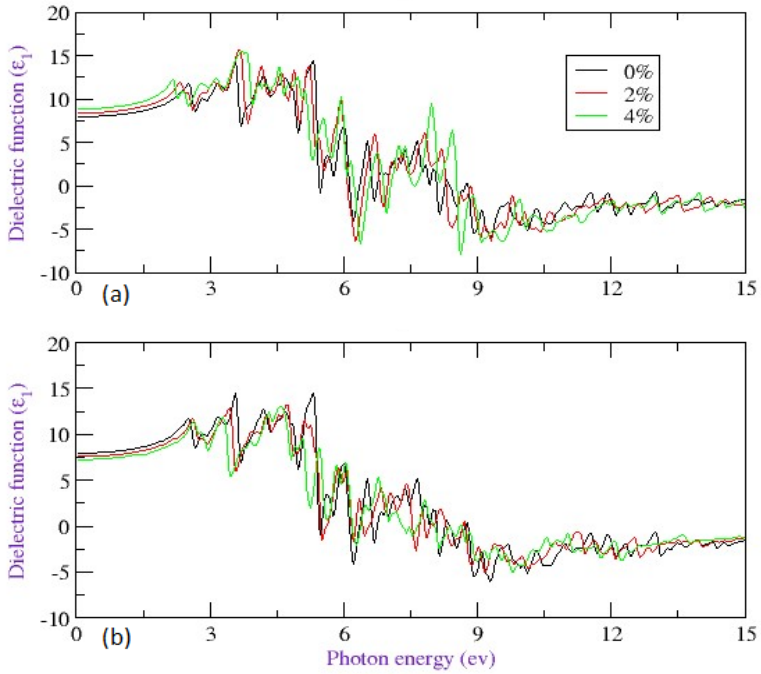


Figure 4.31: The real dielectric function for propagation along the plane of the layer for $WS_2/WSe_2$ heterobilayer (a) the system is under compression (b) the system is under tension

refractive index $n(0)$ is nearly 3 for all case and has peak values 4.3 at 5.3eV for equilibrium and the refractive index property nearly identical for both compressive and tensile strain (0-4%). The refractive index of the material is less dispersed in tensile strain than of compressive strain. The peak value of the extinction coefficient is 3.6 at 8.6 eV for 4% biaxial compression, 3.10 at 5.41 eV for unstrained and 3.11 at 5.44 eV for no strain to the system.

The refractive index of the material is less dispersed in tensile strain than that of compressive strain. The peak value of the extinction coefficient is 3.6 at 8.6 eV for 4% biaxial compression, 3.10 at 5.41 eV for unstrained and 2.9 at 5.4 eV for 2% biaxial tension. The peak value of the extinction coefficient for $WS_2/WSe_2$ shows blue shift as compared to the tensile stress. The absorption coefficient is also calculated in equilibrium and biaxial compression and tension of the heterobilayer as shown in Figure-Figure-4.35 (a) and (b) for compression and tension respectively. The absorption coefficient is increasing with photon energy 0-10eV and the decreases with further increasing of energy. The magnitude of the absorption coefficient of the heterostructure is less dispersed in tensile strain than compressive strain. Moreover, red shift is detected when $WS_2/WSe_2$ heterostructure is under biaxial tension while blue shift is ob-

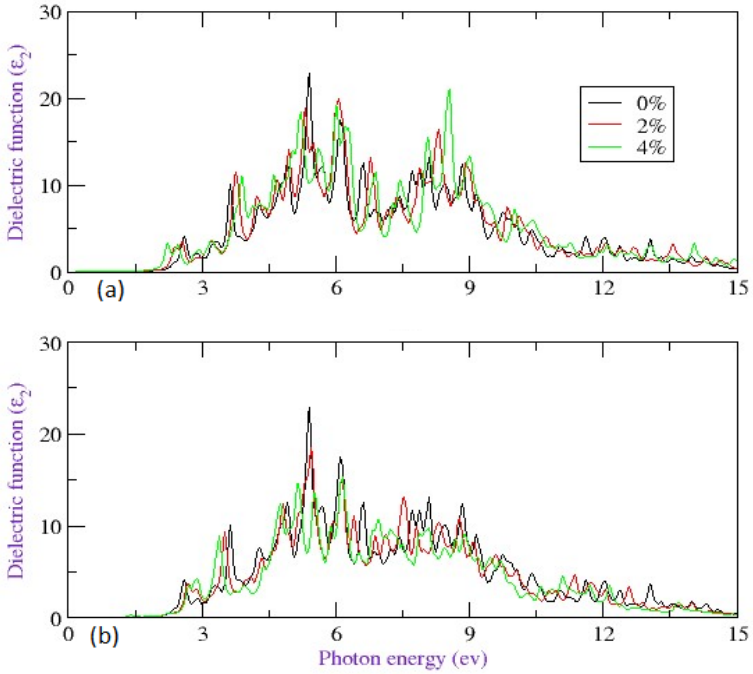


Figure 4.32: Imaginary dielectric function of perpendicular propagation for $WS_2/WSe_2$ heterobilayer (a) with compressive strain (b) tensile strain

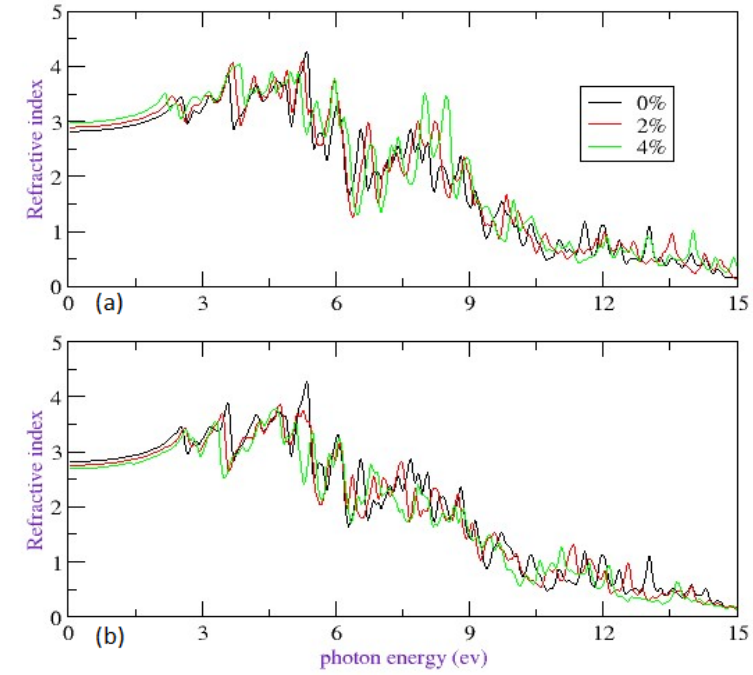


Figure 4.33: Refractive index of $WS_2/WSe_2$ heterobilayer (a) in biaxial compression (b) in biaxial tension

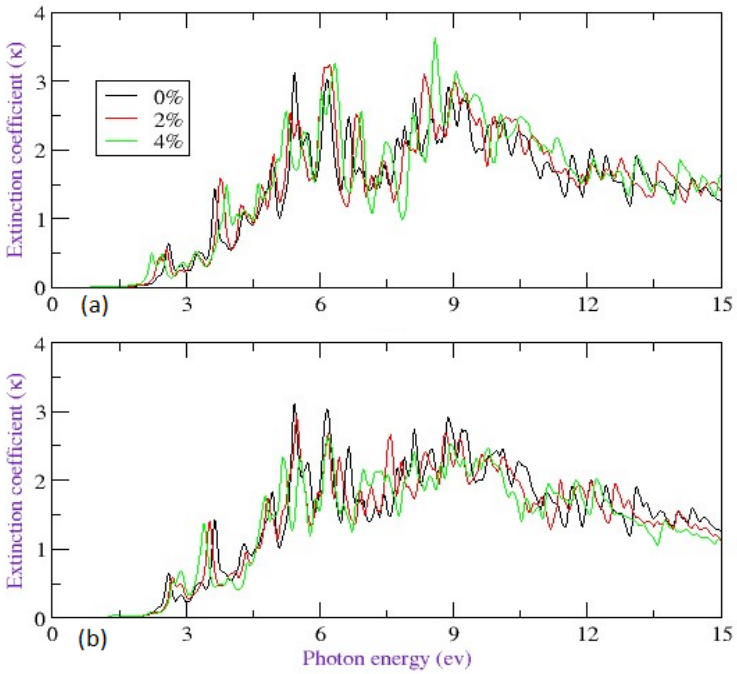


Figure 4.34: Extinction coefficient of $WS_2/WSe_2$ heterostructure (a) under biaxial compression (b) under biaxial tension

served when it is under biaxial compression in transition of visible light to UV-spectrum. The electron energy loss function (EELS) of the heterostructure for unstrained, biaxial compression, and biaxial tensile strain is described in Figure-4.36 (a) and (b) for the biaxial compression and tension of the heterobilayer.

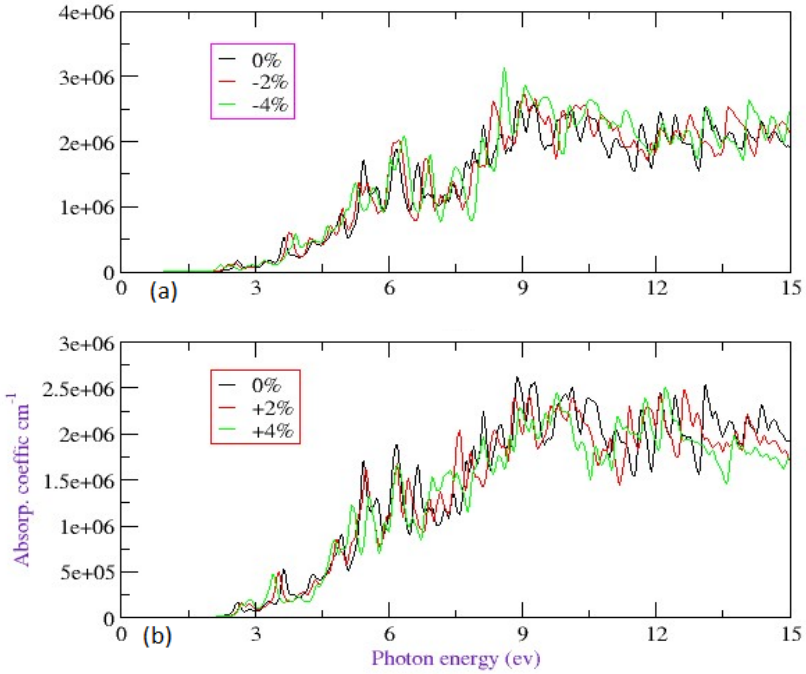


Figure 4.35: Absorption coefficient of $WS_2/WSe_2$ heterostructure (a) under biaxial compression (b) under biaxial tension

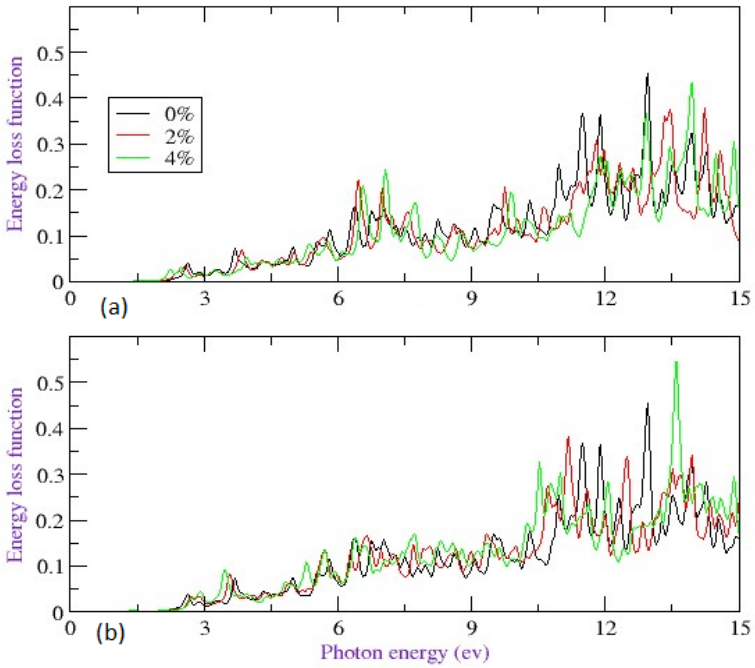


Figure 4.36: Energy loss function of $WS_2/WSe_2$ heterostructure under (a) biaxial compression (b) biaxial tension

# Chapter 5

# Summary and Conclusions

## 5.1 Summary

In 2D-tungsten dichalcogenides ($WX_2$) the structural, electronic, magnetic and optical properties were studied in first principles method using density functional theory. Monolayer $WX_2$ has a direct band gap semiconductor irrespective of its bulk counterpart which has indirect band gap. The high electron mobility and low effective mass in comparison to the molybdenum makes the tungsten families of TMDs more encouraging to new investigations. Pristine 2D-$WX_2$ is nonmagnetic material and becomes magnetic when the constituent W-atom is replaced by magnetic materials like Mn in substitutional doping. In addition, 2D tungsten dichalcogenides have good elastic limit with biaxial strain without altering the direct band gap and suitable for band gap engineering.

## 5.2 Conclusions

- The bond length of $WTe_2$ monolayer and $WS_2$/$WSe_2$ heterobilayers vary with the application external stresses likewise the bond length Mn-Se becomes shorter than W-Se in Mn-doped $WSe_2$.

- The band gap of $WTe_2$ monolayer in GGA approximation is underestimated and GGA+U is applied on the other hand the band gap become wider under biaxial compression and

narrower under biaxial tension.

- For $WTe_2$ monolayer small biaxial compressive or tensile stresses tune the band gap without Shifting the orientation of VBM and CBM and the system remains as a direct band gap semiconductor.

- In lattice vibration under compressive/tensile stress, DFPT+U is used to capture the effect of electronic localization of vibrational frequencies over the entire vibrational spectrum which improves the DFPT.

- The optical properties of 2D-$WTe_2$ monolayer such as complex dielectric property, refractive index, absorption coefficient, electron energy loss function and the reflectivity are investigated.

- The band gap of pure 2D-$WSe_2$ becomes 1.55ev and the result is in agreement with recent theoretical and experimental works on the material.

- Near the Fermi level, the band overlap occurs for spin up electrons while the band in spin-down remains unaltered in doped 2D-$WSe_2$ which shows that Mn-doped $WSe_2$ becomes half metallic material.

- The total magnetic moment in nearest neighboring interaction of Mn-Mn is significantly larger in GGA+U than GGA which indicates the electron correlation effect is high.

- The magnetic interaction energy increases with the impurity concentration to the optimum value but decreases fast for further increasing of the impurity atoms.

- FM in Mn-doped 2D-$WSe_2$ is tuned by adjusting the amount of the Mn atoms in substitutional doping and the material becomes promising for two-dimensional electronic and spintronic applications above room temperature.

- $WS_2$/$WSe_2$ heterostructure is a direct bandgap material which has less energy band gap than individual $WS_2$ and $WSe_2$ monolayers.

- The band gap of $WS_2/WSe_2$ heterobilayer is tunable under biaxial strain with increasing in compressive strain whereas decreasing by tensile strain without shifting of VBM and CBM.
- The projected density of state of $WS_2/WSe_2$ heterostructure shows W (d) orbital is more dominant both in the valence band maximum and conduction band minimum.
- The strained system of the heterostructure shows red shift for biaxial tension and blue shift in biaxial compression with respect to the unstrained one.
- The heterobilayer has high absorption coefficient in the visible light region this made $WS_2/WSe_2$ heterobilayer promising for photovoltaic optoelectronic applications.

## 5.3 Future Plans

In our future work, we have interest

- To study the elasticity of family of $WX_2$ of few layers with large strain since we determined the materials have promising electronic optical and magnetic properties in small strain.
- To study the materials properties by doping in various elements in substitution of W, S, Se or Te since we have got promising results in Mn substitution to W in 2D $WX_2$.
- To study using more advanced tools like the hybrid functionals and GW in addition to GGA and GGA+U approximations.
- To use YAMBO code combination to the Quantum-Espresso to study our materials for exited states because the QE package is used to calculate the ground states
- To finally develop the materials in experiment which can be used in photovoltaic and spintronics applications.

# Refrences


[1] K. S. Novoselov, A. K. Geim, S. V. Morozov, D.-e. Jiang, Y. Zhang, S. V. Dubonos, I. V. Grigorieva, and A. A. Firsov, "Electric field effect in atomically thin carbon films," *science*, vol. 306, no. 5696, pp. 666–669, 2004.

[2] A. K. Geim and I. V. Grigorieva, "Van der waals heterostructures," *Nature*, vol. 499, no. 7459, pp. 419–425, 2013.

[3] K. S. Novoselov, D. Jiang, F. Schedin, T. Booth, V. Khotkevich, S. Morozov, and A. K. Geim, "Two-dimensional atomic crystals," *Proceedings of the National Academy of Sciences*, vol. 102, no. 30, pp. 10 451–10 453, 2005.

[4] A. Ayari, E. Cobas, O. Ogundadegbe, and M. S. Fuhrer, "Realization and electrical characterization of ultrathin crystals of layered transition-metal dichalcogenides," *Journal of applied physics*, vol. 101, no. 1, 2007.

[5] S. Roy, X. Zhang, A. B. Puthirath, A. Meiyazhagan, S. Bhattacharyya, M. M. Rahman, G. Babu, S. Susarla, S. K. Saju, M. K. Tran *et al.*, "Structure, properties and applications of two-dimensional hexagonal boron nitride," *Advanced Materials*, vol. 33, no. 44, p. 2101589, 2021.

[6] K. F. Mak, C. Lee, J. Hone, J. Shan, and T. F. Heinz, "Atomically thin mos 2: a new direct-gap semiconductor," *Physical review letters*, vol. 105, no. 13, p. 136805, 2010.

[7] S. Ahmad, S. Mukherjee *et al.*, "A comparative study of electronic properties of bulk mos2 and its monolayer using dft technique: application of mechanical strain on mos2 monolayer," *Graphene*, vol. 3, no. 04, p. 52, 2014.

[8] Z. Ji, L. Zhang, G. Xie, W. Xu, D. Guo, J. Luo, and B. Prakash, "Mechanical and tribological properties of nanocomposites incorporated with two-dimensional materials," *Friction*, vol. 8, pp. 813–846, 2020.

[9] H. Schmidt, F. Giustiniano, and G. Eda, "Electronic transport properties of transition metal dichalcogenide field-effect devices: surface and interface effects," *Chemical Society Reviews*, vol. 44, no. 21, pp. 7715–7736, 2015.

[10] J. Hu, X. Shi, S. Wu, K. Ho, and Z. Zhu, "Dependence of electronic and optical properties of mos2 multilayers on the interlayer coupling and van hove singularity, nanoscale res," 2019.

[11] M. Ye, D. Winslow, D. Zhang, R. Pandey, and Y. K. Yap, "Recent advancement on the optical properties of two-dimensional molybdenum disulfide thin films," in *Photonics*, vol. 2, no. 1. MDPI, 2015, pp. 288–307.

[12] H. Wang, D. Nezich, J. Kong, and T. Palacios, "Graphene frequency multipliers," *IEEE Electron Device Letters*, vol. 30, no. 5, pp. 547–549, 2009.

[13] R. Coehoorn, C. Haas, J. Dijkstra, C. d. Flipse, R. De Groot, and A. Wold, "Electronic structure of mose 2, mos 2, and wse 2. i. band-structure calculations and photoelectron spectroscopy," *Physical review B*, vol. 35, no. 12, p. 6195, 1987.

[14] F. A. Rasmussen and K. S. Thygesen, "Computational 2d materials database: electronic structure of transition-metal dichalcogenides and oxides," *The Journal of Physical Chemistry C*, vol. 119, no. 23, pp. 13 169–13 183, 2015.

[15] T. E. Graedel, E. M. Harper, N. T. Nassar, P. Nuss, and B. K. Reck, "Criticality of metals and metalloids," *Proceedings of the National Academy of Sciences*, vol. 112, no. 14, pp. 4257–4262, 2015.

[16] G.-B. Liu, D. Xiao, Y. Yao, X. Xu, and W. Yao, "Electronic structures and theoretical modelling of two-dimensional group-vib transition metal dichalcogenides," *Chemical Society Reviews*, vol. 44, no. 9, pp. 2643–2663, 2015.

[17] H. Yoo, K. Heo, M. H. R. Ansari, and S. Cho, "Recent advances in electrical doping of 2d semiconductor materials: Methods, analyses, and applications," *Nanomaterials*, vol. 11, no. 4, p. 832, 2021.

[18] R. Cheng, S. Jiang, Y. Chen, Y. Liu, N. Weiss, H.-C. Cheng, H. Wu, Y. Huang, and X. Duan, "Few-layer molybdenum disulfide transistors and circuits for high-speed flexible electronics," *Nature communications*, vol. 5, no. 1, p. 5143, 2014.

[19] H. R. Gutiérrez, N. Perea-López, A. L. Elías, A. Berkdemir, B. Wang, R. Lv, F. López-Urías, V. H. Crespi, H. Terrones, and M. Terrones, "Extraordinary room-temperature photoluminescence in triangular ws2 monolayers," *Nano letters*, vol. 13, no. 8, pp. 3447–3454, 2013.

[20] D. Braga, I. Gutieérrez Lezama, H. Berger, and A. F. Morpurgo, "Quantitative determination of the band gap of ws2 with ambipolar ionic liquid-gated transistors," *Nano letters*, vol. 12, no. 10, pp. 5218–5223, 2012.

[21] W. Zhang, Z. Huang, W. Zhang, and Y. Li, "Two-dimensional semiconductors with possible high room temperature mobility," *Nano Research*, vol. 7, pp. 1731–1737, 2014.

[22] S. Kretschmer, H.-P. Komsa, P. Bøggild, and A. V. Krasheninnikov, "Structural transformations in two-dimensional transition-metal dichalcogenide mos2 under an electron beam: insights from first-principles calculations," *The Journal of Physical Chemistry Letters*, vol. 8, no. 13, pp. 3061–3067, 2017.

[23] T. Kosmala, P. Palczynski, M. Amati, L. Gregoratti, H. Sezen, C. Mattevi, S. Agnoli, and G. Granozzi, "Strain induced phase transition of ws2 by local dewetting of au/mica film upon annealing," *Surfaces*, vol. 4, no. 1, pp. 1–8, 2020.

[24] X. Gan, L. Y. S. Lee, K.-y. Wong, T. W. Lo, K. H. Ho, D. Y. Lei, and H. Zhao, "2h/1t phase transition of multilayer mos2 by electrochemical incorporation of s vacancies," *ACS Applied Energy Materials*, vol. 1, no. 9, pp. 4754–4765, 2018.

[25] R. Kappera, D. Voiry, S. E. Yalcin, W. Jen, M. Acerce, S. Torrel, B. Branch, S. Lei, W. Chen, S. Najmaei *et al.*, "Metallic 1t phase source/drain electrodes for field effect transistors from chemical vapor deposited mos2," *Apl Materials*, vol. 2, no. 9, 2014.

[26] R. Kappera, D. Voiry, S. E. Yalcin, B. Branch, G. Gupta, A. D. Mohite, and M. Chhowalla, "Phase-engineered low-resistance contacts for ultrathin mos2 transistors," *Nature materials*, vol. 13, no. 12, pp. 1128–1134, 2014.

[27] S. Song, D. H. Keum, S. Cho, D. Perello, Y. Kim, and Y. H. Lee, "Room temperature semiconductor–metal transition of mote2 thin films engineered by strain," *Nano letters*, vol. 16, no. 1, pp. 188–193, 2016.

[28] L. Liu, S. B. Kumar, Y. Ouyang, and J. Guo, "Performance limits of monolayer transition metal dichalcogenide transistors," *IEEE Transactions on Electron Devices*, vol. 58, no. 9, pp. 3042–3047, 2011.

[29] K. Liu, Q. Yan, M. Chen, W. Fan, Y. Sun, J. Suh, D. Fu, S. Lee, J. Zhou, S. Tongay *et al.*, "Elastic properties of chemical-vapor-deposited monolayer mos2, ws2, and their bilayer heterostructures," *Nano letters*, vol. 14, no. 9, pp. 5097–5103, 2014.

[30] R. Zhang, V. Koutsos, and R. Cheung, "Elastic properties of suspended multilayer wse2," *Applied Physics Letters*, vol. 108, no. 4, 2016.

[31] D. Çakır, F. M. Peeters, and C. Sevik, "Mechanical and thermal properties of h-mx2 (m= cr, mo, w; x= o, s, se, te) monolayers: A comparative study," *Applied Physics Letters*, vol. 104, no. 20, 2014.

[32] A. Falin, M. Holwill, H. Lv, W. Gan, J. Cheng, R. Zhang, D. Qian, M. R. Barnett, E. J. Santos, K. S. Novoselov *et al.*, "Mechanical properties of atomically thin tungsten dichalcogenides: Ws2, wse2, and wte2," *ACS nano*, vol. 15, no. 2, pp. 2600–2610, 2021.

[33] H. Zhan, D. Guo, and G. Xie, "Two-dimensional layered materials: from mechanical and coupling properties towards applications in electronics," *Nanoscale*, vol. 11, no. 28, pp. 13 181–13 212, 2019.

[34] Z. Peng, X. Chen, Y. Fan, D. J. Srolovitz, and D. Lei, "Strain engineering of 2d semiconductors and graphene: from strain fields to band-structure tuning and photonic applications," *Light: Science & Applications*, vol. 9, no. 1, p. 190, 2020.

[35] P. Kang, M. C. Wang, P. M. Knapp, and S. Nam, "Crumpled graphene photodetector with enhanced, strain-tunable, and wavelength-selective photoresponsivity," *Advanced Materials*, vol. 28, no. 23, pp. 4639–4645, 2016.

[36] M. K. Blees, A. W. Barnard, P. A. Rose, S. P. Roberts, K. L. McGill, P. Y. Huang, A. R. Ruyack, J. W. Kevek, B. Kobrin, D. A. Muller *et al.*, "Graphene kirigami," *Nature*, vol. 524, no. 7564, pp. 204–207, 2015.

[37] J. Lee, S. J. Yun, C. Seo, K. Cho, T. S. Kim, G. H. An, K. Kang, H. S. Lee, and J. Kim, "Switchable, tunable, and directable exciton funneling in periodically wrinkled ws2," *Nano Letters*, vol. 21, no. 1, pp. 43–50, 2020.

[38] P. Rivera, H. Yu, K. L. Seyler, N. P. Wilson, W. Yao, and X. Xu, "Interlayer valley excitons in heterobilayers of transition metal dichalcogenides," *Nature nanotechnology*, vol. 13, no. 11, pp. 1004–1015, 2018.

[39] F. Carrascoso, D.-Y. Lin, R. Frisenda, and A. Castellanos-Gomez, "Biaxial strain tuning of interlayer excitons in bilayer mos2," *Journal of Physics: Materials*, vol. 3, no. 1, p. 015003, 2019.

[40] Y. He, Y. Yang, Z. Zhang, Y. Gong, W. Zhou, Z. Hu, G. Ye, X. Zhang, E. Bianco, S. Lei *et al.*, "Strain-induced electronic structure changes in stacked van der waals heterostructures," *Nano letters*, vol. 16, no. 5, pp. 3314–3320, 2016.

[41] B. Peng, H. Zhang, H. Shao, Y. Xu, X. Zhang, and H. Zhu, "Thermal conductivity of monolayer mos 2, mose 2, and ws 2: interplay of mass effect, interatomic bonding and anharmonicity," *RSC advances*, vol. 6, no. 7, pp. 5767–5773, 2016.

[42] Y. Cai, J. Lan, G. Zhang, and Y.-W. Zhang, "Lattice vibrational modes and phonon thermal conductivity of monolayer mos 2," *Physical Review B*, vol. 89, no. 3, p. 035438, 2014.

[43] V. I. Anisimov, F. Aryasetiawan, and A. Lichtenstein, "First-principles calculations of the electronic structure and spectra of strongly correlated systems: the lda+ u method," *Journal of Physics: Condensed Matter*, vol. 9, no. 4, p. 767, 1997.

[44] S. L. Dudarev, G. A. Botton, S. Y. Savrasov, C. Humphreys, and A. P. Sutton, "Electron-energy-loss spectra and the structural stability of nickel oxide: An lsda+ u study," *Physical Review B*, vol. 57, no. 3, p. 1505, 1998.

[45] P. Giannozzi, S. De Gironcoli, P. Pavone, and S. Baroni, "Ab initio calculation of phonon dispersions in semiconductors," *Physical Review B*, vol. 43, no. 9, p. 7231, 1991.

[46] A. Floris, S. de Gironcoli, E. Gross, and M. Cococcioni, "Vibrational properties of mno and nio from dft+ u-based density functional perturbation theory," *Physical Review B*, vol. 84, no. 16, p. 161102, 2011.

[47] Q. H. Wang, K. Kalantar-Zadeh, A. Kis, J. N. Coleman, and M. S. Strano, "Electronics and optoelectronics of two-dimensional transition metal dichalcogenides," *Nature nanotechnology*, vol. 7, no. 11, pp. 699–712, 2012.

[48] T. Yu and M. Wu, "Valley depolarization dynamics and valley hall effect of excitons in monolayer and bilayer mos2," *Physical Review B*, vol. 93, no. 4, p. 045414, 2016.

[49] C.-K. Shih, "Coherently strained in-plane atomic layer heterojunctions," *NPG Asia Materials*, vol. 7, no. 12, pp. e231–e231, 2015.

[50] C. Huang, S. Wu, A. M. Sanchez, J. J. Peters, R. Beanland, J. S. Ross, P. Rivera, W. Yao, D. H. Cobden, and X. Xu, "Lateral heterojunctions within monolayer mose 2–wse 2 semiconductors," *Nature materials*, vol. 13, no. 12, pp. 1096–1101, 2014.

[51] D. Li, W. Xiong, L. Jiang, Z. Xiao, H. Rabiee Golgir, M. Wang, X. Huang, Y. Zhou, Z. Lin, J. Song *et al.*, "Multimodal nonlinear optical imaging of mos2 and mos2-based van der waals heterostructures," *ACS nano*, vol. 10, no. 3, pp. 3766–3775, 2016.

[52] N. Huo, S. Tongay, W. Guo, R. Li, C. Fan, F. Lu, J. Yang, B. Li, Y. Li, and Z. Wei, "Novel optical and electrical transport properties in atomically thin wse2/mos2 p–n heterostructures," *Advanced Electronic Materials*, vol. 1, no. 5, p. 1400066, 2015.

[53] T. Hong, B. Chamlagain, T. Wang, H.-J. Chuang, Z. Zhou, and Y.-Q. Xu, "Anisotropic photocurrent response at black phosphorus–mos 2 p–n heterojunctions," *Nanoscale*, vol. 7, no. 44, pp. 18 537–18 541, 2015.

[54] X. Hu, L. Kou, and L. Sun, "Stacking orders induced direct band gap in bilayer mose2-wse2 lateral heterostructures," *Scientific reports*, vol. 6, no. 1, p. 31122, 2016.

[55] S. Yu, Q. Rice, B. Tabibi, Q. Li, and F. J. Seo, "Piezoelectricity in wse 2/mos 2 heterostructure atomic layers," *Nanoscale*, vol. 10, no. 26, pp. 12 472–12 479, 2018.

[56] K. Kośmider and J. Fernández-Rossier, "Electronic properties of the mos 2-ws 2 heterojunction," *Physical Review B*, vol. 87, no. 7, p. 075451, 2013.

[57] P. Rivera, J. R. Schaibley, A. M. Jones, J. S. Ross, S. Wu, G. Aivazian, P. Klement, K. Seyler, G. Clark, N. J. Ghimire *et al.*, "Observation of long-lived interlayer excitons in monolayer mose2–wse2 heterostructures," *Nature communications*, vol. 6, no. 1, p. 6242, 2015.

[58] F. Wang, J. Wang, S. Guo, J. Zhang, Z. Hu, and J. Chu, "Tuning coupling behavior of stacked heterostructures based on mos2, ws2, and wse2," *Scientific reports*, vol. 7, no. 1, p. 44712, 2017.

[59] C. Cho, J. Wong, A. Taqieddin, S. Biswas, N. R. Aluru, S. Nam, and H. A. Atwater, "Highly strain-tunable interlayer excitons in mos2/wse2 heterobilayers," *Nano letters*, vol. 21, no. 9, pp. 3956–3964, 2021.

[60] A. Van Der Zande and J. Hone, "Inspired by strain," *Nature Photonics*, vol. 6, no. 12, pp. 804–806, 2012.

[61] R. Roldán, A. Castellanos-Gomez, E. Cappelluti, and F. Guinea, "Strain engineering in semiconducting two-dimensional crystals," *Journal of Physics: Condensed Matter*, vol. 27, no. 31, p. 313201, 2015.

[62] D. Lloyd, X. Liu, J. W. Christopher, L. Cantley, A. Wadehra, B. L. Kim, B. B. Goldberg, A. K. Swan, and J. S. Bunch, "Band gap engineering with ultralarge biaxial strains in suspended monolayer mos2," *Nano letters*, vol. 16, no. 9, pp. 5836–5841, 2016.

[63] M. Feierabend, A. Morlet, G. Berghäuser, and E. Malic, "Impact of strain on the optical fingerprint of monolayer transition-metal dichalcogenides," *Physical Review B*, vol. 96, no. 4, p. 045425, 2017.

[64] A. Kumar and P. Ahluwalia, "Electronic structure of transition metal dichalcogenides monolayers 1h-mx 2 (m= mo, w; x= s, se, te) from ab-initio theory: new direct band gap semiconductors," *The European Physical Journal B*, vol. 85, pp. 1–7, 2012.

[65] W. Zhao, Z. Ghorannevis, L. Chu, M. Toh, C. Kloc, P.-H. Tan, and G. Eda, "Evolution of electronic structure in atomically thin sheets of ws2 and wse2," *ACS nano*, vol. 7, no. 1, pp. 791–797, 2013.

[66] K. Xu, P. Chen, X. Li, C. Wu, Y. Guo, J. Zhao, X. Wu, and Y. Xie, "Ultrathin nanosheets of vanadium diselenide: a metallic two-dimensional material with ferromagnetic charge-density-wave behavior," *Angewandte Chemie*, vol. 125, no. 40, pp. 10 671–10 675, 2013.

[67] B. T. Zhou, N. F. Yuan, H.-L. Jiang, and K. T. Law, "Ising superconductivity and majorana fermions in transition-metal dichalcogenides," *Physical Review B*, vol. 93, no. 18, p. 180501, 2016.

[68] A. Ramasubramaniam, D. Naveh, and E. Towe, "Tunable band gaps in bilayer transition-metal dichalcogenides," *Physical Review B*, vol. 84, no. 20, p. 205325, 2011.

[69] X. Zhang, Y. Sun, W. Gao, Y. Lin, X. Zhao, Q. Wang, X. Yao, M. He, X. Ye, and Y. Liu, "Sizable bandgaps of graphene in 3d transition metal intercalated defective graphene/wse 2 heterostructures," *RSC advances*, vol. 9, no. 32, pp. 18 157–18 164, 2019.

[70] J. Gusakova, X. Wang, L. L. Shiau, A. Krivosheeva, V. Shaposhnikov, V. Borisenko, V. Gusakov, and B. K. Tay, "Electronic properties of bulk and monolayer tmds: theoretical study within dft framework (gvj-2e method)," *physica status solidi (a)*, vol. 214, no. 12, p. 1700218, 2017.

[71] L. Loh, Z. Zhang, M. Bosman, and G. Eda, "Substitutional doping in 2d transition metal dichalcogenides," *Nano Research*, vol. 14, pp. 1668–1681, 2021.

[72] M. Fang and E.-H. Yang, "Advances in two-dimensional magnetic semiconductors via substitutional doping of transition metal dichalcogenides," *Materials*, vol. 16, no. 10, p. 3701, 2023.

[73] H. Terrones, F. López-Urías, and M. Terrones, "Novel hetero-layered materials with tunable direct band gaps by sandwiching different metal disulfides and diselenides," *Scientific reports*, vol. 3, no. 1, p. 1549, 2013.

[74] J. Wang, F. Sun, S. Yang, Y. Li, C. Zhao, M. Xu, Y. Zhang, and H. Zeng, "Robust ferromagnetism in mn-doped mos2 nanostructures," *Applied Physics Letters*, vol. 109, no. 9, 2016.

[75] A. Ramasubramaniam and D. Naveh, "Mn-doped monolayer mos 2: An atomically thin dilute magnetic semiconductor," *Physical Review B*, vol. 87, no. 19, p. 195201, 2013.

[76] Z. Xiang, Z. Zhang, X. Xu, Q. Zhang, Q. Wang, and C. Yuan, "Room-temperature ferromagnetism in co doped mos 2 sheets," *Physical Chemistry Chemical Physics*, vol. 17, no. 24, pp. 15 822–15 828, 2015.

[77] Y. Cheng, Q. Zhang, and U. Schwingenschlögl, "Valley polarization in magnetically doped single-layer transition-metal dichalcogenides," *Physical Review B*, vol. 89, no. 15, p. 155429, 2014.

[78] T. Cai, S. A. Yang, X. Li, F. Zhang, J. Shi, W. Yao, and Q. Niu, "Magnetic control of the valley degree of freedom of massive dirac fermions with application to transition metal dichalcogenides," *Physical Review B*, vol. 88, no. 11, p. 115140, 2013.

[79] S. Dufferwiel, T. P. Lyons, D. D. Solnyshkov, A. A. Trichet, F. Withers, S. Schwarz, G. Malpuech, J. M. Smith, K. S. Novoselov, M. S. Skolnick *et al.*, "Valley-addressable polaritons in atomically thin semiconductors," *Nature Photonics*, vol. 11, no. 8, pp. 497–501, 2017.

[80] E. J. Sie, A. J. Frenzel, Y.-H. Lee, J. Kong, and N. Gedik, "Intervalley biexcitons and many-body effects in monolayer mos 2," *Physical Review B*, vol. 92, no. 12, p. 125417, 2015.

[81] E. J. Sie, C. H. Lui, Y.-H. Lee, J. Kong, and N. Gedik, "Observation of intervalley biexcitonic optical stark effect in monolayer ws2," *Nano letters*, vol. 16, no. 12, pp. 7421–7426, 2016.

[82] F. Zhang, B. Zheng, A. Sebastian, D. H. Olson, M. Liu, K. Fujisawa, Y. T. H. Pham, V. O. Jimenez, V. Kalappattil, L. Miao *et al.*, "Monolayer vanadium-doped tungsten disulfide: a room-temperature dilute magnetic semiconductor," *Advanced Science*, vol. 7, no. 24, p. 2001174, 2020.

[83] D. L. Duong, S. J. Yun, Y. Kim, S.-G. Kim, and Y. H. Lee, "Long-range ferromagnetic ordering in vanadium-doped wse2 semiconductor," *Applied Physics Letters*, vol. 115, no. 24, 2019.

[84] Y. Cheng, Z. Zhu, W. Mi, Z. Guo, and U. Schwingenschlögl, "Prediction of two-dimensional diluted magnetic semiconductors: Doped monolayer mos 2 systems," *Physical Review B*, vol. 87, no. 10, p. 100401, 2013.

[85] R. Mishra, W. Zhou, S. J. Pennycook, S. T. Pantelides, and J.-C. Idrobo, "Long-range ferromagnetic ordering in manganese-doped two-dimensional dichalcogenides," *Physical Review B*, vol. 88, no. 14, p. 144409, 2013.

[86] H. Ohno, n. A. Shen, a. F. Matsukura, A. Oiwa, A. Endo, S. Katsumoto, and Y. Iye, "(ga, mn) as: a new diluted magnetic semiconductor based on gaas," *Applied Physics Letters*, vol. 69, no. 3, pp. 363–365, 1996.

[87] T. Dietl, "A ten-year perspective on dilute magnetic semiconductors and oxides," *Nature materials*, vol. 9, no. 12, pp. 965–974, 2010.

[88] J. L. Lado and J. Fernández-Rossier, "On the origin of magnetic anisotropy in two dimensional cri3," *2D Materials*, vol. 4, no. 3, p. 035002, 2017.

[89] M. Habib, Z. Muhammad, R. Khan, C. Wu, Z. Ur Rehman, Y. Zhou, H. Liu, and L. Song, "Ferromagnetism in cvt grown tungsten diselenide single crystals with nickel doping," *Nanotechnology*, vol. 29, no. 11, p. 115701, 2018.

[90] L. Yang, H. Wu, W. Zhang, X. Lou, Z. Xie, X. Yu, Y. Liu, and H. Chang, "Ta doping enhanced room-temperature ferromagnetism in 2d semiconducting mote2 nanosheets," *Advanced Electronic Materials*, vol. 5, no. 10, p. 1900552, 2019.

[91] S. J. Yun, D. L. Duong, D. M. Ha, K. Singh, T. L. Phan, W. Choi, Y.-M. Kim, and Y. H. Lee, "Ferromagnetic order at room temperature in monolayer wse2 semiconductor via vanadium dopant," *Advanced Science*, vol. 7, no. 9, p. 1903076, 2020.

[92] C. J. Gil, A. Pham, A. Yu, and S. Li, "An ab initio study of transition metals doped with wse2 for long-range room temperature ferromagnetism in two-dimensional transition metal dichalcogenide," *Journal of Physics: Condensed Matter*, vol. 26, no. 30, p. 306004, 2014.

[93] Q. Xin, X. Zhao, and T. Wang, "Electronic and magnetic properties of mn-doped wse2 monolayer under strain," *Physica E: Low-dimensional Systems and Nanostructures*, vol. 88, pp. 11–17, 2017.

[94] S. Mekonnen Hailemariam, "Electronic structure and room temperature of 2d dilute magnetic semiconductors in bilayer mos2-doped mn," *Advances in Condensed Matter Physics*, vol. 2020, pp. 1–8, 2020.

[95] H. Ohno, a. D. Chiba, a. F. Matsukura, T. Omiya, E. Abe, T. Dietl, Y. Ohno, and K. Ohtani, "Electric-field control of ferromagnetism," *Nature*, vol. 408, no. 6815, pp. 944–946, 2000.

[96] H. Ohno, "Making nonmagnetic semiconductors ferromagnetic," *science*, vol. 281, no. 5379, pp. 951–956, 1998.

[97] K. Sato, L. Bergqvist, J. Kudrnovskỳ, P. H. Dederichs, O. Eriksson, I. Turek, B. Sanyal, G. Bouzerar, H. Katayama-Yoshida, V. Dinh *et al.*, "First-principles theory of dilute magnetic semiconductors," *Reviews of modern physics*, vol. 82, no. 2, p. 1633, 2010.

[98] C.-S. Park, D. Chu, Y. Shon, J. Lee, and E. K. Kim, "Room temperature ferromagnetic and ambipolar behaviors of mos2 doped by manganese oxide using an electrochemical method," *Applied Physics Letters*, vol. 110, no. 22, 2017.

[99] P. Kumar, R. Skomski, and R. Pushpa, "Magnetically ordered transition-metal-intercalated wse2," *ACS omega*, vol. 2, no. 11, pp. 7985–7990, 2017.

[100] W.-B. Zhang, Q. Qu, P. Zhu, and C.-H. Lam, "Robust intrinsic ferromagnetism and half semiconductivity in stable two-dimensional single-layer chromium trihalides," *Journal of Materials Chemistry C*, vol. 3, no. 48, pp. 12 457–12 468, 2015.

[101] W. Yu, J. Li, T. S. Herng, Z. Wang, X. Zhao, X. Chi, W. Fu, I. Abdelwahab, J. Zhou, J. Dan *et al.*, "Chemically exfoliated vse2 monolayers with room-temperature ferromagnetism," *Advanced Materials*, vol. 31, no. 40, p. 1903779, 2019.

[102] S. Tiwari, M. Van de Put, B. Sorée, C. Hinkle, and W. G. Vandenberghe, "Reduction of magnetic interaction due to clustering in doped transition-metal dichalcogenides: A case study of mn-, v-, and fe-doped wse2," *ACS Applied Materials & Interfaces*, vol. 16, no. 4, pp. 4991–4998, 2024.

[103] Z. Y. Zhu, Y. C. Cheng, and U. Schwingenschlögl, "Giant spin-orbit-induced spin splitting in two-dimensional transition-metal dichalcogenide semiconductors," *Physical Review B*, vol. 84, no. 15, p. 153402, 2011.

[104] W. S. Yun, S. Han, S. C. Hong, I. G. Kim, and J. Lee, "Thickness and strain effects on electronic structures of transition metal dichalcogenides: 2h-m x 2 semiconductors (m= mo, w; x= s, se, te)," *Physical Review B*, vol. 85, no. 3, p. 033305, 2012.

[105] W. Jin, P.-C. Yeh, N. Zaki, D. Zhang, J. T. Sadowski, A. Al-Mahboob, A. M. van Der Zande, D. A. Chenet, J. I. Dadap, I. P. Herman *et al.*, "Direct measurement of the thickness-dependent electronic band structure of mos 2 using angle-resolved photoemission spectroscopy," *Physical review letters*, vol. 111, no. 10, p. 106801, 2013.

[106] I. G. Lezama, A. Arora, A. Ubaldini, C. Barreteau, E. Giannini, M. Potemski, and A. F. Morpurgo, "Indirect-to-direct band gap crossover in few-layer mote2," *Nano letters*, vol. 15, no. 4, pp. 2336–2342, 2015.

[107] S. Roy and P. Bermel, "Electronic and optical properties of ultra-thin 2d tungsten disulfide for photovoltaic applications," *Solar Energy Materials and Solar Cells*, vol. 174, pp. 370–379, 2018.

[108] Y. Li, A. Chernikov, X. Zhang, A. Rigosi, H. M. Hill, A. M. Van Der Zande, D. A. Chenet, E.-M. Shih, J. Hone, and T. F. Heinz, "Measurement of the optical dielectric function of monolayer transition-metal dichalcogenides: Mos 2, mo s e 2, ws 2, and ws e 2," *Physical Review B*, vol. 90, no. 20, p. 205422, 2014.

[109] B. K. Moghal and M. R. Islam, "Tuning the electronic, phonon, and optical properties by strain-induced on the monolayer transition metal dichalcogenides ase2 (a= mo and w)," *Materials Today Communications*, vol. 31, p. 103240, 2022.

[110] C. Cabrera, D. Contreras-Solorio, and L. Hernández, "Joint density of states in low dimensional semiconductors," *Physica E: Low-dimensional Systems and Nanostructures*, vol. 76, pp. 103–108, 2016.

[111] C. Lui, A. Frenzel, D. Pilon, Y.-H. Lee, X. Ling, G. Akselrod, J. Kong, and N. Gedik, "Trion-induced negative photoconductivity in monolayer mos 2," *Physical review letters*, vol. 113, no. 16, p. 166801, 2014.

[112] A. Singh, G. Moody, K. Tran, M. E. Scott, V. Overbeck, G. Berghäuser, J. Schaibley, E. J. Seifert, D. Pleskot, N. M. Gabor *et al.*, "Trion formation dynamics in monolayer transition metal dichalcogenides," *Physical Review B*, vol. 93, no. 4, p. 041401, 2016.

[113] Y. You, X.-X. Zhang, T. C. Berkelbach, M. S. Hybertsen, D. R. Reichman, and T. F. Heinz, "Observation of biexcitons in monolayer wse 2," *Nature Physics*, vol. 11, no. 6, pp. 477–481, 2015.

[114] J. S. Ross, P. Klement, A. M. Jones, N. J. Ghimire, J. Yan, D. Mandrus, T. Taniguchi, K. Watanabe, K. Kitamura, W. Yao *et al.*, "Electrically tunable excitonic light-emitting diodes based on monolayer wse2 p–n junctions," *Nature nanotechnology*, vol. 9, no. 4, pp. 268–272, 2014.

[115] S. P. Rodrigues and W. Cai, "Tuning harmonics with excitons," *Nature Nanotechnology*, vol. 10, no. 5, pp. 387–388, 2015.

[116] K. L. Seyler, J. R. Schaibley, P. Gong, P. Rivera, A. M. Jones, S. Wu, J. Yan, D. G. Mandrus, W. Yao, and X. Xu, "Electrical control of second-harmonic generation in a wse2 monolayer transistor," *Nature nanotechnology*, vol. 10, no. 5, pp. 407–411, 2015.

[117] L.-Y. Xie and J.-M. Zhang, "The structure, electronic, magnetic and optical properties of the mn doped and mn-x (x= f, cl, br, i and at) co-doped monolayer ws2: a first-principles study," *Journal of Alloys and Compounds*, vol. 702, pp. 138–145, 2017.

[118] G. Froehlicher, "Optical spectroscopy of two-dimensional materials: graphene, transition metal dichalcogenides and van der waals heterostructures," Ph.D. dissertation, Université de Strasbourg, 2016.

[119] Y. Sun, S. Gao, F. Lei, and Y. Xie, "Atomically-thin two-dimensional sheets for understanding active sites in catalysis," *Chemical Society Reviews*, vol. 44, no. 3, pp. 623–636, 2015.

[120] J. Kang, W. Cao, X. Xie, D. Sarkar, W. Liu, and K. Banerjee, "Graphene and beyond-graphene 2d crystals for next-generation green electronics," in *Micro-and Nanotechnology Sensors, Systems, and Applications VI*, vol. 9083. SPIE, 2014, pp. 20–26.

[121] F. Bonaccorso, L. Colombo, G. Yu, M. Stoller, V. Tozzini, A. C. Ferrari, R. S. Ruoff, and V. Pellegrini, "Graphene, related two-dimensional crystals, and hybrid systems for energy conversion and storage," *Science*, vol. 347, no. 6217, p. 1246501, 2015.

[122] P. Hohenberg and W. Kohn, "Inhomogeneous electron gas," *Physical review*, vol. 136, no. 3B, p. B864, 1964.

[123] G. Kresse and J. Furthmüller, "Efficient iterative schemes for ab initio total-energy calculations using a plane-wave basis set," *Physical review B*, vol. 54, no. 16, p. 11169, 1996.

[124] N. A. Hill, "Density functional studies of multiferroic magnetoelectrics," *Annual Review of Materials Research*, vol. 32, no. 1, pp. 1–37, 2002.

[125] R. M. Martin, *Electronic structure: basic theory and practical methods*. Cambridge university press, 2020.

[126] W. Kohn and L. J. Sham, "Self-consistent equations including exchange and correlation effects," *Physical review*, vol. 140, no. 4A, p. A1133, 1965.

[127] M. El-Batanouny, *Advanced quantum condensed matter physics: one-body, many-body, and topological perspectives*. Cambridge University Press, 2020.

[128] E. Engel, *Density functional theory*. Springer, 2011.

[129] W. Koch and M. C. Holthausen, *A chemist's guide to density functional theory*. John Wiley & Sons, 2015.

[130] J. P. Perdew, K. Burke, and M. Ernzerhof, "Generalized gradient approximation made simple," *Physical review letters*, vol. 77, no. 18, p. 3865, 1996.

[131] J. P. Perdew and Y. Wang, "Accurate and simple analytic representation of the electron-gas correlation energy," *Physical review B*, vol. 45, no. 23, p. 13244, 1992.

[132] V. I. Anisimov, J. Zaanen, and O. K. Andersen, "Band theory and mott insulators: Hubbard u instead of stoner i," *Physical Review B*, vol. 44, no. 3, p. 943, 1991.

[133] I. Solovyev, P. Dederichs, and V. Anisimov, "Corrected atomic limit in the local-density approximation and the electronic structure of d impurities in rb," *Physical Review B*, vol. 50, no. 23, p. 16861, 1994.

[134] I. Timrov, N. Marzari, and M. Cococcioni, "Hubbard parameters from density-functional perturbation theory," *Physical Review B*, vol. 98, no. 8, p. 085127, 2018.

[135] M. Cococcioni, "The lda+ u approach: a simple hubbard correction for correlated ground states," *Correlated Electrons: From Models to Materials Modeling and Simulation*, vol. 2, 2012.

[136] B. Himmetoglu, A. Floris, S. De Gironcoli, and M. Cococcioni, "Hubbard-corrected dft energy functionals: The lda+ u description of correlated systems," *International Journal of Quantum Chemistry*, vol. 114, no. 1, pp. 14–49, 2014.

[137] V. I. Anisimov, I. Solovyev, M. Korotin, M. Czyżyk, and G. Sawatzky, "Density-functional theory and nio photoemission spectra," *Physical Review B*, vol. 48, no. 23, p. 16929, 1993.

[138] M. Cococcioni and S. De Gironcoli, "Linear response approach to the calculation of the effective interaction parameters in the lda+ u method," *Physical Review B*, vol. 71, no. 3, p. 035105, 2005.

[139] I. Timrov, N. Marzari, and M. Cococcioni, "Self-consistent hubbard parameters from density-functional perturbation theory in the ultrasoft and projector-augmented wave formulations," *Physical Review B*, vol. 103, no. 4, p. 045141, 2021.

[140] S. Baroni, S. De Gironcoli, A. Dal Corso, and P. Giannozzi, "Phonons and related crystal properties from density-functional perturbation theory," *Reviews of modern Physics*, vol. 73, no. 2, p. 515, 2001.

[141] X. Gonze and J.-P. Vigneron, "Density-functional approach to nonlinear-response coefficients of solids," *Physical Review B*, vol. 39, no. 18, p. 13120, 1989.

[142] X. Gonze, "Perturbation expansion of variational principles at arbitrary order," *Physical Review A*, vol. 52, no. 2, p. 1086, 1995.

[143] A. E. Mattsson and W. Kohn, "An energy functional for surfaces," *The Journal of Chemical Physics*, vol. 115, no. 8, pp. 3441–3443, 2001.

[144] H. J. Monkhorst and J. D. Pack, "Special points for brillouin-zone integrations," *Physical review B*, vol. 13, no. 12, p. 5188, 1976.

[145] D. Vanderbilt, "Soft self-consistent pseudopotentials in a generalized eigenvalue formalism," *Physical review B*, vol. 41, no. 11, p. 7892, 1990.

[146] P. E. Blöchl, "Projector augmented-wave method," *Physical review B*, vol. 50, no. 24, p. 17953, 1994.

[147] D. Hamann, M. Schlüter, and C. Chiang, "Norm-conserving pseudopotentials," *Physical Review Letters*, vol. 43, no. 20, p. 1494, 1979.

[148] G. Kresse and D. Joubert, "From ultrasoft pseudopotentials to the projector augmented-wave method," *Physical review b*, vol. 59, no. 3, p. 1758, 1999.

[149] G. Prandini, A. Marrazzo, I. E. Castelli, N. Mounet, and N. Marzari, "Precision and efficiency in solid-state pseudopotential calculations," *npj Computational Materials*, vol. 4, no. 1, p. 72, 2018.

[150] P. Giannozzi, S. Baroni, N. Bonini, M. Calandra, R. Car, C. Cavazzoni, D. Ceresoli, G. L. Chiarotti, M. Cococcioni, I. Dabo *et al.*, "Quantum espresso: a modular and open-source software project for quantum simulations of materials," *Journal of physics: Condensed matter*, vol. 21, no. 39, p. 395502, 2009.

[151] A. Floris, I. Timrov, B. Himmetoglu, N. Marzari, S. de Gironcoli, and M. Cococcioni, "Hubbard-corrected density functional perturbation theory with ultrasoft pseudopotentials," *Physical Review B*, vol. 101, no. 6, p. 064305, 2020.

[152] F. Birch, "Finite elastic strain of cubic crystals," *Physical review*, vol. 71, no. 11, p. 809, 1947.

[153] J. Sipe and E. Ghahramani, "Nonlinear optical response of semiconductors in the independent-particle approximation," *Physical Review B*, vol. 48, no. 16, p. 11705, 1993.

[154] P. Ondračka, D. Holec, and L. Zajíčková, "Predicting optical properties from ab initio calculations," *Optical Characterization of Thin Solid Films*, pp. 83–104, 2018.

[155] V. B. Bobrov, S. Trigger, G. Van Heijst, and P. Schram, "Kramers-kronig relations for the dielectric function and the static conductivity of coulomb systems," *Europhysics Letters*, vol. 90, no. 1, p. 10003, 2010.

[156] D. Thapa, *Tunable Electronic and Magnetic Properties in 2d-WSe 2 Monolayer via Vanadium (V) Doping and Chalcogenide (Se) Vacancies: A First-Principle Investigations*. Mississippi State University, 2021.

[157] T. N. Tran, M. T. Dang, Q. H. Tran, T. T. Luong, and V. A. Dinh, "Band valley modification under strain in monolayer wse2," *AIP Advances*, vol. 12, no. 11, 2022.

[158] D. Abdullah and D. C. Gupta, "Exploring the half-metallic ferromagnetism, dynamical and mechanical stability, optoelectronic and thermoelectric properties of k2nami6 (m= mn, co, ni) for spintronic applications," *Scientific Reports*, vol. 13, no. 1, p. 12795, 2023.

[159] Y. Wang, S. Li, and J. Yi, "Electronic and magnetic properties of co doped mos2 monolayer," *Scientific reports*, vol. 6, no. 1, p. 24153, 2016.

# List of Publications and Presentations

## Published and under preparation works

1. Mulugeta Woldesenbet, Nebiyu Debelo, and Menberu Woldemariam. "Structural, Electronic, Dynamic, and Optical Properties of 2D Monolayer Tungsten Telluride ($2H - WTe_2$) under Small Biaxial Strain Using Density Functional Theory (DFT and DFT+U)." Advances in Condensed Matter Physics 2023 (2023) published.

2. M. S. Woldesenbet, N.G. Debelo and M. M. Woldemariam "The effect of Mn-doping on structural, electronic, ferromagnetic, and optical properties of monolayer-$WSe_2$ using first-principles calculation. " 2024 The European Physical Journal B accepted.

3. M. S. Woldesenbet, N.G. Debelo and M. M. Woldemariam "Tuning the electronic and optical properties of 2D $WS_2/WSe_2$ heterobilayer under biaxial strain: A first principles study." Open Physics Journal, under review.

# Conference Participation and Presentations

1. Electronic Structure Methods and Application for Emerging Energy Technologies Organized by Computational Sciences and Engineering Society of Ethiopia and International center for Theoretical Physics (ICTP) November 24-December 2, 2021, participant.

2. $4^{th}$ National Research Conference at Bonga University, as May 10-11, 2024 participant and presenter.

3. Scientific Writing and Publication Ethics organized by Jimma University in collaboration with TDR/WHO/CRDF 30-31 March, 2022, as participant

4. $10^{th}$ National research conference and presentation at Wachemo University, May 30-31, 2024, as participant and presenter.